



# **Fluid Mixing and Solute Transport in Transient Subsurface Flow**

A thesis submitted in fulfilment of the requirements for the degree of Master of Engineering

Junhong Wu

Bachelor of Engineering, Xi'an Shiyou University, China

School of Engineering

College of Science, Engineering and Health

RMIT University

October 2019

## **Declaration**

I certify that except where due acknowledgement has been made, the work is that of the author alone; the work has not been submitted previously, in whole or in part, to qualify for any other academic award; the content of the thesis is the result of work which has been carried out since the official commencement date of the approved research program; any editorial work, paid or unpaid, carried out by a third party is acknowledged; and, ethics procedures and guidelines have been followed.

Junhong Wu

30 October 2019

## **Abstract**

The transport of solutes in groundwater systems is central to a wide array of physical, chemical, geological and biological processes that impact the quality of this critical water resource. Whilst research efforts over the past century have focused on understanding and quantifying solute transport in steady groundwater flows, transport in transiently forced systems has received significantly less attention. The additional degree of freedom associated with these transient flows admits a much richer set of possible transport dynamics, with significant implications for the above fluid-borne processes. This thesis aims to uncover the complex transport dynamics that arise in transiently forced aquifer systems, the mechanisms that govern these dynamics, and the relationships between the aquifer transport structure, forcing parameters and physical properties of the porous medium.

A combination of numerical modelling and dynamical systems theory was used to investigate this phenomenon, where a conventional linear groundwater flow model subject to tidal forcing was developed, and a group of governing dimensionless parameters were identified to quantify transport dynamics. Simulations were performed over the dimensionless parameter space, and specialized mathematical techniques were used to visualize and classify the Lagrangian transport structure of the flow and elucidate the impacts on solute transport.

It was found that under certain conditions, steady Darcy flows generate complex transport and mixing phenomena near the tidal boundary. Aquifer heterogeneity, storativity, and forcing magnitude cause flow reversals which generate closed flow regions and chaotic mixing. These features significantly augment fluid mixing and transport, leading to anomalous residence time distributions, flow segregation, accelerated mixing and the potential for profoundly altered reaction kinetics. It also found that governing parameters

control the complex transport dynamics and the bifurcations between transport structures topologies (i.e. open, closed or chaotic).

This study uncovers a wide range of complex transport dynamics in transiently forced aquifers that has profound implications for the understanding and quantification of solute transport in these important groundwater systems. And the results in this thesis predict that complex transport structures and dynamics arise in natural transiently forced aquifers around the world. When such dynamics do arise, it will lead to mixing and reactive transport patterns that are very different from those predicted by conventional Darcy flow models.

## **Acknowledgements**

I want to say thank you for so many people because I cannot complete my research project and thesis without their kind support and guidance.

I definitely need to start with my senior supervisor; Dr Daniel Lester. It is obvious that I could never have got as far as I did without his willingness to become my supervisor and keep pushing me to strengthen my research skills. I still remember, in the beginning, he asked me whether I was prepared to work hard and improved myself to achieve research excellence. Now I have to admit I might be the worst student he ever had, but if I have chance to do a PhD program, his suggestions and guidance would be the most precious research treasure for me. Thank you so much Daniel, thanks for helping me to open the research gate!

I would also like to mention Michael Trefry, Guy Metcalfe and my associate supervisor Bruce Hobbs. I am impressed and encouraged by their endless passion for the research field. And their many sincerely advice, such as “Do the best you can at every step. Don't put in half-ready cases if you can avoid it” and “One more little push to change the world for the better”. They act as several beacons to guide and remind me to keep proving yourself constantly.

Last but not least, many thanks to my parents, a sweet and warm family when I live in Melbourne, Patricia Coffee Brewers, and all of my friends. I never feel alone and still can sense their most reliable support when I explore the vast research universe.

# Table of Contents

<b>Declaration.....</b>	<b>i</b>
<b>Abstract.....</b>	<b>ii</b>
<b>Acknowledgements.....</b>	<b>iv</b>
<b>List of Figures.....</b>	<b>ix</b>
<b>List of Tables .....</b>	<b>xv</b>
<b>List of Acronyms and Abbreviations .....</b>	<b>xvi</b>
<b>List of Symbols .....</b>	<b>xvii</b>
<b>1. Introduction.....</b>	<b>1</b>
1.1. Background Information .....	1
1.2. Problem Statement .....	4
1.3. Rationale.....	7
1.4. Objectives of the Research .....	7
1.5. Research Questions .....	9
1.6. Structure of the Thesis.....	12
<b>2. Literature Review .....</b>	<b>14</b>
2.1. Development of Groundwater Hydrology.....	15
2.1.1. Classical Groundwater Hydrology.....	15
2.1.2. Solute Transport in Steady Darcy Flow .....	17
2.1.3. Transport and Mixing in Coastal Aquifers .....	18
2.2. The Lagrangian Kinematics of Groundwater Flows .....	20
2.2.1. The Concept of Chaotic Advection.....	21
2.2.2. Chaotic Advection in Open Flows .....	25
2.3. Research Gaps .....	28
<b>3. Research Methodology .....</b>	<b>30</b>

3.1.	2D Aquifer Model .....	31
3.1.1.	Governing Equations .....	31
3.1.2.	Steady and Periodic Solutions .....	33
3.2.	Dimensionless Parameters.....	34
3.2.1.	Heterogeneity Model .....	34
3.2.2.	Townley Number $\mathcal{T}$ .....	35
3.2.3.	Tidal Strength $\mathcal{G}$ .....	35
3.2.4.	Tidal Compression Ratio $\mathcal{C}$ .....	36
3.2.5.	Heterogeneity Characters $\mathcal{H}_t$ and $\mathcal{H}_x$ .....	37
3.3.	Nondimensional Governing Equations .....	38
3.3.1.	Dimensionless Model.....	38
3.3.2.	Fluid Velocity .....	39
3.3.3.	Numerical Method for Fluid Velocity Field .....	39
3.4.	Particle Tracking Methods and Kinematics .....	48
3.4.1.	Lagrangian Kinematics .....	48
3.4.2.	Lagrangian Particle Tracking.....	49
3.4.3.	Mapping Method.....	49
3.5.	Visualization and Analysis of Transport Structures.....	50
3.5.1.	Poincaré Sections .....	51
3.5.2.	Characteristic Transport Structures in Periodically Forced Aquifers .....	52
3.5.3.	Residence Time Distributions (RTDs).....	55
3.5.4.	Finite-Time Lyapunov Exponents (FTLEs).....	55
3.6.	Chapter Summary.....	59
<b>4.</b>	<b>Complex Transport in Transiently Forced Aquifers .....</b>	<b>60</b>
4.1.	Basic Hydraulic Characteristics .....	60
4.2.	Flux Ellipses and Flow Reversal .....	61
4.3.	Connection of Flow Reversal to Matrix Conductivity and Poroelasticity .....	63

4.4.	Integrability of Particle Trajectories for Incompressible Media .....	64
4.5.	Tidal Flow in Heterogeneous Domains.....	65
4.6.	Mechanisms and Measures of Transport Complexity .....	69
4.6.1.	Flow Reversal Ellipses.....	69
4.6.2.	Residence Time Distributions (RTDs).....	70
4.6.3.	Poincaré Sections .....	73
4.6.4.	Elucidation of Lagrangian Kinematics and Lagrangian Topology.....	75
4.6.5.	Finite-Time Lyapunov Exponents (FTLEs).....	81
4.7.	Chapter Summary.....	82
<b>5.</b>	<b>Parametric Variability of Complex Transport .....</b>	<b>84</b>
5.1.	Key Dimensionless Parameters .....	84
5.2.	Impact of Tidal Strength and Attenuation on Aquifer Transport.....	86
5.3.	Impact of Aquifer Compressibility on Transport .....	90
5.4.	Sensitivity to Hydraulic Conductivity Field.....	91
5.4.1.	Statistical Invariance of Model Predictions .....	92
5.4.2.	Impact of Correlation Length.....	93
5.4.3.	Impact of Conductivity Variance .....	96
5.5.	Chapter Summary.....	96
<b>6.</b>	<b>Discussion and Physical Relevance for Natural Coastal Aquifers.....</b>	<b>98</b>
6.1.	Implications for Transport and Reaction.....	98
6.1.1.	Residence Time Distributions - Segregation and Singularity.....	98
6.1.2.	Flow Reversal, Traceability and Reaction .....	99
6.2.	Potential for Chaos in Field Settings.....	100
6.3.	Solute Trapping and Transport.....	103
6.3.1.	Size Distribution of Closed Regions.....	103
6.3.2.	Solute Transport across Trapped Regions .....	105
6.4.	Tidal Transition Diagram .....	107

6.5. Chapter Summary .....	111
<b>7. Conclusions .....</b>	<b>113</b>
7.1. Conclusions .....	113
7.2. Recommendations of Further Research .....	117
<b>References .....</b>	<b>121</b>
<b>Appendices .....</b>	<b>132</b>
Appendix A: Relative penetration distance of saline wedges.....	132

## List of Figures

<b>Figure 1.</b> The evolutions of the dye trace during several activation times in RPM flow via reorientation of the injection (red) and extraction (blue) wells. Adapted from Trefry et al. (2012).....	24
<b>Figure 2.</b> Enhanced mixing zones and kinematic boundaries in RPM flow. Adapted from Trefry et al. (2012).....	24
<b>Figure 3.</b> (a) (top) Numerical simulations of particle trajectories within a von Kármán vortex street emanating from Guadalupe Island. Flow reversal due to vortices corresponds to regions indicated by A, B, C, D. (bottom) Some particles orbits have long residence times due to flow reversal (adapted from Arístegui et al. (1997)). (b) Schematic depicting trapping of some fluid tracer particles within a mixing region (represented by the dotted line) in an open flow with the increasing number of flow periods $T$ (adapted from Tél et al. (2005)). (c) Schematic of the evolution of a blob (green) of tracer particles with the number of flow periods and the associated stable (red) and unstable (blue) manifolds in the vortex-shedding wake of a cylinder. Particles at the periodic point $\mathbf{P}$ remain trapped there indefinitely (adapted from Károlyi et al. (2002)).....	27
<b>Figure 4.</b> Schematic of the square aquifer domain $\mathcal{D}$ and boundaries, showing the mean regional flow gradient $J$ and spatial heterogeneity of $K$ . .....	32
<b>Figure 5.</b> Comparison of flow paths integrated forward in time using simple interpolation of finite difference solutions (red) and full CE-corrected solutions (blue) superimposed on the associated $\kappa$ field (shaded). Numbering refers to the number of elapsed periods $P$ ( $\times 100$ ) along each path, starting at $t = 0$ at the points to the right. ....	44
<b>Figure 6.</b> Self-consistency checks of azimuths from steady fluxes and head gradients for the finite difference solution (left column), interpolated solution (centre column) and the updated	

flux (right column) evaluated for two different correlation lengths (upper and lower rows).

The numerical scheme gives better results at larger correlation lengths. ....46

**Figure 7.** Dependence of mean azimuthal difference  $\Delta\theta$  for the updated fluxes on the correlation length  $\lambda/\Delta$  of a set of realizations of the input conductivity field with variances  $\sigma \log \kappa^2 = 1/2$  (squares), 1 (dots), 2 (triangles) and 4 (circles). Curves are fitted to each set of points to aid the eye, and the acceptability cutoff is set at  $1^\circ$  (dashed line). ....47

**Figure 8.** Bifurcation of transport structure types with increasing aquifer compressibility  $\mathcal{C}$  with  $\mathcal{T} = 10$ ,  $\mathcal{G} = 100$  in the region  $(x, y) = (0.3, 0.5) \times (0.75, 0.95)$  of the aquifer domain. Examples of (a) open ( $\mathcal{C} = 0.002 < \mathcal{C}_1$ ), (b) closed ( $\mathcal{C}_1 < \mathcal{C} = 0.005 < \mathcal{C}_2$ ), (c) closed ( $\mathcal{C}_1 < \mathcal{C} = 0.1 < \mathcal{C}_2$ ) and (d) chaotic ( $\mathcal{C}_2 < \mathcal{C} = 0.2$ ) transport structures in periodically forced aquifers. Arrows denote propagation of tracer particles along 1D trajectories, scattered points denote incoherent, chaotic motion of tracer particles. Dots denote elliptic (E) or hyperbolic (H) points, blue and red arrows denote unstable and stable manifolds. See text for more details. 53

**Figure 9.** Schematic of flux ellipses drawn in blue - (a) regular (excluding the origin), and (b) canonical (containing the origin). Arrows on the ellipses indicate the direction of increasing time  $t$ . Both flux components of the canonical ellipse change sign at times during the oscillation period.....62

**Figure 10.** (a) Density map of log hydraulic conductivity  $\kappa$  where lower (higher) values are darker (lighter). (b) Profile of the steady head  $h_s$  for the heterogeneous simulation (squares) and reference homogeneous solution (line) along the green line  $y = 0.5$  shown in (a). (c) Variation of the normalized total porosity  $\phi/\phi_{\text{ref}}$  along  $y = 0.5$  over the tidal cycle. (d) Same as for (b) but showing the periodic head solution  $h_p$  (square) and phase lag  $\arg h_p$  (circles) for the heterogeneous simulation with the reference homogeneous solutions shown as curves. ....66

**Figure 11.** (top) Flow paths, with the number of flow periods shown along each trajectory. (middle left) Detail of the red box with flow paths coloured and dotted every period. Note the change in vertical order of the flow paths from entry to exit (braiding). (middle right) Schematic of generic braiding of fluid trajectories with time  $t$  (adapted from Finn and Thiffeault (2011)). (bottom) Corresponding flow paths for the zero-compression case – no braiding is possible (see Section 4.4).....68

**Figure 12.** Location of clockwise (black) and anticlockwise (red) canonical flux ellipses (red/black points) evaluated over the aquifer domain. The edge of the canonical flux ellipse distribution approximates the extent of the tidally active zone shown by the green line drawn at  $x = x_{taz}$ . ....70

**Figure 13.** (a) The blue curve shows the RTD for the steady regional discharge flow, and the black dots indicate residence times for the tidally forced flow. Blue bars indicate zones excluded to regional discharge. Several zones of braided tidal discharge are noted. (b) Maps of RTD for the transient tidal flow plotted in terms of initial position for a  $1000 \times 1000$  grid of particles seeded over (left) the entire tidal domain and (right) a square region covering the structure centred at  $(x, y) \approx (0.35, 0.51)$ . Particle tracking is performed up to  $t/P = 103$ , hence red points have residence time  $\tau > 103P$ . ....71

**Figure 14.** Poincaré sections formed from locations of points (black) advecting through the flow fields. Sections are assembled with time intervals  $\mathcal{P} = P$  for both steady (a) and tidal flow (b) cases. The tidal section also shows discharging points in green (near the left boundary), calculated with  $\mathcal{P} = P/10$  from the particle locations at the last completed tidal period before discharge. ....74

**Figure 15.** Annotated Poincaré section of the tidally forced aquifer showing hyperbolic (H) and elliptic (E) points, stochastic layers (S), stable (red lines) and unstable (blue lines)

manifolds, KAM islands (magenta orbits), discharge points (green points) and exclusion zones (blue bars). .....76

**Figure 16.** (a) Zoomed view of Poincaré section shown in Figure 15, illustrating the stochastic layers (pink dots) and elliptic orbits (red dots) in the mixing regions and regular orbits (blue dots) in the regular regions of the tidal domain. Points are coloured according to residence time, from the least (cyan) to the greatest (red). Roman letters, black and green dots indicate initial positions for FTLE calculations discussed in Subsection 4.6.5. (b) Detail of Poincaré sections for the mixing regions and surrounding non-chaotic structures in (a) as (black dots), showing points associated with stable (red) and unstable (blue) manifolds, respectively, entering and leaving the aquifer domain via the tidal boundary (green line). The chaotic saddle is the intersection of these manifolds, which surround the elliptic orbits (KAM islands), cantori and stochastic layers. ....79

**Figure 17.** Finite-time Lyapunov exponents calculated from five arbitrarily chosen starting locations in the stochastic layer (see Figure 16). All traces eventually exit at the tidal boundary, except trace F (KAM orbit) which does not terminate and was truncated for display. The ensemble mean and standard error bounds are indicated. ....82

**Figure 18.** Summary of Poincaré sections for  $\mathcal{C} = 0.1$  calculated via the distributed injection of particles. Particle trajectories are coloured according to residence time, from shortest (blue) to longest (red), and the colour scales change with  $\mathcal{G}$ . Green lines indicate Poincaré sections that possess trapped orbits. Purple and brown curves are the tidal emptying and inland boundaries respectively. ....87

**Figure 19.** Summary of transport simulations that exhibit closed transport structures (as indicated by crosses) for compressibility ratio (a)  $\mathcal{C} = 0.01$  and (b)  $\mathcal{C} = 0.1$ . ....89

<b>Figure 20.</b> Poincaré sections in the periodically forced aquifer under the distributed injection protocol for different values of $\mathcal{C}$ over the range $\mathcal{C} = 0 - 0.5$ for $\mathcal{T} = 10$ and $\mathcal{G} = 100$ . Green rectangles identify chaotic transport structures.....	91
<b>Figure 21.</b> Density map of log hydraulic conductivity for three different realizations of the log-Gaussian hydraulic conductivity field and associated Poincaré sections (distributed injection) for two cases, row a: $\mathcal{T} = 20$ , $\mathcal{G} = 10$ , $\mathcal{C} = 0.2$ , row b: $\mathcal{T} = 5$ , $\mathcal{G} = 50$ , $\mathcal{C} = 0.1$ . .....	93
<b>Figure 22.</b> Poincaré sections (distributed injection) for $\mathcal{G} = 100$ and $\mathcal{C} = 0.1$ with varying $\mathcal{T}$ and $\lambda$ .....	94
<b>Figure 23.</b> Average radius of trapped regions in the aquifer for different values of the correlation length $\lambda$ for two cases ( $\mathcal{T} = 10$ and $100$ ) with fixed tidal strength and compressibility ( $\mathcal{G} = 100$ , $\mathcal{C} = 0.1$ ). .....	95
<b>Figure 24.</b> Poincaré sections (distributed injection) of flow in a single log- $K$ realization for $\mathcal{T} = 10$ and $\mathcal{C} = 0.1$ with varying $\mathcal{G}$ and $\sigma \log K^2$ . .....	96
<b>Figure 25.</b> Location of the present example system (star) in $\mathcal{T} - \mathcal{G} \sigma \log K^2$ parameter space. Locations of some field studies (letters on error bars) reported in the literature are provided for reference. ....	101
<b>Figure 26.</b> (a) Residence time distribution of fluid particles for the distributed injection protocol for $\mathcal{T} = 100$ , $\mathcal{G} = 100$ at $\mathcal{C} = 0.1$ . Inset: total of the area (a) of trapped regions (closed orbits) as a proportion of aquifer area for various values of $\mathcal{T}$ and $\mathcal{G}$ at $\mathcal{C} = 0.1$ . (b) Histograms (probability density function) of the relative area (a) of individual trapped regions in the aquifer for various values of $\mathcal{T}$ and $\mathcal{G}$ at $\mathcal{C} = 0.1$ . ....	104
<b>Figure 27.</b> Tidal transition diagram showing (a) bifurcation and chaotic zones, and (b) tidal amplitude ( $gp$ ) trajectories marked each metre up to a maximum of 8 m. Ellipsoids refer to the GI (blue, limestone and sand), LN (orange, sand and clay), J (purple, limestone and sand), D (brown, limestone and sand), SR (yellow, sand and clay) and P (green, basalts) case studies	

of Section 6.2 and the small black ellipse marks the example problem  $(\mathcal{T}, \sigma_2 \mathcal{G}, \mathcal{C}) = (10^\circ, 20, 0.5)$ . Trajectories reach the elliptic zone (pink) at values  $gp = 3$  m (GI), 1.5 m (LN), 0.5 m (J), 3.5 m (D), 0.5 m (SR), 2 m (P). .....110

**Figure 28.** Global variation of the amplitudes (in metres) of the K1 (diurnal, top) and M2 (semi-diurnal, bottom) tidal modes (FES2004 data supplied by LEGOS, see Lyard et al. (2006)). Site locations used in Figure 27 are indicated by pink lettering. Zones of high amplitude indicate increased potential for Lagrangian complexity in coastal groundwater flows.....111

## List of Tables

<b>Table 1.</b> Dimensionless parameters for the tidal forcing problem. ....	85
------------------------------------------------------------------------------	----

## **List of Acronyms and Abbreviations**

ADE	Advection-Dispersion Equation
CTRW	Continuous Time Random Walk
FD method	Finite-Difference method
FTLEs	Finite-Time Lyapunov Exponents
KAM islands	Kolmogorov-Arnol'd-Moser islands
RPM flow	Programmed Rotated Potential Mixing flow
RTDs	Residence Time Distributions
SGD	Submarine Groundwater Discharge

## List of Symbols

$B$	Unit thickness
$\varphi$	Matrix porosity
$\mathbf{q}$	Darcy flux
$K$	Isotropic saturated hydraulic conductivity
$h$	Pressure head
$J$	Regional flow gradient
$T$	Transmissivity
$h_{\text{ref}}$	Reference head
$\varphi_{\text{ref}}$	Reference porosity
$S_s$	Specific storage
$S$	Storativity
$P$	Forcing period
$\omega$	Forcing frequency
$h_s$	Steady head
$h_p$	Periodic head
$\varphi_s$	Steady porosity
$\varphi_p$	Periodic porosity
$g_p$	Tidal amplitude
$K_{\text{eff}}$	Mean conductivity
$\sigma_{\log K}^2$	Log-variance of $K$
$\lambda$	Correlation length
$\mathcal{T}$	Townley number

$D_{\text{eff}}$	Effective aquifer diffusivity
$\mathcal{G}$	Tidal strength
$\mathcal{C}$	Tidal compression ratio
$\mathcal{Q}$	Dynamical parameters set
$\chi$	Statistical parameters set
$v_{\text{drift}}$	Mean drift velocity
$\mathcal{H}_t$	Temporal character
$\mathcal{H}_x$	Spatial character
$x_{\text{taz}}$	Tidally affected zone
$\Delta$	Spatial resolution of the finite difference grid
$E$	Elliptic point
$H$	Hyperbolic point
$W_{1D}^U$	Unstable manifolds
$W_{1D}^S$	Stable manifolds
$S$	Stochastic Layers
$\mathbf{F}$	Fluid deformation gradient tensor
$\mathbf{C}$	Right Cauchy-Green deformation tensor
$\Delta\tau$	Phase lag
$\alpha$	Attenuation
$\omega$	Vorticity
$\tau$	Residence time
$\mathbf{D}_H$	Hydrodynamic dispersion tensor
$D_m$	Molecular diffusivity

$R_0$	Relative radius of trapped regions
$\alpha_L$	Longitudinal dispersivity
$\bar{v}_r$	Mean regional groundwater velocity
$\tilde{v}_{max}$	Maximum tidal groundwater velocity
Pe	Péclet number

# Chapter One

## 1. Introduction

### 1.1. Background Information

It is difficult to overstate the importance of groundwater (water stored in natural underground aquifers) to society and the environment. Globally, groundwater represents 98% of the world's freshwater (Eakins & Sharman, 2010), and natural underground aquifers provide around 35% of the water used by humans (Richey et al., 2015). Over 20% of the world's population rely on crops which are irrigated by groundwater (Wada et al., 2012). At a national level, groundwater makes up around 17% of accessible water resources and over 30% of total water consumption in Australia (Sundaram et al., 2009). In arid and semi-arid areas, groundwater may be the only reliable water resource. For example, over 90% of the freshwater in the Northern Territory is sourced from aquifers (Harrington & Cook, 2014). Unlike surface water, which can easily be influenced by many external factors, groundwater in aquifers is less vulnerable to contamination. Despite this robustness, the quality of groundwater and aquifer systems are still highly sensitive to anthropogenic actions and climate changes (Ferguson & Gleeson, 2012; Hallegatte et al., 2011; Neumann et al., 2015; Robinson et al., 2018). Thus, the transport, dispersion and mixing of biological organisms and chemical species (such as pollutants and pathogens) in underground aquifers are relevant to a wide range of natural and human-made processes, from seawater intrusion in tidal aquifers to pollutant remediation and CO<sub>2</sub> sequestration. Understanding the transport of solutes and colloids in groundwater is essential for effective management of these groundwater systems.

Whilst the transport, mixing of dispersion of solutes in steady aquifer flows have been the subject of intense research over the past century, significantly less attention has been paid

to transient aquifer flows. Hence very little is presently known regarding the nature of these transient flows or the impacts upon solute transport, dispersion and mixing. Transient flows are important as many groundwater systems also involve discharge boundaries that are driven by time-varying conditions, leading to transient flows within the aquifer. For example, coastal aquifers are affected by tidal action at their discharge boundary, internal flows that are driven by tidal forcing, and also leading to complex spatiotemporal distributions on biogeochemical activities. Many studies (Geng & Boufadel, 2015; Heiss et al., 2017; Liu et al., 2018) have found that tidal fluctuations can strongly influence physicochemical gradients (e.g. salinity, pH, redox potential) in groundwater systems. Tide-induced water exchange and groundwater flow have also been shown to have a significant impact on the fate of contaminants, nutrients migration and biodegradation (Geng et al., 2017; Malott et al., 2017; Robinson et al., 2009). Similarly, seasonal variations, barometric effects and climate change can also influence riverine and lacustrine discharges, which in turn generate time-dependent internal flows and associated solute transport (Cuthbert et al., 2016; De Schepper et al., 2017; Goderniaux et al., 2011; Huang et al., 2018).

Groundwater flow in aquifer systems is typically modelled via the Darcy flow equation, which states that the flux of fluid at any point is equal to the product of the pressure gradient and hydraulic conductivity, the latter of which may be a strongly heterogeneous function in space. Under steady flow conditions, these strong conductivity fluctuations can lead to observations of “anomalous” non-Fickian transport and highly convoluted streamlines. Whilst transport in these steady flows may be considered to be “complex” in that the conductivity heterogeneities can impart non-trivial transport behaviour such as wide distributions of breakthrough times, from another perspective transport in these flows is “simple” in that steady Darcy flow admits open, regular and smooth flow streamlines (in both 2D and 3D) that organize the distribution of dispersive solutes. The presence of such open,

fixed streamlines also means that steady Darcy flows are poor mixing flows in that fluid line elements (and hence concentration gradients) can only increase algebraically with time (as opposed to exponential growth for strong mixing flows). In this sense, transport in steady Darcy flows can be considered simple, even if the associated conductivity field is highly heterogeneous.

In contrast, transient Darcy flows can admit a much more complex transport dynamics due to the additional degree of freedom imparted by the time coordinate. Specifically, such flows can admit crossing of streamlines (when viewed at different times) (Aref, 1984; Ottino, 1989), with profound impacts upon solute transport and biogeochemical activities, and can lead to rapid and complex mixing behaviour (Károlyi et al., 2000; Tél et al., 2005; Toroczka et al., 1998). For example, it has been established (Lester et al., 2009; 2010; Metcalfe et al., 2010a; 2010b; Trefry et al., 2012) that transient Darcy flows in groundwater systems can be engineered to achieve rapid mixing by using programmed pumping activities, and this pumping schedule also can be designed to retard transport. Therefore, this new subsurface technology can fulfil different requirements of terrestrial intervention activities, such as the recovery of dissolved contaminant plumes or heat utilization in geothermal reservoirs (Cho et al., 2019; Trefry et al., 2012). While it has been recognized that time-dependent flows in engineered groundwater systems can generate significantly altered transport dynamics (Bagtzoglou & Oates, 2007; Mays & Neupauer, 2012; Piscopo et al., 2013; Rodríguez-Escales et al., 2017), the extent to which these dynamics arise in natural aquifers is still unknown, and a detailed understanding of these transport dynamics is an outstanding problem. In this study, we are interested in understanding whether such complex transport can arise in natural aquifer systems, which includes a wide range of periodically forced aquifers.

## 1.2. Problem Statement

Whilst the bulk of research concerning the transport of solutes and colloids in groundwater systems has been involved with steady groundwater flows (Bear, 1972; Whitaker, 1986); there arise many circumstances where transient flow can appear in natural groundwater systems, especially near aquifer discharge boundaries near lakes, rivers and oceans that are subject to periodic forcing. Whilst several studies (Geng et al., 2017; Li et al., 2004; Liu et al., 2018; Pool et al., 2015; Robinson et al., 2009) have considered the interplay of tidal forcing and regional groundwater flow on solute transport, to date no field studies have been attempted to explicitly resolve the kind of complex transport behaviour that can arise in these natural groundwater systems.

In this thesis, we aim to investigate whether complex mixing dynamics can arise in naturally forced aquifer systems and if present, what is their impact on solute transport. We define complex transport in Darcy flow as regions where the topology of time-averaged particle trajectories differs from the regular, open streamlines characteristic of steady Darcy flow. This includes closed transport regions where fluid elements are trapped indefinitely and regions of intense mixing where solutes are mixed at rates far in excess of steady Darcy flow. Both of these types of “complex transport” can significantly augment the transport of diffusive solutes (Adrover et al., 2002; Lester et al., 2008; Tang & Boozer, 1999) and the effective reaction rate of chemical and biological species (Károlyi et al., 2002; Tél et al., 2005; Toroczkai et al., 1998). Such complex transport and its sequential impacts have been demonstrated in many natural flows beyond groundwater systems. One common example is the complex transport structures that arise during vortex shedding in the wake of oceanic or riverine flows over islands or rocks (Károlyi et al., 2000). Non-equilibrium coexistence in plankton communities (i.e. sustained plankton blooms involving multiple plankton species) does not follow the competitive exclusion principle that arises in well-mixed environments.

Instead, complex transport due to incomplete mixing under the action of ocean currents augments the limiting biological factors, leading to the coexistence of plankton species with different predation and reptation rates (Hernández-García & López, 2004; Károlyi et al., 2000). Resolution of these complex transport dynamics in oceanic flows has also led to the development of new tools and techniques to understand, predict (and thus better manage) the spatial extent and temporal evolution of pollutants such as the gulf oil spill (Mezic et al., 2010; Thiffeault, 2010b). Such complex transport phenomena in mantle convection have also been identified as a key driver for observed heterogeneities in rock mineral composition and age at upwelling zones (Metcalf et al., 1995; Turcotte, 1997).

As stated in Section 1.1, there also is strong evidence that transient forcing can impart complex transport in engineered groundwater flows. In-situ water treatment and remediation are a demanding field technology that involves mixing or delivering reagents into affected water body for remediation of, e.g. contaminants and pollutants. The programmed rotated potential mixing (RPM) flow (Lester et al., 2009; 2010; Metcalfe et al., 2010a; 2010b; Trefry et al., 2012) is an efficient tool to control subsurface flow and transport that has recently been proven in field settings (Cho et al., 2019). This flow is generated via a series of injection/extraction wells that operate under a synchronized dipole pumping schedule. Repeated changes of fluid flow direction can have a range of kinematic effects ranging from rapid mixing to segregation and confinement of fluid regions. Specifically, the kinematic constraints associated with regular and smooth streamlines can be broken due to the transient nature of the flow, leading to transient switching of streamlines that can significantly enhance fluid mixing. However, accelerated mixing dynamics may not affect the entire flow domain, where some non-mixing “islands” may also form that represent barriers to transport and mixing, where material exchange across these regions only occur in the presence of diffusion. Thus, RPM flow can achieve either enhanced mixing or confinement for different field

treatments based upon different pumping protocols at the injection/extraction wells. Whilst these impacts have been demonstrated in field trials (Cho et al., 2019) of engineered systems such as the RPM flow; it is currently unknown whether these dynamics can arise in naturally forced systems.

For example, in the case of coastal aquifers, many previous studies have focused on understanding the mixing dynamics between freshwater and saltwater in the Ghyben-Herzberg zone due to density differences between these different mixtures (Badon-Ghyben, 1888; Herzberg, 1901). Whilst density differences may induce convective circulation patterns in the discharge zone which add spatial and temporal complexity to discharge pathways (Smith, 2004; Trefry et al., 2007; Wilson & Morris, 2012), the influence of time-dependent forcing of the coastal aquifer due to tides has not been explicitly considered. Currently, very little is understood regarding the flow and transport dynamics of transiently forced aquifer systems such as coastal, lacustrine, and riverine aquifers (Lu et al., 2013), and Motivated by the RPM flow, where periodic flow reorientation can admit enhanced mixing and confinement conditions, we believe the interplay of periodic forcing with regional groundwater flow also generate similarly complex mixing phenomena via the transient motion of streamlines. Therefore, in this thesis, we aim to investigate the capacity for transiently forced aquifer systems to display complex transport behaviour, and where such complex transport arises, uncover the underlying mechanisms, dependence on aquifer parameters and forcing dynamics, and implications for solute transport and reaction. This will be achieved by a combination of numerical modelling to simulate and visualize flow and transport in periodically forced aquifers, and theoretical tools such as Hamiltonian chaos and dynamical systems theory to understand complex transport in transiently forced aquifers.

### **1.3. Rationale**

This thesis aims to investigate whether complex transport dynamics can arise in aquifers subject to transient forcing at a discharge point, the conditions under which such transport can occur and the underlying mechanisms and impacts for solute transport, dispersion and mixing. We shall use numerical computations to simulate transport in a simple model of a transiently forced aquifer and present results regarding the prevalence of complex transport in these systems, including significant impacts on fluid trajectories, mixing dynamics and residence time distributions. We aim to identify the key dimensionless parameter groups that govern complex transport in transiently forced aquifers, and we expect these parameters will depend upon the aquifer properties, forcing and regional flow characteristics. We then aim to use these dimensionless parameters to help us understand such fundamental changes in the aquifer transport structure. Other benefits from defined parameter groups include the development of mechanistic arguments as to how and why transport varies over the parameter space, and how these governing parameters for natural systems relate to these regions of augmented transport. The thesis will also consider the interplay of advective transport, solute diffusion and dispersion and estimate the impacts of diffusion upon solute transport and the propensity for complex transport to occur in natural coastal aquifers. If complex transport is present in natural groundwater flows, then the potential for enhanced mixing and augmented transport dynamics must be considered when developing conceptual models for fluid reaction in a wide range of groundwater systems.

### **1.4. Objectives of the Research**

The main objective of this research is to understand the propensity for complex transport to occur in transiently forced aquifers and the relationships between the aquifer transport structure, forcing parameters and physical properties of the porous medium. A secondary objective is to then interpolate these impacts of these dynamics upon solute mixing,

transport, and chemical reaction. The following individual objectives are formulated to achieve the primary and secondary research objectives:

- To identify knowledge gaps regarding the mixing and transport behaviour of transient subsurface flow.
- To develop a detailed numerical dynamic simulation model which can accurately resolve the flow and transport characteristics of transiently forced aquifers.
- To explore the basic solution properties and transport complexity of this transient tidal model.
- To identify the dimensionless parameters that govern the transport complexity in transiently forced aquifer systems.
- To seek relevant techniques to elucidate, classify and quantify the complex transport structures in the problem model domain.
- To scan the dimensionless parameter space of this model and resolve the changes in the transport structure over this the “phase space.”
- To elucidate the mechanisms which govern complex transport in transiently forced aquifers
- To compare model predictions with parameters of natural coastal, lacustrine and riverine aquifers and determine the propensity for complex transport dynamics to occur in field settings.
- To determine the implications of complex transport upon dissipative solute transport, mixing and dispersion

By focusing on a series of specific research objectives above, we hope to understand the flow complexity and enhanced mixing in the transient subsurface flow, and to shed light on the following research questions in next section.

## 1.5. Research Questions

The following research questions are formulated to address the problem statement in Section 1.2 and the research objectives identified in Section 1.4:

### ***Research Question 1:***

How does the interplay of unsteady flow and porous material properties generate complex transport in subsurface flows?

#### *Significance:*

As discussed in Section 1.2, It is known that time-dependent Darcy flows can generate enhanced mixing through the crossing of streamlines in time, which provides a mechanism for complex transport behaviour in Darcian systems. The key questions here are how and why such dynamics can arise in natural aquifer systems, and what aquifer properties and forcing parameters govern the transition from regular to complex transport.

#### *Key findings:*

We find that tidal forcing in a simplified 2D model aquifer can give rise to a wide array of complex transport structures (closed flow regions, chaotic saddles, KAM islands) that differ significantly from the open, regular streamlines inherent to steady Darcy flow. These transport structures are expected to have significant implications for solute mixing, transport, dispersion, and a wide range of biogeochemical processes.

### ***Research Question 2:***

Do tidally forced systems exhibit dynamical features consistent with enhanced mixing?  
If so, how to elucidate and quantify these underlying dynamical structures?

#### *Significance:*

Unlike steady Darcy flows, where the transport dynamics can be directly visualized from the streamlines of the flow, the flow paths and coherent structures in transiently forced tidal aquifers can become too complicated to directly visualize and understand. Specific techniques are required visualize, categorize and understand those underlying dynamical structures.

*Key findings:*

We find tools and techniques from chaotic advection and nonlinear Hamiltonian dynamics (Poincare sections, identification of stable and unstable manifolds, KAM theory) can be used to visualize, classify, and understand the complex transport structures that arise in transiently forced aquifers. These tools and techniques allow identification of the mechanisms that control transport in these systems and the transition from regular to complex transport.

***Research Question 3:***

What are the key mechanisms and associated dimensionless parameters that govern transport complexity in transiently forced aquifer systems?

*Significance:*

Identification of the key mechanisms and dimensionless parameters that govern the transition from regular to complex transport is critical to understanding the origins of this phenomenon and its propensity to occur in natural systems.

*Key findings:*

From the analysis of the governing equations and model simulations, we have determined the mechanisms that govern transport complexity and their associated parameters. These parameters describe the attenuation of the tidal fluctuation into the aquifer, the strength of tidal forcing relative to that of the regional flow, and relative compressibility of the aquifer.

Secondary parameters also include the conductivity field structure such as log-variance and correlation structure. The key parameters have been couched in terms of a simple dimensionless parameter group via a simple phase diagram for the different transport structure topologies.

#### ***Research Question 4:***

Can complex transport arise in natural aquifer systems, and what are the impacts of complex transport upon solute transport?

#### ***Significance:***

An understanding of the prevalence of complex transport in natural aquifer systems is critical for the translation of the above research findings into real-world applications. To answer this question, it is necessary to estimate what proportion of coastal aquifer systems might fulfil the requirements for complex transport dynamics. Whilst much of the analysis in this thesis is concerned with the transport dynamics of purely advective particles (i.e. in the absence of diffusion or dispersion), it is also necessary to translate these research findings into predictions of solute transport, including emptying time from closed regions of the flow.

#### ***Key findings:***

From identification of the governing mechanisms and parametric dependence of complex transport, then based on global maps of tidal ranges, we are able to make coarse predictions of where complex transport is likely to occur in coastal aquifers around the world. We find that these complex transport dynamics are remarkably prevalent, where tidal forcing is sufficient to form closed or chaotic transport regions. We also find these complex transport structures that arise in natural tidally forced aquifers can trap dispersing solutes for many years. These transport and mixing dynamics are very different from those predicted by

conventional Darcy flow models, and so should be accounted for when considering transport and mixing in these systems.

## **1.6. Structure of the Thesis**

The main research work in this thesis can be divided into the following seven chapters, which are described as follows:

Chapter 1, Introduction, provides context and background information to the research topic and identifies the knowledge gap and problem statement. It also identifies the objectives of this research and relevant research questions.

Chapter 2, Literature Review, provides a survey of current knowledge relative to the problem of flow and transport in transiently forced aquifers. This includes a survey of literature regarding conventional approaches to transient groundwater flow, as well as tools and techniques for understanding flow and transport in generic transient flows, including Lagrangian kinematics and chaotic advection. This chapter also surveys current knowledge regarding the relationship between steady and transient Darcy flow and prior studies in using engineered transient flows to control transport in the subsurface.

Chapter 3, Research Methodology, describes the various computational and theoretical tools and techniques that will be used to answer the Research Questions. This includes the description of the numerical 2D aquifer model that will be used as the primary flow simulation tool, and relevant numerical solutions are explained. Key parameter groups that govern transport are also defined. Specific techniques to characterize transport and visualize and classify transport structures, such as the Poincaré section and Residence Time Distributions (RTDs) are also described.

Chapter 4, Complex Transport in Transiently Forced Aquifers, demonstrates that transiently forced heterogeneous aquifers can induce complex transport dynamics. These underlying complex dynamical structures for a single set of governing parameters are

characterized in terms of their Lagrangian topology, and the mechanisms that generate such transport phenomena are described.

Chapter 5, Parametric Variability of Complex Transport, considers the dependence of complex transport upon the governing dimensionless parameters. This is achieved by performing a range of simulations using the periodically forced 2D aquifer model to resolve the aquifer transport dynamics over the relevant parameter space. From these results, the key transport characteristics over the flow parameter space are determined and classified, and a phase diagram is developed for the different transport structures over the parameter space.

Chapter 6, Discussion and Physical Relevance for Natural Coastal Aquifers, considers the propensity for complex transport to occur in natural aquifer systems and estimates the impact of such complex transport upon solute diffusion and dispersion.

Chapter 7, Conclusions, summarizes key findings and principal conclusions and discusses the scope for future work.

## **Chapter Two**

### **2. Literature Review**

The purpose of this literature review is to survey and review the scientific literature that is relevant to the research topic of flow and transport in transiently forced aquifers. This review aims to facilitate identification of the state-of-the-art of current research relevant to this research topic and clearly identifies knowledge gaps in the existing literature. These knowledge gaps form the basis for the research questions (Section 1.5) identified in the Introduction chapter.

There exist two main bodies of literature that are relevant to this research topic. The first may broadly be classified as groundwater hydrology, which encompasses conventional approaches to understanding flow, transport and biogeochemical processes in groundwater systems. Much of this literature is found in the groundwater hydrology journals. The second body may be broadly classified as Lagrangian fluid kinematics. This is concerned with the structure and fate of fluid pathlines from a dynamical systems perspective, and the subsequent impacts upon solute mixing, dispersion and transport and active processes such as biochemical reactions. This field encompasses (but is not limited to) the field of chaotic advection (which is concerned with flows that generate chaotic fluid pathlines) and involves a number of tools and techniques to understand the structure of these flows. Much of this literature is found in fluid mechanics and physics literature and is not typically associated with groundwater flow. However, as shall be demonstrated, these tools and techniques are vital to understanding transport and mixing in many transiently forced aquifer systems.

This literature review is structured as follows. This literature review contains two main sections that correspond to the bodies of literature outlined above. Section 2.1 is concerned with the development of groundwater hydrology with respect to the research topic, and

Section 2.2 is concerned with the tools and techniques of Lagrangian fluid mechanics that are relevant to the research topic. Finally, Section 2.3 then considers how these fields relate to the research topic and identify knowledge gaps with respect to the research questions.

We outline the structure of Section 2.1 as follows. Subsection 2.1.1 is concerned with classical groundwater hydrology, from the development of Darcian theory through to modern stochastic hydrology and its application to flow and transport in heterogeneous aquifers. The associated concepts and methods then provide a theoretical basis for extension to unsteady flow conditions. Subsection 2.1.2 reviews the studies of solute transport in steady Darcy flows that use conventional methods of groundwater hydrology and aims to identify the shortcomings of these approaches in understanding complex transport. Subsection 2.1.3 is concerned with conventional groundwater hydrology methods to study solute transport and mixing in transiently forced coastal aquifers. This includes studies concerned with coastal aquifer dynamics, saltwater intrusion and coastal biogeochemical activities.

Section 2.2 is concerned with Lagrangian fluid kinematics. Subsection 2.2.1 then introduces the concept of chaotic advection, including how the Lagrangian topology of steady and unsteady flows organize fluid mixing and governs solutes transport. It is also concerned with chaotic advection in porous media, from pore-scale to potential and Darcy-scale flows. Subsection 2.2.2 is concerned with the Lagrangian kinematics of complex open flows. Whilst many flows and simple examples considered in the Lagrangian kinematics literature are closed flows, the majority of Darcy flows (including transient forced aquifers) are open. Finally, Section 2.3 identifies the main research gaps with respect to the research questions.

## **2.1. Development of Groundwater Hydrology**

### **2.1.1. Classical Groundwater Hydrology**

Groundwater hydrology was put on a quantitative basis by the pioneering experiments of Henri Darcy in 1856 (Darcy, 1856). This relied upon a spatial averaging approach to

characterizing properties of a porous medium that resulted in mathematical equations which, at certain spatial and temporal scales, could predict fluid and mass transport processes in the subsurface (Bear, 1972; Coussy, 2004). These equations were elaborated for fluid sources and sinks, and the solutions were automated for digital computers in the 1960s. Nowadays, robust computer programs (MODFLOW, FEFLOW) are widely used to solve complicated and multidimensional groundwater engineering problems (Diersch, 2013; Hughes et al., 2017).

Despite the utility of these approaches, uncertainty in groundwater predictions and model performance remains high. Fundamentally, the structure of natural porous media comprises a hierarchy of spatial scales which are difficult to measure. The signatures of fluid sources and sinks, often idealized as boundary conditions to the model, are also usually not well characterized (Delleur, 2010). These uncertainties cast doubt on the utility of forward modelling, and from the 1970s attention turned to stochastic approaches to estimate property distributions, either via geostatistical methods (Deutsch & Journel, 1992) or through model inversions (Li et al., 2018; McLaughlin & Townley, 1996).

Furthermore, it also became clear that the Darcian theory often could not adequately explain how solutes move, mix and spread in natural porous systems (Benson et al., 2006; Berkowitz et al., 2000; Gelhar, 1993; Trefry et al., 2003). Gelhar and Axness (1983) developed a predictive model for large-scale dispersion which relied on the stochastic theory. Based on this theoretical framework, continuous time random walk (CTRW) approaches (Berkowitz et al., 2006; Dentz et al., 2015) have been developed to quantify non-Fickian transport. Related formulations also include fractional derivative modelling (Benson et al., 2013; Neuman & Tartakovsky, 2009) and Lévy flights (Benson, 1998; Berkowitz et al., 2000). More recently, CTRW models have been extended to pore-scale kinematics, fluid deformation, and mixing (Dentz et al., 2016; Lester et al., 2016).

### **2.1.2. Solute Transport in Steady Darcy Flow**

The question of how to quantify solute transport in porous media is a long-standing problem that has been researched over several decades. Early analysis of tracer breakthrough experiments (Greenkorn, 1962; Lenda & Zuber, 1970) leads to the development of the classical advection-dispersion equation (ADE). This classical ADE assumed local-scale transport in homogeneous porous media is Fickian. However, early experiments (Aronofsky & Heller, 1957; Scheidegger, 1961) of breakthrough curves in homogeneous media differed significantly from the predictions from the classical ADE. Since these observations, anomalous (non-Fickian) transport has not only been found in homogeneous media (Bromly & Hinz, 2004; Major et al., 2011; Zhang & Lv, 2007) but also in laboratory experiments (Berkowitz & Scher, 2009; Levy & Berkowitz, 2003) and at the field scale in a wide range of geological formations (Adams & Gelhar, 1992; Berkowitz et al., 2008; Bianchi & Zheng, 2016; Bijeljic et al., 2013).

Anomalous transport was introduced by Bochner, Feller, etc. (Bochner, 1949; Feller, 2008; Montroll & Weiss, 1965) to account for the effects of heterogeneities in the geometrical properties (hydraulic conductivity and porosity) across all scales in porous media. Unlike the traditional transport theories, stochastic methods (such as CTRW methods) focused on particle transitions in space and time induced by the inherent spatial heterogeneity of the medium (Berkowitz et al., 2006).

Despite the success of these methods for steady flows, only a small number of studies have considered transport in transient flows. Theoretical studies (Cirpka & Attinger, 2003; Dentz & Carrera, 2005) showed that temporal fluctuations could significantly enhance transverse dispersion, leading to effective solute transport and mixing. Other studies (Dentz & Carrera, 2003; Dentz et al., 2003) focused on temporal fluctuations in the velocity field, which also leads to enhanced mixing.

### **2.1.3. Transport and Mixing in Coastal Aquifers**

Coastal aquifers are an important groundwater resource that is subject to transient forcing due to tidal fluctuations. Research into coastal aquifer transport can be broadly classified into two main topics (Robinson et al., 2018). The first topic is concerned with saline intrusion which controlled by the hydraulics of discharge and density-driven mixing at the saline/freshwater interface, and the second is concerned with the understanding of contaminant transport in groundwater systems and mitigating nutrient and toxin/pathogen pollution of sensitive coastal ecosystems.

#### ***Solute Transport and Saltwater Intrusion***

Coastal aquifers involve the mixing of groundwaters with surface waters of different geochemical quality at beaches, riverbanks and shorelines. As such, much attention has focused on determining how these waters of different geochemical origins mix and interact. Early advances by Ghyben and Herzberg (Badon-Ghyben, 1888; Herzberg, 1901; Verruijt, 1968), and Glover (1959) led to a class of sharp interface models (Llopis-Albert & Pulido-Velazquez, 2014) to characterize saline intrusion geometries at coastal aquifers. More advanced dispersive models were then formulated to study buoyancy-driven processes (Smith, 2004).

It was not until very recently that these steady models were extended to transient flows. Seasonal (Trefry et al., 2007) and tidal effects (Kuan et al., 2012) on dense saline intrusion have been considered in homogeneous formations. Several studies and simulations (Ataie-Ashtiani et al., 1999; Chen & Hsu, 2004) also have shown that relatively high ratios of tidal amplitude to aquifer depth can force seawater to intrude further. In isohaline coastal systems (where density differences are absent), much attention has been paid to how pressure disturbances (from tidal forcing) may propagate inland, expressed either as water table

(phreatic surface) fluctuations (Cartwright et al., 2003; Li et al., 1997; Nielsen, 1990; Roberts et al., 2011) or as confined diffusion waves (Ferris, 1952; Jacob, 1950; Townley, 1995).

However, incorporation of aquifer heterogeneity in such studies is rare, and aquifer homogeneity is a common simplifying assumption. Although analytical results have been derived for tidal propagation in a range of idealized layered/structured aquifer configurations (Li & Jiao, 2002; Li et al., 2001; Trefry, 1999), the effects of geological heterogeneity lead to at least one stochastic solution (Trefry et al., 2011). More recently, several studies (Pool et al., 2014, 2015) have demonstrated that mixing in the land-ocean interface is affected by combined effects between tidal amplitude, hydraulic diffusivity and aquifer heterogeneity.

### ***Biogeochemical Activity in Coastal Aquifers***

Another key question in coastal systems is how nutrients or contaminants carried by groundwater may mix and transform before discharging to receiving environments (Anschutz et al., 2009; Moore, 2010; Robinson et al., 2018). Submarine groundwater discharge (SGD) is a well-established hydrological process in which subsurface inflow of regional groundwater is discharged via coastal aquifers into the ocean (Burnett et al., 2003; Moore, 2010). This process is an essential source of nutrients (Lee et al., 2009; Luo et al., 2014; Paytan et al., 2006), metals (Bone et al., 2007; Charette & Sholkovitz, 2002; Trezzi et al., 2016), and organic contaminants (Robinson et al., 2009; Sbarbati et al., 2015; Westbrook et al., 2005) to discharge into the coastal ocean.

Early studies have used the well-developed Ghyben–Herzberg relationship (Badon-Ghyben, 1888; Herzberg, 1901) to quantify saltwater intrusion. Density differences between ground and surface waters may induce convective circulation patterns in the discharge zone which add spatial and temporal complexity to discharge pathways (Smith, 2004; Trefry et al., 2007; Wilson & Morris, 2012). This leads to fresh-sea water mixing zone with often strong

biogeochemical (salinity, pH, redox, nutrients) gradients (Charette & Sholkovitz, 2002; Moore, 1999).

More recently, the effect of transient forcing (such as tides) on biogeochemical activities in coastal aquifers has received significant attention. Several studies (Anwar et al., 2014; Santos et al., 2009) have indicated that the impact of oceanic forcing generates different mixing dynamics at the fresh/seawater interface, impacting nutrient transport and their effective reaction rates. Fluid mixing, dilution and residence times also have been correlated with enhanced biodegradation rates for contaminants in coastal aquifers subject to tidal influences (Geng et al., 2017; Robinson et al., 2009).

Over the past century, many studies of groundwater discharge processes in coastal aquifers have contributed to a conventional and well-accepted picture of flow and transport that is supported by field observations, laboratory experiments, computational and theoretical modelling. Despite this consensus, groundwater aquifers are often driven by transient flows that can lead to complex transport dynamics that cannot be resolved or understood via these conventional approaches. In the next section, we consider a range of tools and techniques to understand such complex transport from a dynamical systems perspective.

## **2.2. The Lagrangian Kinematics of Groundwater Flows**

Although steady Darcy flow in heterogeneous porous media may be considered “complex” in that it can give rise to anomalous (non-Fickian) transport, from another perspective, transport in steady Darcy flow is “simple” because this flow only admits open, regular streamlines. This simple streamline structure arises from the helicity-free nature of steady Darcy flow in locally isotropic porous media. Helicity density, defined by Moffatt (1969) as the dot product of vorticity and velocity, is a measure of the topological complexity of the streamlines of a flow. Kelvin (1884) and Arnold (1965) established that the streamlines of 3D helicity-free flows are confined to a series of coherent, non-intersecting two-

dimensional (2D) lamellar sheets. Such confinement restricts the transport dynamics of these flows, leading to algebraic deformation of fluid elements (due to the Poincaré-Bendixson theorem) and zero transverse hydrodynamic dispersion. Thus, the helicity-free nature of steady Darcy flow in locally isotropic media renders these as inherently poor mixing flows. Dentz et al. (2016) show that whilst conductivity heterogeneities can promote the fluid mixing at the Darcy scale, the kinematics of steady Darcy flow limits the stretching of fluid elements (a critical underlying mechanism) to grow at most quadratically with time.

### 2.2.1. The Concept of Chaotic Advection

Conversely, highly efficient (exponential) stretching of fluid elements can occur via chaotic advection, whereby fluid particles undertake chaotic trajectories, even when the Eulerian velocity field is laminar (Aref, 1984; Ottino, 1989). Such behaviour arises because of the advection equation for the evolution with time  $t$  of the position  $\mathbf{x}$  of a particle in a steady 3D velocity field  $\mathbf{v}(\mathbf{x})$

$$\frac{d\mathbf{x}}{dt} = \mathbf{v}(\mathbf{x}), \quad (1)$$

represents a continuous nonlinear dynamical system. A result from dynamical systems theory (Peixoto's theorem) is that a necessary condition for such continuous systems to exhibit chaotic behaviour is that they possess three or more degrees of freedom. Hence steady 3D flows, such as pore-scale flow in porous media, can exhibit chaotic advection (Lester et al., 2013).

From the Lagrangian point of view, complex mixing dynamics in steady 3D flows are caused by the fact that the advection equation (1) can generate chaotic particle orbits even if the velocity field  $\mathbf{v}$  is smooth and regular. This means that particles trajectories have high sensitivity to initial conditions and initially close trajectories separate exponentially with time, leading to exponential stretching of fluid elements (Aref, 1984; Ottino, 1989; Tél et al., 2005).

Thus, steady 3D flows that are relatively simple in the Eulerian frame can lead to complicated kinematics in the Lagrangian frame, as observed via particle tracking experiments and computations. These complex Lagrangian kinematics can then significantly impact the transport and mixing of solutes, as well as the chemical reactions and biological activity (Tél et al., 2005).

Conversely, 2D steady flows cannot be chaotic as the advection equation does not possess enough degrees of freedom to admit such behaviour. As 3D steady Darcy flows are constrained to 2D surfaces due to their helicity-free nature, these flows are also non-chaotic. The non-chaotic nature of steady 2D flows is reflected by posing these flows in terms of the streamfunction  $\psi$  as

$$v_x = \frac{\partial \psi}{\partial y}, \quad v_y = -\frac{\partial \psi}{\partial x}, \quad (2)$$

and so

$$\frac{dx}{dt} = \frac{\partial \psi}{\partial y}, \quad \frac{dy}{dt} = -\frac{\partial \psi}{\partial x}. \quad (3)$$

Hence, passively advected particles in a steady 2D flow have the same dynamics a one-degree-of-freedom Hamiltonian system, where fluid particles are confined to level sets (streamlines) of the streamfunction  $\psi$ . As such, these orbits cannot be chaotic, and the system (3) is termed *integrable*.

However, this paradigm is broken if the 2D flow is transient, and the additional degree of freedom associated with the transient flow then permits chaotic advection in 2D flows (Aref, 1984; Ottino, 1989). In this case, the streamlines of the flow can change with time, and so the trajectory of a fluid particle is no longer confined to a single streamline, and so may wander in a chaotic fashion throughout the flow domain. Thus transient flow reorientation and transient forcing have been used a mechanism to generate chaotic advection in many 2D flows (Jones & Aref, 1988; Lester et al., 2009; Trefry et al., 2012).

Metcalf et al. (2010a); (2010b) used periodically reorientation of a basic dipole flow (termed a reoriented potential mixing (RPM) flow) in a novel Hele-Shaw experiment to generate chaotic advection. When suitably programmed, this RPM flow induced highly efficient repeated stretching and folding motions of the flow field, the hallmark of chaotic advection (Ottino, 1989; Wiggins & Ottino, 2004). While the RPM flow has been developed in terms of homogeneous 2D Darcy flow (Lester et al., 2009; 2010; Metcalfe et al., 2010a; 2010b), successful application to heterogeneous porous media has been demonstrated both computationally (Trefry et al., 2012) and in field studies (Cho et al., 2019).

The RPM flow is a key hydrogeological example to demonstrate that chaotic advection in groundwater systems can be engineered via programmed pumping activities. In this flow, a synchronized dipole pumping schedule is used to drive a series of injection/extraction wells, where the neighbouring dipole is activated or deactivated subject to two key parameters: the activation time  $\tau$  and the reorientation angle  $\theta$ . Different parameter values can generate a range of Lagrangian kinematics, ranging from rapid mixing (Figure 1) to segregation and confinement (Figure 2) of fluid regions, where non-mixing “islands” may also form that represent barriers to transport and mixing. These kinematic boundaries confine and isolate flows at spatial regions, and material exchange across these regions only occur in the presence of diffusion. Thus, the RPM flow can achieve either enhanced mixing or confinement based upon different pumping protocols at the injection/extraction wells. This technology, which has recently been proven in field settings (Cho et al., 2019), can fulfil the different requirements of subsurface intervention activities, such as the recovery of dissolved contaminant plumes, improvement of reagent distribution or heat utilization in geothermal reservoirs (Aref et al., 2017; Trefry et al., 2012). An open question is whether such transport dynamics (chaotic mixing regions, non-mixing islands) can arise in natural groundwater

systems, and what are the impacts upon solute mixing, transport and dispersion, chemical reactions and biological activity.

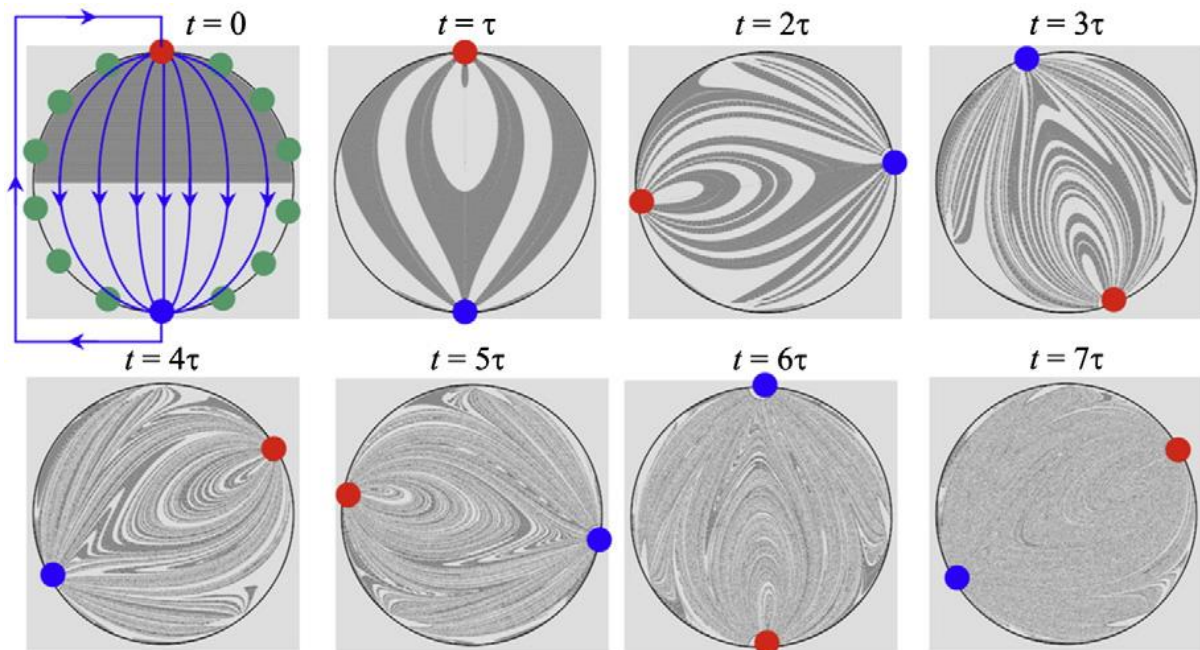


**Figure 1.** The evolutions of the dye trace during several activation times in RPM flow via reorientation of the injection (red) and extraction (blue) wells. Adapted from Trefry et al. (2012).

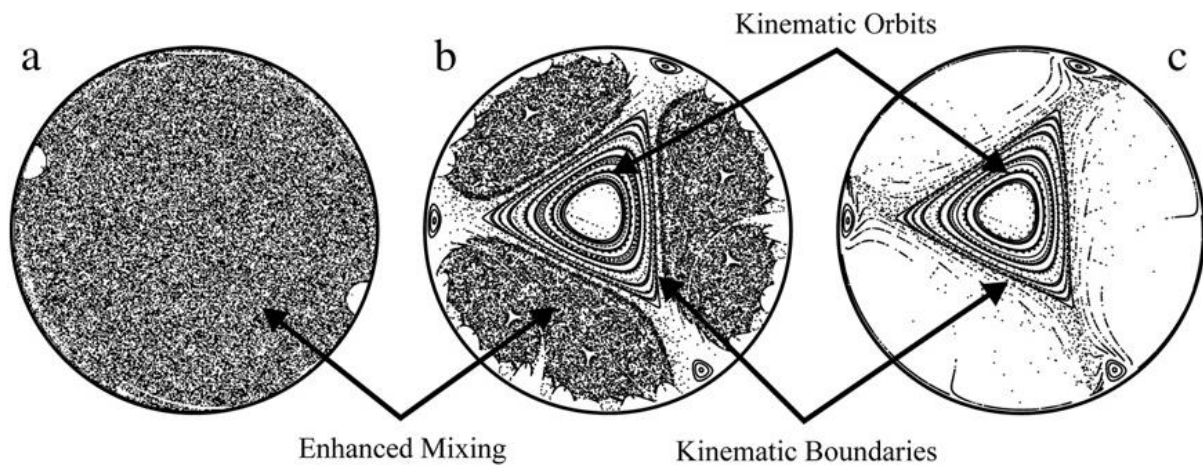


**Figure 2.** Enhanced mixing zones and kinematic boundaries in RPM flow. Adapted from Trefry et al. (2012).

### 2.2.2. Chaotic Advection in Open Flows

Whilst the RPM flow and many other prototypical examples of chaotic flows arise in closed domains, Darcy flow in natural groundwater aquifers typically involve regional flows that are open flows. As such, it is useful to consider how chaotic advection and other complex transport dynamics can arise in open flows. One example of a chaotic open flow is the von Kármán vortex street, which arises from periodic vortex shedding over a bluff body, as shown in Figure 3a, c. Here, transient flow reversal within the vortices results in the trapping of select fluid tracer particles in the wake of the flow, even though the net open flow continually passes through the flow domain. Such trapping of particles is associated with the *mixing region* of the flow; an area of intense local mixing in which some fluid elements remain for arbitrarily long times (Figure 3b).

As shown in Figure 3b, c, the mixing region of an open flow contains the intersection of the stable and unstable manifolds of the flow. The stable manifold is a temporally periodic (due to the periodicity of the flow) material line (with zero area) which is comprised of fluid tracer particles which approach the mixing region and get “trapped” within this region for arbitrarily long times ( $t \rightarrow \infty$ ). Hence, the stable manifold has profound impacts upon transport as the residence time of particles near the stable manifold diverges to infinity the closer a particle is to the stable manifold. Similar to the stable manifold, the unstable manifold (shown in Figure 3c) is a material line comprised of fluid particles which approach the mixing region as time goes backward, and so get trapped within this region in the limit ( $t \rightarrow -\infty$ ). As illustrated in Figure 3b, fluid tracer particles close to the unstable manifold eventually leave the mixing region, and so the unstable manifold can be directly observed in open flows by placing a “blob” of fluid particles over the stable manifold. Once this blob enters the mixing region, many particles are swept downstream out of the mixing region; the remainder is trapped locally near the unstable manifold. The particles which remain trapped

in the mixing region lie close to the chaotic saddle (Figure 3c), a fractal set of points given by the intersection of the stable and unstable manifolds; these points never leave the mixing region. These intersections generate continual exponential stretching and folding of fluid elements (Ottino, 1989) and chaotic advection. The mixing region can also admit non-mixing “islands” which (in contrast to the chaotic saddle) are of non-zero area, and so can trap finite amounts of fluid for infinitely long times.

Flow reversal in the open von Kármán flow can lead to complex transport dynamics that include chaotic mixing and trapping regions, both of which lead to strongly anomalous transport. We hypothesize that flow reversal in open flows associated with natural groundwater systems may also give rise to such complex transport, and so in this thesis, we focus particular attention on potential mechanisms for flow reversal in transiently forced aquifer systems.

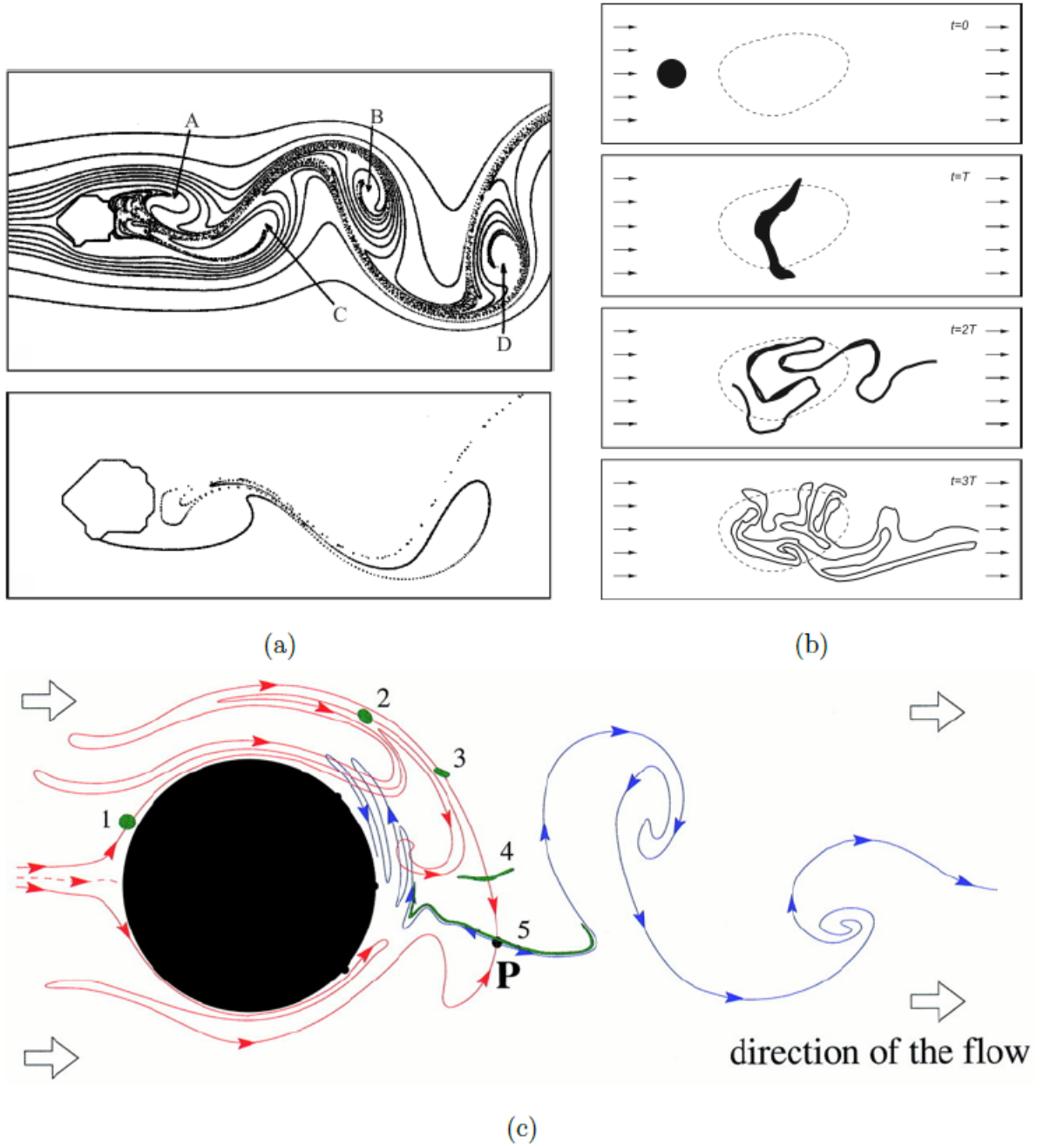


**Figure 3.** (a) (top) Numerical simulations of particle trajectories within a von Kármán vortex street emanating from Guadalupe Island. Flow reversal due to vortices corresponds to regions indicated by A, B, C, D. (bottom) Some particles orbits have long residence times due to flow reversal (adapted from Arístegui et al. (1997)). (b) Schematic depicting trapping of some fluid tracer particles within a mixing region (represented by the dotted line) in an open flow with the increasing number of flow periods  $T$  (adapted from Tél et al. (2005)). (c) Schematic of the evolution of a blob (green) of tracer particles with the number of flow periods and the

associated stable (red) and unstable (blue) manifolds in the vortex-shedding wake of a cylinder. Particles at the periodic point **P** remain trapped there indefinitely (adapted from Károlyi et al. (2002)).

### **2.3. Research Gaps**

Despite over 150 years of research, there still exist significant knowledge gaps in how solutes and contaminants migrate in hydrogeological settings. These gaps render the management, protection and/or remediation of groundwater resources economically difficult and uncertain. Whilst conventional groundwater hydrology has developed a series of sophisticated techniques and models to understand solute transport and mixing in spatially heterogeneous media; these approaches are focused almost solely on steady-state flow conditions. Although there exist many examples of groundwater aquifers being subject to significant transient forcing, very few studies have explicitly considered the impacts of such forcing upon flow and solute transport.

It was also found that mixing between fresh groundwater and recirculating seawater in coastal aquifers has long been thought to occur mainly in the dispersion zone of the salt wedge. Studies that explicitly consider the fresh/saltwater mixing zone and the effects of heterogeneity also have predominantly focused on steady-state conditions. While more recent research considered the impacts of transient forcing (e.g. tides and waves), incorporation of aquifer heterogeneity in such studies is rare, i.e. the interplay between transient forcing and aquifer properties to generate complex transport in subsurface flows is still unknown.

Moreover, these studies have not resolved the detailed nature and underlying mechanisms that lead to complex transport in subsurface systems. The tools and techniques of Lagrangian fluid kinematics, which have so far only been employed to a limited extent in conventional groundwater studies, show significant promise in their ability to visualize,

understand and classify complex transport dynamics. These approaches have previously been used to identify the ubiquity of chaotic advection in steady 3D flow at the pore-scale and design engineered subsurface interventions at the Darcy scale to control mixing and confinement of solutes. Application of these tools to understand complex transport in open flows (such as the von Kármán vortex street) shows particular promise in the ability to address the research gaps regarding flow and transport in natural groundwater systems.

## Chapter Three

### 3. Research Methodology

The purpose of this study is to show when, how and why this previously unresolved mechanism for complex transport can arise, and to point out potential implications for solute transport, dispersion and mixing. Because this complex transport mechanism is the primary focus of this study, we do not aim to present complete predictions of solute transport from a fully resolved 3D aquifer model. Rather, we limit consideration to an idealised 2D aquifer model with a multi-Gaussian conductivity field that does not include, e.g. density-driven effects. Whilst we are aware that 3D coastal aquifers and different conductivity models can generate much more complicated flow and transport phenomena (Pool et al., 2011), the reasons for using such a 2D model are: First, we shall show that the possible mechanisms and kinematics of these transport dynamics in 2D are already quite complex, and so we need to fully understand these dynamics before consideration of 3D flow and transport. Second, density-driven flows in coastal aquifers often only penetrate relatively short distances from the oceanic interface, whereas, strong tidal signals may penetrate several kilometres inland. In Appendix A, we shall show that for many common aquifers the saline wedge only penetrates a fraction of the distance of the tidal signal. As such, many of the transport structures resolved in this study are not influenced by density-driven flows at coastal boundaries. Third, as more complex transport is expected in actual 3D aquifers, we employ the idealized 2D model under the assumption that predictions of this model provide a conservative estimate for the generation of complex transport structures in 3D aquifers. This corresponds with general observations in spatially extended dynamical systems that 3D systems tend to transition to chaotic dynamics more readily than their 2D analogues, as the additional spatial dimension admits a richer set of dynamics.

In this chapter, we review the computational and analytic tools and techniques that we will use in this thesis to study transport in transiently forced aquifer systems. This chapter is organized as follows. Section 3.1 introduces an idealized 2D aquifer model that will be used for the simulation of groundwater flow and transport in a heterogeneous, tidally forced aquifer. Section 3.2 identifies the key dimensionless parameters that control the flow and transport dynamics in these groundwater systems. Section 3.3 describes the resultant non-dimensionalized Darcy flow equations and introduces an efficient numerical method for the solution of these flows that ensure flow solutions strictly obey their physical constraints. Section 3.4 considers particle tracking methods to resolve the Lagrangian kinematics of these flows and Section 3.5 contains techniques and tools to visualize, classify and understand the aquifer transport structures and Lagrangian kinematics.

### 3.1. 2D Aquifer Model

#### 3.1.1. Governing Equations

As a prototype of a tidally forced aquifer, we consider a bounded 2D domain in the  $x$ - $y$  plane shown in Figure 4 that represents an aquifer in plan view. The aquifer domain  $\mathcal{D}$  is defined by the coordinate vector  $\mathbf{x} = (x, y) \in [0, L_x] \times [0, L_y]$  and we assume the aquifer has unit thickness  $B = 1$ . For numerical simplicity and without loss of generality, we assume  $L_x = L_y = L$ , as depicted in Figure 4. Furthermore, we limit our analysis to confined flow conditions in the absence of vertical recharge and internal sources and sinks. Following Bear (1972), we write the continuity equation for an incompressible fluid in a deformable porous medium of matrix porosity  $\phi$  as

$$\frac{\partial \phi}{\partial t} + \nabla \cdot \mathbf{q} = 0, \quad (4)$$

where the Darcy flux  $\mathbf{q} = \phi \mathbf{v}$  (with  $\mathbf{v}$  the groundwater velocity) is given by the Darcy equation

$$\mathbf{q} = -K\nabla h, \quad (5)$$

where the spatially heterogeneous scalar  $K(\mathbf{x})$  is the isotropic saturated hydraulic conductivity and  $h$  is the pressure head.

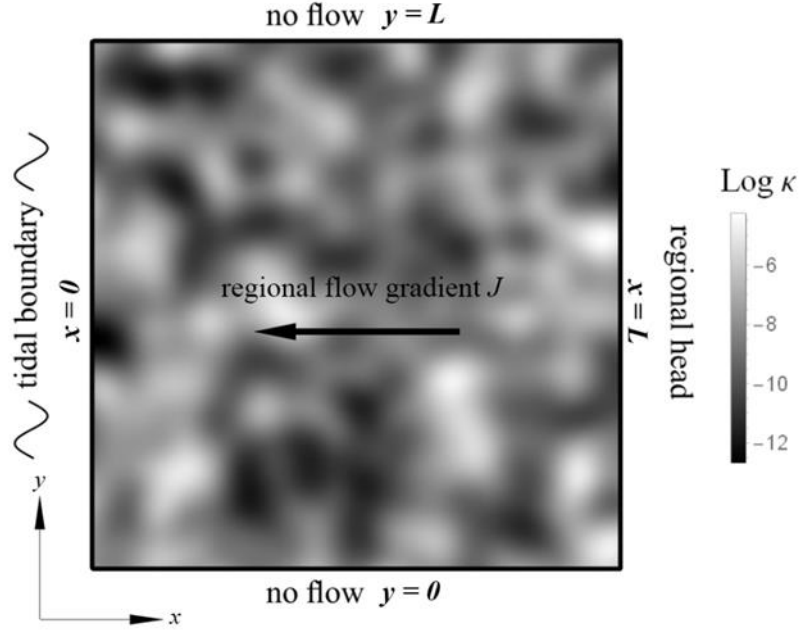


**Figure 4.** Schematic of the square aquifer domain  $\mathcal{D}$  and boundaries, showing the mean regional flow gradient  $J$  and spatial heterogeneity of  $K$ .

For 2D systems, it is usual to work in terms of the transmissivity  $T = KB$ ; however, as  $B = 1$  we use  $K$  throughout. Following conventional approaches (Bear, 1972; Coussy, 2004), we model changes in the local porosity  $\varphi$  due to fluctuations in the local head  $h$  via a linear approximation

$$\varphi(h) = \varphi_{\text{ref}} + S_s (h - h_{\text{ref}}), \quad (6)$$

where  $h_{\text{ref}}$  is the reference head at which the reference porosity  $\varphi_{\text{ref}}$  applies, and  $S_s$  is formally the specific storage. However, noting the unit aquifer thickness assumption, we henceforth replace  $S_s$  by  $S$  and refer to the storage term simply as storativity. Note that whilst the aquifer solid and fluid phases are both considered incompressible, equation (6) reflects the migration of solids particles in the aquifer due to gradients in the pressure head  $h$  (Bear,

1972; Coussy, 2004). As  $\varphi_{\text{ref}}$ ,  $h_{\text{ref}}$  and  $S$  are assumed constant, all spatial and temporal dependence of  $\varphi$  is generated by the coupling with  $h$ . Combining (4) - (6) yields the linear groundwater flow equation

$$S \frac{\partial h}{\partial t} = \nabla \cdot (K \nabla h), \quad (7)$$

subject to the no flow, inland fixed head ( $J$  the inland head gradient) and tidal boundary conditions ( $g(t)$ ), respectively,

$$\frac{\partial h}{\partial y} \Big|_{y=0} = \frac{\partial h}{\partial y} \Big|_{y=L} = 0, \quad h(L, y, t) = JL, \quad h(0, y, t) = g(t). \quad (8)$$

Solution of equation (7) subject to the boundary conditions (8) completely solves the system, and the Darcy flux  $\mathbf{q}$  is computed via (5). The inland boundary condition  $JL$  is intended to provide for mean discharge flow to the tidal boundary, i.e.  $JL > \overline{g(t)}$ , which is common in the field. Nevertheless, saline intrusion  $JL < \overline{g(t)}$  is becoming more widespread (see, e.g., Fadili et al. (2018)). Our model encompasses mean intrusion from the tidal boundary, but in this work, we restrict attention solely to discharging regional flows.

### 3.1.2. Steady and Periodic Solutions

Following Trefry et al. (2011), we assume the tidal boundary forcing function  $g(t)$  to be finite-valued and cyclic with period  $P$ , i.e.  $g(t) = g(t + P)$ . For simplicity of exposition, we assume the tidal forcing to consist of a single Fourier mode

$$g(t) = g_p e^{i\omega t}, \quad (9)$$

where  $\omega$  is the forcing frequency, and note that due to linearity, the extension to a multi-modal tidal forcing spectrum does not alter qualitative aspects of the flow problem (Trefry & Bekele, 2004). Under such forcing, the head  $h$  can be decomposed into steady  $h_s$  and periodic  $h_p$  components

$$h(\mathbf{x}, t) = h_s(\mathbf{x}) + h_p(\mathbf{x}, t) = h_s(\mathbf{x}) + h_{p,x}(\mathbf{x}) e^{i\omega t} \quad (10)$$

that satisfy the steady and periodic Darcy equations, respectively,

$$\nabla \cdot (K \nabla h_s(\mathbf{x})) = 0, \quad \nabla \cdot (K \nabla h_{p,x}(\mathbf{x})) - i\omega S h_{p,x}(\mathbf{x}) = 0, \quad (11)$$

subject to the boundary conditions

$$h_s(L, y) = JL, \quad h_s(0, y) = 0, \quad h_{p,x}(L, y) = 0, \quad h_{p,x}(0, y) = g_p \quad (12)$$

with zero flux conditions for both  $h_s$ ,  $h_{p,x}$  at the  $y = 0$  and  $y = L$  boundaries. All periodic quantities are complex in this formulation, and so the real part must be taken throughout as these are observable quantities. Henceforth we drop the notation  $h_{p,x}$  for the spatial part of the periodic head component, replacing it by  $h_p$ . Likewise, the porosity relation (6) can be decomposed into steady and periodic contributions as

$$\varphi(\mathbf{x}, t) = \varphi_s(\mathbf{x}) + \varphi_p(\mathbf{x}, t) = \varphi_{\text{ref}} + S(h_s(\mathbf{x}) - h_{\text{ref}}) + S h_p(\mathbf{x}, t), \quad (13)$$

where  $\varphi_p$  is the last term on the right-hand side of (13).

### 3.2. Dimensionless Parameters

Input parameters to the solution algorithm are the conductivity field  $K(\mathbf{x})$ , the imposed regional flux gradient  $J$ , the tidal amplitude  $g_p$ , the model frequency  $\omega$ , the storativity  $S$ , and the reference porosity  $\varphi_{\text{ref}}$ . It is useful to nondimensionalize the governing equations by identifying the key dimensionless parameters, which are summarized as follows.

#### 3.2.1. Heterogeneity Model

The choice of conductivity distribution deserves some discussion. Characterization and representation of physically realistic conductivity fields is a non-trivial task, and since the early work of Delhomme (1979) a variety of geostatistical inversion techniques have been developed to make the best use of the often sparse field measurements (Deutsch & Journel, 1992; Ezzedine et al., 1999; Fienen et al., 2009). In contrast, in the present work, we seek to identify transferable attributes of tidally forced flows, so our emphasis is on understanding how simple models of spatial heterogeneity may potentially contribute to enhanced mixing

processes. Our expectation is that if enhanced mixing is detected in simple fields, then similar mixing dynamics will likely also appear in more sophisticated, better conditioned (and more representative) geostatistical fields. Thus, we restrict attention to random spatial processes governed by Gaussian autocorrelation functions, where the mean ( $K_{\text{eff}}$ ), log-variance ( $\sigma_{\log K}^2$ ) and integral scale ( $\lambda$ ) are sufficient to describe the statistics.

### 3.2.2. Townley Number $\mathcal{T}$

Townley (1995) shows that the dimensionless *Townley number*  $\mathcal{T}$  captures the relative timescales of diffusion  $\tau_D = L^2/D_{\text{eff}}$  and tidal forcing  $\tau_T = 1/\omega$  in a finite tidal aquifer as

$$\mathcal{T} \equiv \frac{\tau_D}{\tau_T} = \frac{L^2 S \omega}{K_{\text{eff}}} = \frac{2\pi L^2}{D_{\text{eff}} P}, \quad (14)$$

where  $D_{\text{eff}} \equiv K_{\text{eff}}/S$  is the effective aquifer diffusivity. As is well understood for homogeneous aquifers (see following sections), low values of  $\mathcal{T}$  provide conditions conducive to the propagation of tidal signals far into the aquifer with low phase lags, while high  $\mathcal{T}$  values ensure rapid attenuation (damping) of tidal amplitudes and phase lags growing rapidly with increasing penetration distance. Here, for convenience, we are interested in systems where  $\mathcal{T}$  is large enough to ensure that finite-aquifer effects are negligible in the tidal forcing zone.

### 3.2.3. Tidal Strength $\mathcal{G}$

We also characterize the relative strength of the tidal forcing amplitude  $g_p$  to the inland regional gradient  $J$ , thereby defining the *tidal strength*

$$\mathcal{G} \equiv \frac{g_p}{JL}, \quad (15)$$

such that  $\mathcal{G} = 0$  corresponds to conventional steady discharge to a constant fixed head boundary. From (11), (12)  $\mathcal{G} = \langle ||\mathbf{q}_p|| \rangle / \langle ||\mathbf{q}_s|| \rangle$  in the limit of slow forcing  $\omega \rightarrow \infty$ , where the angled brackets denote a spatial average over the flow domain. Hence the tidal strength  $\mathcal{G}$

controls the propensity for flow reversal over a forcing cycle. Indeed, it can be shown numerically that the product of tidal strength and aquifer log-conductivity variance

$$\mathcal{G} \sigma_{\log K}^2 = \frac{g_p}{JL} \sigma_{\log K}^2 \quad (16)$$

is strongly correlated with the density of canonical flux ellipses in the tidally active zone, where  $\mathcal{G} \sigma_{\log K}^2 = 0$  corresponds to flow in aquifers with homogeneous hydraulic conductivity or zero tidal forcing.

#### 3.2.4. Tidal Compression Ratio $\mathcal{C}$

The final main dimensionless parameter is the tidal compression ratio which characterizes the relative change in porosity of the aquifer from its reference state  $(\varphi_{\text{ref}}, h_{\text{ref}})$  under a pressure fluctuation of the same magnitude as the tidal forcing amplitude ( $\Delta h = g_p$ ), that is,

$$\mathcal{C} \equiv \frac{\varphi - \varphi_{\text{ref}}}{\varphi_{\text{ref}}} = \frac{Sg_p}{\varphi_{\text{ref}}}, \quad (17)$$

such that  $\mathcal{C} = 0$  corresponds to an incompressible aquifer and  $\mathcal{C} \ll 1$  corresponds to a weakly compressible aquifer. These limits shall prove useful in understanding how chaotic mixing arises in strongly compressible aquifers, that is,  $\mathcal{C} \lesssim 1$ . Note that the linear approximation (6) breaks down for values of the tidal compression ratio close to unity, leading to the possibility of predictions of negative porosity and other non-physical effects.

Thus, the dimensionless parameter set  $\mathcal{Q} \equiv (\mathcal{T}, \mathcal{G}, \mathcal{C})$  controls the dynamics of a periodically forced aquifer. In combination with the set of statistical parameters  $\chi$  which define the dimensionless hydraulic conductivity field (where for the log-Gaussian conductivity field in this study  $\chi = (\sigma_{\ln K}^2, \lambda)$ ), this parameter set completely defines the dimensionless transient tidal forcing problem, and so these parameters serve as model inputs.

In this way, the set of dynamical parameters  $Q$  can then be translated between aquifer models with different conductivity structures (as defined by  $\chi$ ).

### 3.2.5. Heterogeneity Characters $\mathcal{H}_t$ and $\mathcal{H}_x$

In addition to the input parameters sets  $Q$  and  $\chi$  there also exist two *characteristic* dimensionless parameters,  $\mathcal{H}_t$  and  $\mathcal{H}_x$ , that are functions of the input parameters. These heterogeneity characters are completely defined by  $Q$  and  $\chi$  and aid understanding of how the aquifer transport dynamics relate to the heterogeneous structure of the conductivity field.

Heterogeneous flow in the aquifer model is governed by the interaction of two physical processes with independent time scales. First, through the imposed regional gradient the inland part of the domain displays a mean *drift velocity*  $v_{\text{drift}} \equiv -K_{\text{eff}}J/\phi_{\text{ref}}$  toward the tidal boundary where the fluid ultimately discharges. Fluid parcels advecting within this mean drift sample successive conductivity heterogeneities on a time scale of  $t_{\text{drift}} = \lambda/|v_{\text{drift}}| = \lambda\phi_{\text{ref}}/K_{\text{eff}}|J|$ . Second, the tidal boundary oscillates with period  $P$ . Thus we define the *temporal character* of the heterogeneous flow,  $\mathcal{H}_t$ , as the ratio of the drift time scale to the tidal period, i.e.  $\mathcal{H}_t \equiv t_{\text{drift}}/P = t_{\text{drift}}\omega/2\pi$ . When  $\mathcal{H}_t \ll 1$  the system is said to be *discharge dominated*, and the groundwater flow displays minimal lateral (longshore) deflections and residence time variances scale with  $\sigma_{\log K}^2$ . For  $\mathcal{H}_t \gg 1$  the system is *tidally dominated* with low drift velocity: although fluid parcels experience many tidal periods during the journey to the discharge boundary, lateral deflections of the flow paths are suppressed due to the low velocity. Where  $\mathcal{H}_t \approx \mathcal{O}(1)$  the system is in *temporal resonance* and, heuristically, there is maximum potential for local elliptical velocity orbits (see Section 4.3 in Chapter 4, Figure 11) to induce folding of flow paths and the development of complex transport structures.

We also introduce the *spatial character* of the heterogeneous flow,  $\mathcal{H}_x$ , as a measure of the density of heterogeneities in the tidally affected zone. We define the *tidally affected zone*

as the zone from the tidal boundary to the interior point,  $x_{\text{taz}}$ , where the amplitude of the tidal oscillation ( $g_p$ ) matches the mean local steady head, i.e.  $|h_p(x_{\text{taz}}, t)| = h_s(x_{\text{taz}})$ . This value  $h_p$  can be conveniently estimated using a one-dimensional homogeneous model (Townley, 1995), fixing  $x_{\text{taz}}$  independently of the heterogeneous numerical solution. The relevant analytical solutions are

$$h_s(x) = xJL; h_p(x, t) = g_p \cosh[(x - 1)\sqrt{i\mathcal{T}}] \text{sech}[\sqrt{i\mathcal{T}}] e^{i\omega t}, \quad (18)$$

which are easily established by integration (Trefry et al., 2011). It is straightforward to show that  $x_{\text{taz}}$  is the root of

$$\mathcal{G} \sqrt{\frac{\cos((x_{\text{taz}} - 1)b) + \cosh((x_{\text{taz}} - 1)b)}{\cos(b) + \cosh(b)}} - x_{\text{taz}} = 0, \quad (19)$$

where  $b = \sqrt{2\mathcal{T}}$ . We define the spatial character by  $\mathcal{H}_x \equiv x_{\text{taz}}/\lambda$ , which expresses the number of spatial correlation scales of  $K$  that fit within the width of the tidally affected zone (perpendicular to the tidal boundary). The higher  $\mathcal{H}_x$ , the greater the number of conductivity contrasts encountered by the discharging flow while subject to strong elliptical motions.

### 3.3. Nondimensional Governing Equations

#### 3.3.1. Dimensionless Model

Based on these dimensionless parameters, we write the governing equations (11) and (12) in dimensionless form via the rescalings  $\mathbf{x}' = (x', y') = \mathbf{x}/L = (x/L, y/L)$ ,  $h' = h/(JL)$ ,  $t' = t\omega$ ,  $\kappa = K/K_{\text{eff}}$  yielding the nondimensional governing equations (where primes are henceforth dropped)

$$\nabla \cdot (\kappa \nabla h_s(\mathbf{x})) = 0, \quad \nabla \cdot (\kappa \nabla h_p(\mathbf{x})) - i\mathcal{T} h_p(\mathbf{x}) = 0, \quad (20)$$

and non-dimensional boundary conditions on  $\mathcal{D}$  (now the unit square)

$$h_s(1, y) = 1, \quad h_s(0, y) = 0, \quad h_p(1, y) = 0, \quad h_p(0, y) = \mathcal{G}. \quad (21)$$

The parameter set  $(\mathcal{T}, \mathcal{G})$  governs the dimensionless Darcy flux  $\mathbf{q}' = \mathbf{q}/(JK_{\text{eff}})$ . Conversely, the tidal compression ratio  $\mathcal{C}$  governs scaling of the dimensionless velocity as

$$\mathbf{v}' = \mathbf{v} \frac{\varphi_{\text{ref}}}{JK_{\text{eff}}} = \mathcal{C} \mathbf{q}'. \quad (22)$$

Hence the Lagrangian kinematics of the aquifer model are governed by dimensionless conductivity field  $\kappa(\mathbf{x})$  and the dynamical parameter set  $\mathcal{Q} \equiv (\mathcal{T}, \mathcal{G}, \mathcal{C})$ .

### 3.3.2. Fluid Velocity

As fluid particles and passive tracers are advected by the groundwater velocity field,  $\mathbf{v} = \mathbf{q}/\varphi$ , in this study we are primarily interested in the mixing and transport properties of  $\mathbf{v}(\mathbf{x}, t)$ . For finite  $S > 0$ ,  $\varphi$  varies with space and time through its dependence on  $h$ , and it is not possible to separate  $v$  into steady and periodic terms; rather,  $\mathbf{v}$  is given by

$$\mathbf{v}(\mathbf{x}, t) = \frac{\mathbf{q}(\mathbf{x}, t)}{\varphi(\mathbf{x}, t)} = \frac{\mathbf{q}_s(\mathbf{x}) + \mathbf{q}_p(\mathbf{x}, t)}{\varphi_s(\mathbf{x}) + \varphi_p(\mathbf{x}, t)}. \quad (23)$$

This velocity formulation is consistent with (7) where the compression term acts only on net storage; head-dependent alterations to the conductivity  $K$  are also plausible but here are neglected in the context of confined aquifers characterized by small  $S$ .

### 3.3.3. Numerical Method for Fluid Velocity Field

We describe the numerical method used to solve the dimensionless governing equations (20) for the steady and periodic components of the pressure head. We require interpolated values of the Darcy flux and fluid velocity for locations away from the finite difference (FD) grid that *exactly* satisfy (20), as even minor errors violate the measure-preserving nature of the system and lead to spurious results (discussed below). While the FD method computes (20) to within machine precision with respect to the FD stencil (which approximates the differential operators in (20)), interpolated (off-grid) values of  $\mathbf{q}_s(\mathbf{x}, t)$  and  $\mathbf{q}_p(\mathbf{x}, t)$  do not exactly satisfy the continuous differential operators of the governing equations. From the

continuity equation (4), the steady Darcy flux  $\mathbf{q}_s(\mathbf{x})$  must be exactly divergence-free and, accordingly, as described in this section, we developed a spline interpolation streamfunction representation of  $\mathbf{q}_s(\mathbf{x})$ . The periodic flux  $\mathbf{q}_p(\mathbf{x}, t)$  also must individually satisfy the continuity equation (4); this is achieved by interpolating  $\mathbf{q}_p(\mathbf{x})$  from the FD grid and then computing the periodic contribution to the porosity  $\varphi_p$  from the divergence of  $\mathbf{q}_p(\mathbf{x})$ , also described in this section. By constructing  $\mathbf{q}$  and  $\varphi$  in this manner, we ensure the solution obeys the continuity equation exactly, and the subsequent velocity  $\mathbf{v}$  conserves mass to machine precision at *all* interior locations.

When considering the Lagrangian kinematics of these flow fields, evaluations of velocity vectors for particle tracking purposes require much greater accuracy than is commonly provided in many groundwater modelling investigations. This is because the resolution and identification of Lagrangian structures can require a combination of long particle travel times and fine spatial resolution, and it is important that the Hamiltonian structure of the advection equation is preserved to prevent spurious particle tracking. Even tiny violations of mass conservation can lead to serious errors such as spurious sources and sinks in the flow domain and violation of Lagrangian topology (Ravu et al., 2016). Numerical calculations of the Darcy flux vector at arbitrary locations in the problem domain can be problematic since calculations require both differentiation and interpolation of discretised variables ( $\kappa$  and  $h$ ). This numerical method solves the tidal heads via a finite difference approach and then generates heads, fluxes and porosities as spatially smooth and continuous scalar fields that are consistent with the relevant physical constraints (4) and (6). These continuous variables allow the fluid velocity field to be evaluated to an accuracy sufficient to support the required analyses of Lagrangian flow characteristics without spurious effects.

The steady and periodic head solutions of (20) and (21) calculated according to the numerical scheme in (Trefry et al., 2010) are presented as head distributions  $h_s$  and  $h_p$

evaluated on a regular (square) finite difference grid with spatial increment  $\Delta$ . The corresponding flux distributions  $\mathbf{q}_s$  and  $\mathbf{q}_p$  are constructed by finite differences according to

$$\begin{aligned}\mathbf{q}_s(\mathbf{x}_{m,n}) &= (-\kappa_x^+ [h_s(\mathbf{x}_{m+1,n}) - h_s(\mathbf{x}_{m,n})], -\kappa_y^+ [h_s(\mathbf{x}_{m,n+1}) - h_s(\mathbf{x}_{m,n})]) / \Delta \\ \mathbf{q}_p(\mathbf{x}_{m,n}) &= (-\kappa_x^+ [h_p(\mathbf{x}_{m+1,n}) - h_p(\mathbf{x}_{m,n})], -\kappa_y^+ [h_p(\mathbf{x}_{m,n+1}) - h_p(\mathbf{x}_{m,n})]) / \Delta\end{aligned}\quad (24)$$

where  $m$  and  $n$  index the finite difference nodes in the  $x$  and  $y$  directions, respectively, and  $\mathbf{x}_{m,n} = (x_m, y_n)$ . For the present 2D problem, the mid-nodal conductivity values may be estimated by the geometric averages:

$$\begin{aligned}\kappa_x^+ &= \sqrt{\kappa_{m+1,n} \kappa_{m,n}} \\ \kappa_y^+ &= \sqrt{\kappa_{m,n+1} \kappa_{m,n}}.\end{aligned}\quad (25)$$

The flux estimation scheme (24) provides error residuals identical to those of the head solution. From equation (6), the nodal porosity is then expressed as

$$\begin{aligned}\varphi(\mathbf{x}_{m,n}, t) &= \varphi_{\text{ref}} + S(h_s(\mathbf{x}_{m,n}) - h_{\text{ref}} + h_p(\mathbf{x}_{m,n})e^{i\omega t}) \\ &= \varphi_s(\mathbf{x}_{m,n}) + \varphi_p(\mathbf{x}_{m,n}, t).\end{aligned}\quad (26)$$

To accurately resolve the transport structures within the aquifer, the continuity equation (4) must be satisfied with machine precision at all locations (not just at the finite difference nodes) and times in the model system. Noting that, formally, the Darcy flux  $\mathbf{q}$  and porosity  $\varphi$  satisfy (23) and (13), respectively, we see that the continuity equation can be expressed in terms of the continuous quantities  $\mathbf{q}_s(\mathbf{x})$ ,  $\mathbf{q}_p(\mathbf{x})$  as:

$$\nabla \cdot (\mathbf{q}_s + \mathbf{q}_p e^{i\omega t}) + \frac{\partial(\varphi_s + \varphi_p e^{i\omega t})}{\partial t} = 0. \quad (27)$$

Expanding this equation and noting the time-independence of the results yields the following two identities for exactly mass-conserving flow in our model periodic system:

$$\nabla \cdot \mathbf{q}_s = 0, \quad \nabla \cdot \mathbf{q}_p + i\omega \varphi_p = 0. \quad (28)$$

This result shows that the periodic component of the Darcy flux induces a bounded oscillation in the local porosity which, in turn, modulates the advective velocity via (13). It is usual to generate continuous Darcy flux distributions by interpolating between the finite

difference nodal fluxes. If, however, our interpolated estimate of the steady Darcy flux component is not precisely divergence-free, i.e.  $\nabla \cdot \mathbf{q}_s = \epsilon \neq 0$ , where  $\epsilon$  is independent of time, then the continuity equation becomes

$$\frac{\partial \varphi}{\partial t} = -\nabla \cdot (\mathbf{q}_p e^{i\omega t}) - \epsilon, \quad (29)$$

which provides for unbounded growth of  $\varphi$  as  $t \rightarrow \infty$ , resulting in unphysical flow paths. To remedy this situation, we impose equations (28) as exact constraints on the interpolated numerical solutions for  $\mathbf{q}$  and  $\varphi$  via the following three-step process.

***Step 1: Enforcing Zero Divergence for  $\mathbf{q}_s$  via a Streamfunction Approach***

Consider the steady component of the Darcy flux,  $\mathbf{q}_s$ , with nodal values  $\mathbf{q}_{s,m,n} = (\mathbf{q}_{s,m,n}^x, \mathbf{q}_{s,m,n}^y)$  and continuous vector interpolation  $\mathbf{q}_s^{\text{int}}(x, y) = (q_{s,x}^{\text{int}}(x, y), q_{s,y}^{\text{int}}(x, y))$ . Even if  $\mathbf{q}_s^{\text{int}}$  exactly reproduces the numerical fluxes at the finite difference node points it does not follow that the interpolation necessarily provides zero divergence at all locations  $(x, y)$ . We address this by constructing an effective streamfunction,  $\Psi$ , for  $\mathbf{q}_s$  based on  $\mathbf{q}_s^{\text{int}}$  and then differentiating  $\Psi$  to generate modified flux components  $\mathbf{q}_{s,x}^*$  and  $\mathbf{q}_{s,y}^*$  according to

$$\mathbf{q}_{s,x}^* \equiv \frac{\partial \Psi}{\partial y}, \quad \mathbf{q}_{s,y}^* \equiv -\frac{\partial \Psi}{\partial x}. \quad (30)$$

This results in an explicitly divergence-free flux distribution since

$$\nabla \cdot (\mathbf{q}_{s,x}^*, \mathbf{q}_{s,y}^*) \equiv \frac{\partial^2 \Psi}{\partial x \partial y} - \frac{\partial^2 \Psi}{\partial y \partial x} = 0. \quad (31)$$

The effective streamfunction  $\Psi$  is calculated by first performing a spline interpolation of the x- and y-components of the steady flux  $\mathbf{q}_s^{\text{int}}$  over the finite difference grid. Integration of these interpolants over a square grid (termed an integration grid) with spacing  $\Delta_N$ , yielding the two datasets:

$$\begin{aligned}\Psi_{m,n}^{(x)} &= \int_{y_0}^{y_n} q_{s,x}^{\text{int}}(x_0 + m \Delta_N, y') dy' , \\ \Psi_{m,n}^{(y)} &= - \int_{x_0}^{x_m} q_{s,y}^{\text{int}}(x', y_0 + n \Delta_N) dx' .\end{aligned}\tag{32}$$

Here each integral is performed by quadrature over the integration grid. These datasets provide two independent estimates of the streamfunction  $\Psi$  over the finite difference grid as

$$\begin{aligned}\Psi_{m,n}^{(1)} &= \Psi_{m,n}^{(x)} + \Psi_{m,0}^{(y)} , \\ \Psi_{m,n}^{(2)} &= \Psi_{m,n}^{(y)} + \Psi_{0,n}^{(x)} ,\end{aligned}\tag{33}$$

where we note that the streamfunction is arbitrary up to an additive constant, as expected, these estimates converge with increasing resolution of both the finite difference and integration grids.

Rather than choose between these estimates, we assemble the streamfunction in discrete form by the simple average  $\Psi_{m,n} = (\Psi_{m,n}^{(1)} + \Psi_{m,n}^{(2)})/2$ . The discrete streamfunction  $\Psi_{m,n}$  is then converted to final continuous form  $\Psi(x, y)$  via spline interpolation and the modified flux components calculated via (30).

### ***Step 2: Enforcing the Continuity Equation on $\mathbf{q}_p$ and $\varphi_p$***

In order to ensure that the transient form of the continuity equation (28) is also satisfied, we fix the modified transient porosity component  $\varphi_p^*$  by setting  $\varphi_p^*(x, y) = -(i\omega)^{-1} \nabla \cdot \mathbf{q}_p^{\text{int}}(x, y)$ , where  $\mathbf{q}_p^{\text{int}}$  is the spline interpolated transient flux solution based on the finite difference nodal values for  $\mathbf{q}_p$ . The total modified Darcy flux is constructed as  $\mathbf{q}^*(x, y, t) = \mathbf{q}_s^*(x, y) + \mathbf{q}_p^{\text{int}}(x, y) e^{i\omega t}$  and the total modified porosity as  $\varphi^*(x, y, t) = \varphi_s^{\text{int}}(x, y) + \varphi_p^*(x, y) e^{i\omega t}$ . In turn, the periodic head  $h_p^*$  is fixed by (13), (23), yielding  $h^*(x, y, t) = h_s^{\text{int}}(x, y) + h_p^*(x, y) e^{i\omega t}$ . Thus, we identically satisfy the continuity equation and compressibility relation over the problem domain and obtain an exactly mass-conserving velocity field  $\mathbf{v}^* = \mathbf{q}^*/\varphi^*$  that incorporates the underlying tidal groundwater hydraulics.

In general, the updated variables differ from those interpolated directly from the finite difference flux solution but retain the character of the underlying numerical solution. Figure 5 compares three arbitrary flow paths calculated using  $\mathbf{v}^{\text{int}}$  with the counterpart path calculated using  $\mathbf{v}^*$  with  $\Delta_N=1/500$ .

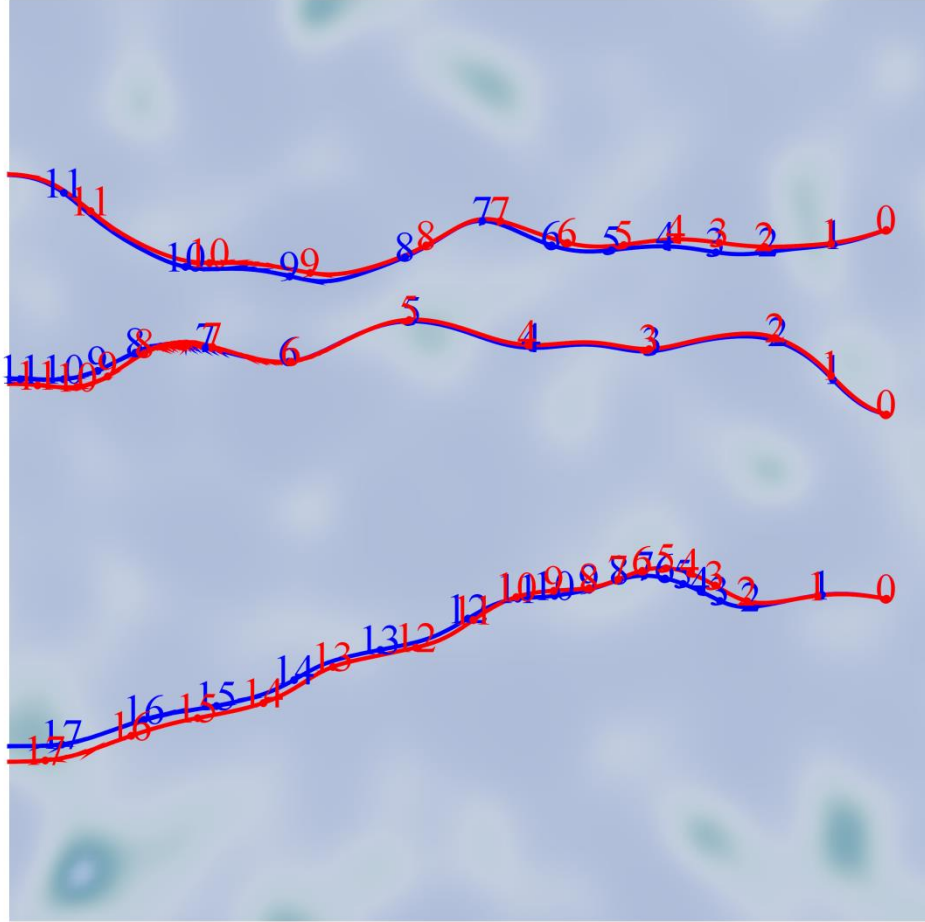


**Figure 5.** Comparison of flow paths integrated forward in time using simple interpolation of finite difference solutions (red) and full CE-corrected solutions (blue) superimposed on the associated  $\kappa$  field (shaded). Numbering refers to the number of elapsed periods  $P$  ( $\times 100$ ) along each path, starting at  $t = 0$  at the points to the right.

### *Step 3: Checking Self-Consistency of the Adjusted Dependent Variables*

The previous two steps have ensured that the updated dependent variables ( $h^*, \mathbf{q}^*, \varphi^*$ ) satisfy the continuity equation and the compressibility relation, but at the cost of slightly

perturbing the variables from their finite difference values. We assess the nature and magnitude of the perturbations using the Darcy equation (5) as a reference. The updated heads and fluxes will be consistent with a Darcian process if the updated flux vector  $\mathbf{q}^*$  and the gradient of the updated head  $\nabla h^*$  are aligned. This alignment is tested by calculating the azimuths  $\theta_{\nabla h^*} = \text{ArcTan}(\nabla h_y^* / \nabla h_x^*)$  and  $\theta_{q^*} = \text{ArcTan}(q_y^* / q_x^*)$  of the updated steady flux and steady head gradient vectors, with zero azimuth chosen to lie in the mean flow direction (negative  $x$  direction). Azimuth plots were compiled by sampling the updated head and flux distributions at the finite difference node locations and plotting the sample values against each other, and comparing this with the discrete solution counterpart.

Results of this assessment are shown in Figure 6 for two different spatial correlation lengths  $\lambda/\Delta$  and  $(N_x, N_y) = (64, 64)$ . In each case, the finite difference solution provides an azimuth plot with non-zero mean discrepancy between the head gradient and flux vectors, which is a consequence of the discrete heads being evaluated at grid nodes (with specified conductivity values) and the discrete fluxes at mid-nodal locations (with spatially averaged conductivity values). Thus the finite difference azimuth plots provide a lower bound to the error of the updated azimuth distributions. For coarse meshes with  $\lambda/\Delta = 2$ , the updated azimuth plot shows wide dispersion, including many samples with opposed azimuths (approximately 15% of the flux and head gradient vectors have opposite flow directions); however, for finer meshes with  $\lambda/\Delta = 12$ , the updated azimuths are more tightly aligned ( $< 1.4\%$  opposed flows). Figure 7 displays the resolution-dependence of the mean azimuthal discrepancy, showing that the mean azimuth error drops to less than  $1^\circ$  for  $\lambda/\Delta \geq 8$  for  $\sigma_{\log \kappa}^2 = 1$ . The results also depend on the conductivity variance  $\sigma_{\log \kappa}^2$ : increasing variances worsen the azimuthal discrepancy.

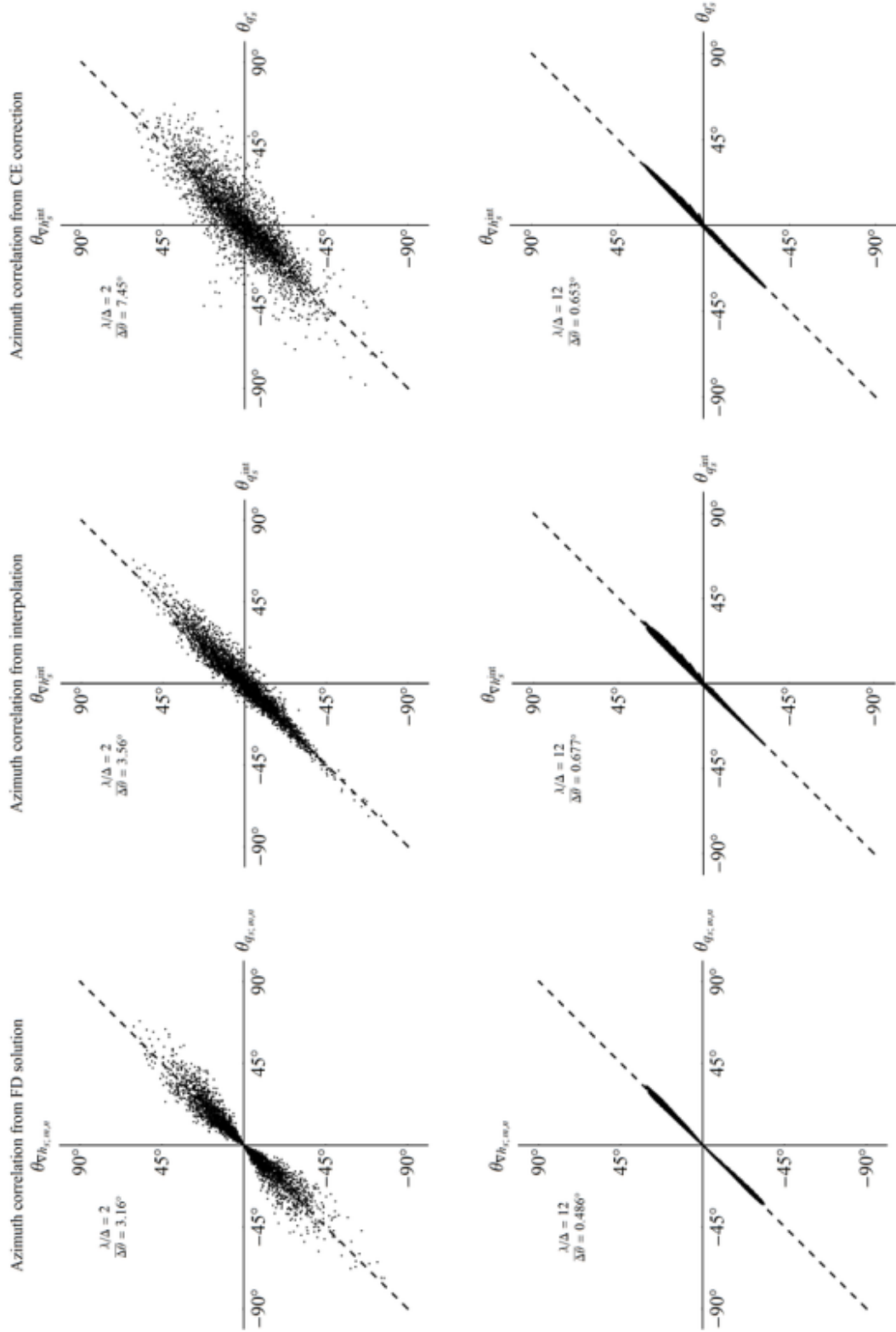


**Figure 6.** Self-consistency checks of azimuths from steady fluxes and head gradients for the finite difference solution (left column), interpolated solution (centre column) and the updated flux (right column) evaluated for two different correlation lengths (upper and lower rows). The numerical scheme gives better results at larger correlation lengths.

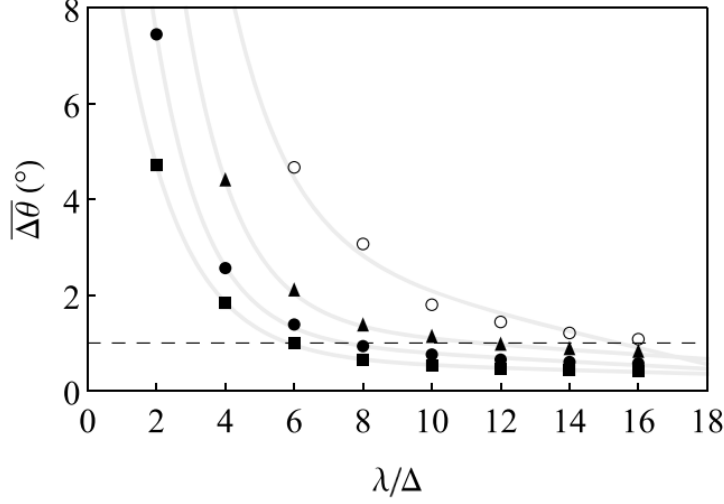


**Figure 7.** Dependence of mean azimuthal difference  $\overline{\Delta\theta}$  for the updated fluxes on the correlation length  $\lambda/\Delta$  of a set of realizations of the input conductivity field with variances  $\sigma^2_{\log\kappa} = 1/2$  (squares), 1 (dots), 2 (triangles) and 4 (circles). Curves are fitted to each set of points to aid the eye, and the acceptability cutoff is set at  $1^\circ$  (dashed line).

These results indicate that our numerical scheme generates accurate Darcian solutions that strictly obey the necessary continuity and compressibility constraints so long as the spatial conductivity variations are sufficiently well resolved by the finite difference grid and thus the discrete set of input  $\kappa$  values. In order to guarantee the acceptable quantitative performance of the physical constraints and laws in our simulations, it is useful to adopt a maximum permissible mean azimuthal discrepancy, e.g.  $1^\circ$ . In this case, for unit variance  $\sigma^2_{\log\kappa} = 1$  attention would be confined to cases where  $\lambda/\Delta \geq 8$  as indicated in Figure 7 (see dashed line).

### 3.4. Particle Tracking Methods and Kinematics

#### 3.4.1. Lagrangian Kinematics

Fluid mixing and transport are direct properties of the *Lagrangian kinematics* of the aquifer, which describe the evolution of non-diffusive, passive tracer particles advected by the velocity field as

$$\frac{d\mathbf{x}}{dt} = \mathbf{v}(\mathbf{x}, t). \quad (34)$$

Whilst the advection equation (34) appears simple, under certain conditions, it can give rise to distinct regions with chaotic particle trajectories; i.e. solutions to (34) can exhibit chaotic dynamics. These chaotic regions may be interspersed with regions of regular transport (e.g. smooth, regular streamlines), and these distinct regions of regular and chaotic dynamics define the *Lagrangian topology* of the flow. Resolution and classification of these diverse regions provide deep insights into the mixing and transport properties of aquifer flow (Aref et al., 2017).

We use (34) extensively to resolve the Lagrangian kinematics and topology of the aquifer flow. Whilst it may appear incongruous to study mixing in the absence of particle diffusion or dispersion, we deliberately omit particle diffusion as we wish to clearly observe the underlying Lagrangian kinematics and Lagrangian topology in the absence of diffusive noise. Throughout this study, we use the term “mixing” to denote the mixing of particle trajectories (akin to the mixing of coloured balls) rather than the classical definition made in terms of a decrease in concentration variance or increase in concentration entropy (Kitanidis, 1994), although both can be recovered through coarse-grained averages over sets of fluid particle trajectories.

### 3.4.2. Lagrangian Particle Tracking

In order to address our study of Lagrangian kinematics, we need to generate accurate solutions to tidally forced groundwater systems. In principle, any groundwater flow package can be used to solve the governing equations (11) - (13), but extra care must be taken to assure that accurate, cyclo-stationary solutions satisfy the periodic equation in (11). The finite difference (FD) algorithm of Trefry et al. (2010) is second-order convergent and efficiently provides direct solutions (i.e. without time stepping) for both steady and periodic equations. Modification of this method to ensure mass conservation is described in Subsection 3.3.3. Given the solution of (20), (21) via this FD method, the Darcy flux  $\mathbf{q}$  and fluid velocity  $\mathbf{v}$  are computed via (5) and (23), respectively. To probe the Lagrangian kinematics of these flows, we integrate the advection equation (34) for many passive fluid tracers over many millions of periods of the flow. As shall be shown, in conjunction with the tools and techniques of *measure-preserving* dynamical systems (chaos theory), such analysis in the *Lagrangian frame* allows a clear visualization of the transport dynamics that may not be otherwise apparent.

### 3.4.3. Mapping Method

Rather than integrate the trajectory of each individual fluid particle to solve (34), we exploit the periodicity of the flow field by employing a “mapping method” to rapidly advect large numbers of fluid particles based upon solution of the advection equation (34). This method involves advecting a  $N \times N$  uniform square grid of tracer particles (where  $N$  is typically 200 or greater) that covers the entire computational domain  $(x, y) = [0, 1] \times [0, 1]$  over a single forcing period using a fourth-order explicit Runge-Kutta method. This method was also tested using an implicit Runge-Kutta method and a finer ( $N = 400$ ) grid, and no significant changes to the predicted transport dynamics were observed. Any particles that leave the fluid domain are deemed to lie on the boundary location at which they leave the

domain during the forcing cycle. The updated particle locations are then used to construct the following spline interpolation functions for the  $x$ - and  $y$ -coordinates at the end of a forcing period  $(x_{n+1}, y_{n+1})$  as a function of the coordinates  $(x_n, y_n)$  at the start of the forcing period:

$$x_{n+1} = f_x(x_n, y_n), \quad y_{n+1} = f_y(x_n, y_n). \quad (35)$$

We show that the fluid velocity is net divergence-free over a single forcing period of the aquifer, hence in principle, this method should yield an area-preserving mapping such that the Jacobian  $J = \det(\nabla \mathbf{f})$ ,  $\mathbf{f} = (f_x, f_y)$  is everywhere unity. However, interpolation of particle trajectories via equation (35) above introduces small (typically  $10^{-3}$ ) deviations in the Jacobian from unity. Whilst these deviations can produce spurious behaviour in, e.g. chaotic regions of the flow over very large particle residence times, these effects are relatively minor and do not qualitatively impact the Lagrangian topologies and transport structures in these regions. As expected, large deviations in the Jacobian from unity also occur near the inflow/outflow domain boundaries due to the trapping of particles here; however, these errors are highly localized and do not impact the internal transport structures. Once the mapping functions  $(f_x, f_y)$  are generated, these may be used to rapidly advect very large numbers of particles over many flow periods, facilitating rapid generation of the Poincaré sections used in this study.

### 3.5. Visualization and Analysis of Transport Structures

The transient nature of these complex flow dynamics means they can be difficult to visualize and understand (even in two-dimensional idealizations), and specialized mathematical tools and techniques are required to visualize, classify and quantify the aquifer transport structures and Lagrangian kinematics, which include Poincaré section, Residence Time Distributions (RTDs) and Finite-Time Lyapunov Exponents (FTLEs).

### 3.5.1. Poincaré Sections

In the absence of sources and sinks, steady Darcy flow is typified by open streamlines and an absence of stagnation points (Bear, 1972), leading to slow mixing and limited transport dynamics (Dentz et al., 2016). Conversely, unsteady Darcy flows can break these topological constraints due to transient switching of streamlines (Lester et al., 2009; 2010; Metcalfe et al., 2010a; Trefry et al., 2012), leading to a much richer set of possible transport structures. Particle trajectories in such transient flows can become very complicated, so direct plotting these complex flow trajectories results in a tangle from which it is difficult to discern any coherent structures or Lagrangian topology. A useful tool to aid such visualization for periodic flows is the *Poincaré section* (Aref, 1984; Ottino, 1989), which allows direct visualization of the Lagrangian topology of the flow field and interpretation of the Lagrangian kinematics within each topologically distinct region. A Poincaré section is formed by tracking the number of fluid particles via the advection equation (34), and recording all particle positions at every time period  $P$  of the flow. The computation does not re-inject particles; once a particle exits the domain, it is removed from the simulation. This *stroboscopic map* essentially “filters out” all of the rapid particle motions between tidal forcing periods, leaving only the slow mean particle motion over each forcing period. Henceforth we shall refer to the flow averaged over a forcing period as the *slow flow* of the aquifer. It can be shown that net fluid transport in periodic flows can be almost completely understood solely in terms of this slow flow; hence Poincaré section unveils the hitherto hidden transport structure of the aquifer. The Poincaré section can contain regular, non-chaotic regions which are comprised of coherent 1D particle trajectories that are non-mixing (in the ergodic sense), and distinct chaotic regions which are comprised of a seemingly random particle distributions which are formed as particles undertake chaotic, space-filling

orbits. Chaotic regions are associated with localized strong (exponential) fluid stretching and rapid mixing, whereas the coherent trajectories in regular regions form barriers to transport.

### 3.5.2. Characteristic Transport Structures in Periodically Forced Aquifers

Figure 8 shows the Poincaré sections for the three main types of aquifer transport structures (open, closed, chaotic) found in this study. Below we describe the features and dynamics of these structures, implications for transport, and how they change with the flow control parameters. In this Figure, we have selected cases by only varying the compressibility ratio  $\mathcal{C}$ , but similar transitions are observed by varying the other physical parameters.

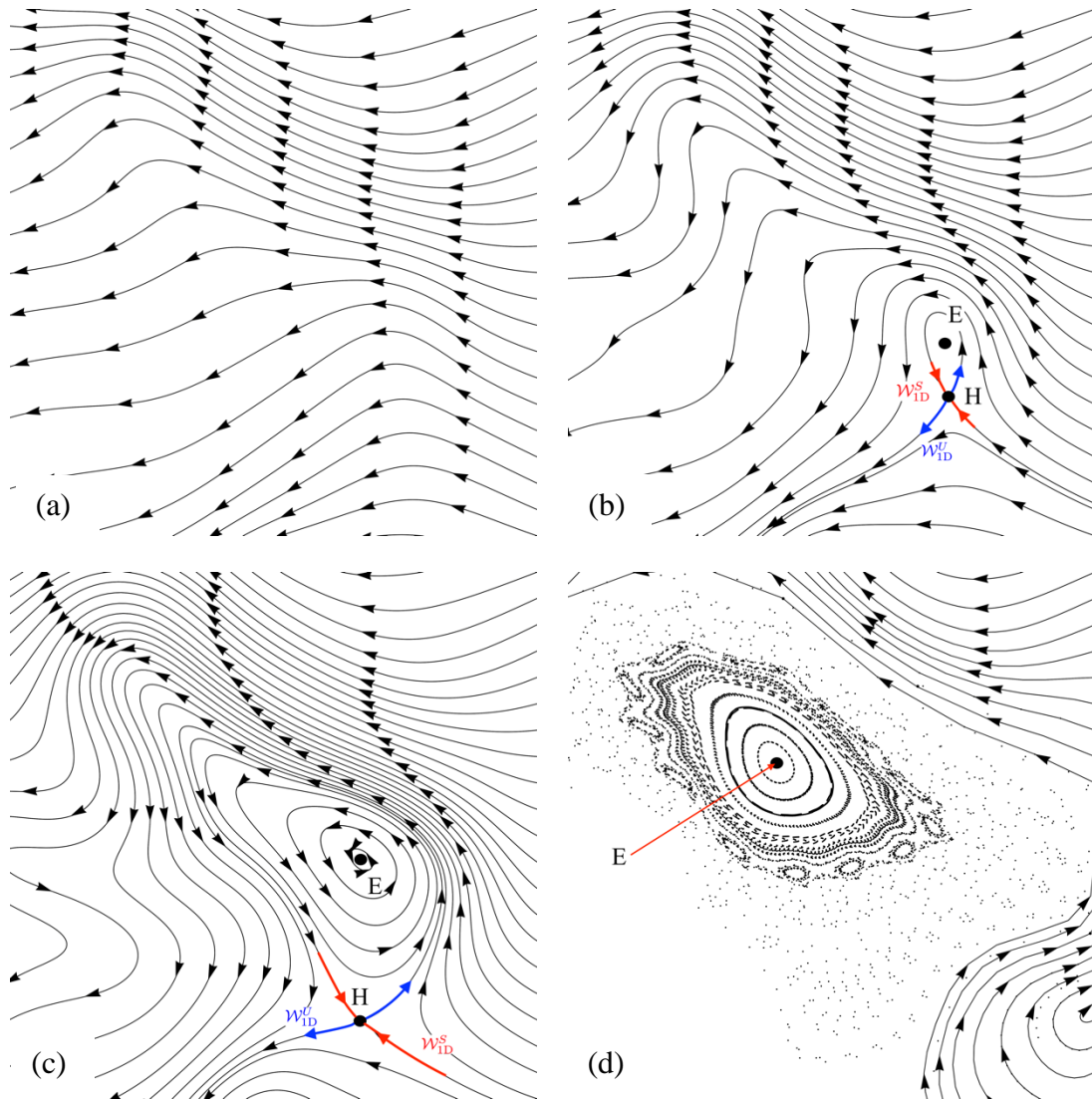


**Figure 8.** Bifurcation of transport structure types with increasing aquifer compressibility  $\mathcal{C}$  with  $\mathcal{T} = 10$ ,  $\mathcal{G} = 100$  in the region  $(x, y) = (0.3, 0.5) \times (0.75, 0.95)$  of the aquifer domain. Examples of (a) open ( $\mathcal{C} = 0.002 < \mathcal{C}_1$ ), (b) closed ( $\mathcal{C}_1 < \mathcal{C} = 0.005 < \mathcal{C}_2$ ), (c) closed ( $\mathcal{C}_1 < \mathcal{C} = 0.1 < \mathcal{C}_2$ ) and (d) chaotic ( $\mathcal{C}_2 < \mathcal{C} = 0.2$ ) transport structures in periodically forced aquifers. Arrows denote propagation of tracer particles along 1D trajectories, scattered points denote incoherent, chaotic motion of tracer particles. Dots denote elliptic (E) or hyperbolic (H) points, blue and red arrows denote unstable and stable manifolds. See text for more details.

### ***Open Transport Structures***

As shown in Figure 8a, for small values of the relative compressibility  $\mathcal{C}$ , the aquifer Poincaré section is comprised only of regular and open (time-averaged) particle trajectories that resemble open streamlines of steady Darcy flow. Although particles undergo cyclical motion as they move through the aquifer, their basic transport structure in the stroboscopic frame consists of ordered and coherent 1D particle paths with no trapped regions or fixed points. Whilst these trajectories are displayed as continuous lines in Figure 8a; typically they would manifest as a series of discrete points in the Poincaré section. Such representation is not possible for the chaotic regions (as regular trajectories do not exist). Hence chaotic regions are displayed using discrete points in Figure 8.

### ***Closed Transport Structures***

Above a critical value (termed  $\mathcal{C}_1$ ) of the relative compressibility  $\mathcal{C}$  (Figure 8b), the aquifer Poincaré section appears to undergo a *topological bifurcation* from open trajectories to particle trajectories that are now closed. This represents a fundamental change in the transport structure as fluid elements can neither enter nor leave this closed region, and so trapped fluid elements have essentially infinite residence times. In addition to these closed

regions, *periodic points* of the flow also arise (where fluid particles return to the same position after one ( $k = 1$ ) or more ( $k > 1$ ) flow periods) which then manifest as fixed ( $k = 1$ ) or periodic ( $k > 1$ ) points in the Poincaré section. As shown in Figure 8, these periodic points may be classified as *elliptic* (E) or *hyperbolic* (H) points, based on their local transport structure. Elliptic points (E) involve a net rotation of the local fluid and are located in the centre of closed flow regions. Hyperbolic points (H) involve a net local saddle flow and are often found at the separatrices between closed and open transport structures. Fluid elements near hyperbolic points undergo exponential fluid deformation over each flow period, with stretching (blue) and contracting (red) particle trajectories shown in Figure 8c that are respectively termed the *unstable* ( $W_{1D}^U$ ) and *stable manifolds* ( $W_{1D}^S$ ) of the flow. These manifolds play a critical role in organizing transport. If these manifolds connect smoothly (Figure 8b, c), then the associated exponential stretching cancels out, and regular particle trajectories result, but more complex transport dynamics arise if they intersect transversely.

### ***Chaotic Transport Structures***

As shown in Figure 8d, further increases in  $\mathcal{C}$  beyond a second critical value  $\mathcal{C}_2$  (where  $\mathcal{C}_2 > \mathcal{C}_1$ ) leads to the breakup of regular, coherent 1D particle trajectories into chaotic, space-filling particle trajectories that manifest as *chaotic regions* in the Poincaré section. From the classical understanding of Hamiltonian chaos (Aref, 1984; Ottino, 1989), these chaotic dynamics arise as the stable and unstable manifolds no longer connect smoothly, resulting in a *chaotic saddle* within the open flow. This region is comprised of a fractal tangle of stable and unstable manifolds that imparts exponential stretching to fluid elements and a fractal distribution of residence times, see Tél et al. (2005); Toroczkai et al. (1998) for details. In contrast, elliptic points (E) represent regular, non-mixing regions in the flow. The Kolmogorov-Arnol'd-Moser (KAM) theorem states that the outermost orbits of these regular

“islands” (termed KAM islands, see Figure 8d) around elliptic points are the least stable and so will break up into chaotic trajectories with further increases in the compressibility parameter  $\mathcal{C}$  beyond  $\mathcal{C}_2$ . Eventually, all of the orbits will become chaotic, but the elliptic point itself will persist.

The three transport structure types (open, closed, chaotic) shown in Figure 8 represent all of the different transport structures observed over the parameter space  $\mathcal{Q} = \mathcal{T} \times \mathcal{G} \times \mathcal{C}$ . In the following section, we then explore how these dynamics impact the global transport properties within the aquifer and the implications for solute transport.

### 3.5.3. Residence Time Distributions (RTDs)

We shall also make extensive use of Residence Time Distributions (RTDs) to characterize transport in the periodically forced aquifers. Although particle trapping is not possible in steady Darcy flow, closed fluid orbits are possible in transient Darcy flow, leading to infinite residence times. These trapped regions are not necessarily chaotic, and they can also be regular with closed streamlines. In this study, we use two different particle injection protocols to generate RTDs and Poincaré sections: (i) inland boundary injection, where tracer particles are released in a flux-weighted manner along the inland boundary ( $x = L$ ), and (ii) distributed injection, where particles are released uniformly over the entire aquifer domain. Distributed injection resolves transport structures that are not accessible to particles released along the inland boundary, whereas inland boundary injection highlights regions of the flow that are not accessible to these particles.

### 3.5.4. Finite-Time Lyapunov Exponents (FTLEs)

We need a quantitative, computable metric that definitively indicates whether chaos exists in the flow or not. The Lyapunov exponent is commonly used in dynamical systems to measure the sensitivity of a system to its initial conditions; it directly characterises the rate of exponential growth of (infinitesimal) material elements (see, e.g., Allshouse and Peacock

(2015)) in both volume-preserving flows and more recently, non-volume-preserving flows (Gonzalez et al., 2016; Pérez-Muñuzuri, 2014; Volk et al., 2014).

The time-dependent groundwater equation (7) describes a non-volume-preserving flow due to the storage term (although it is volume-preserving over a full flow period  $P$ ), and normally corresponds to an *open flow* (Tél et al., 2005) due to the in- and out-flow boundaries typical of hydrogeological models. Here we use the presence of a positive Lyapunov exponent (indicating the presence of exponential fluid stretching) as an indicator of chaotic mixing.

Chaotic advection is characterized by the exponential stretching of fluid material elements where the stretching rate is characterized by the (infinite-time) Lyapunov exponent, defined as

$$\Lambda_{\infty} \equiv \lim_{t \rightarrow \infty} \frac{1}{t} \ln \frac{\delta l(t)}{\delta l(0)}, \quad (36)$$

where  $\delta l(t)$  is the length of an infinitesimal fluid line element advected by the flow. A positive Lyapunov exponent  $\Lambda_{\infty} > 0$  indicates the presence of chaotic advection, and the magnitude of  $\Lambda_{\infty}$  indicates the rate of exponential stretching. For closed flows (whether steady or unsteady), the Lagrangian flow domain can be divided into topologically distinct regions which are either regular (non-chaotic,  $\Lambda_{\infty} = 0$ ) or chaotic ( $\Lambda_{\infty} > 0$ ).

As fluid elements can flow into and out of mixing regions in open flows, it is more useful to characterise deformation of fluid particles in terms of the finite-time Lyapunov exponent (FTLE,  $\Lambda$ ) which quantifies the maximum (i.e. maximum over all possible initial orientations) deformation of an infinitesimal fluid line element. In the limit of infinite residence time, the FTLE of an orbit converges to the infinite-time Lyapunov exponent of the chaotic saddle (which does not flow out of the mixing region), which is also equivalent to the ensemble average of the FTLE over many orbits over finite time.

To formally define and derive the FTLE  $\Lambda$  and the associated fluid deformation gradient tensor  $\mathbf{F}$ , we first introduce the Lagrangian spatial coordinate system  $\mathbf{X}$ , which may be defined in terms of the Eulerian trajectory  $\mathbf{x}(t, t_0; \mathbf{X})$  of a fluid particle at position  $\mathbf{X}$  at time  $t_0$ . The Eulerian trajectory  $\mathbf{x}(t, t_0; \mathbf{X})$  is a solution of the advection equation

$$\frac{\partial \mathbf{x}}{\partial t} = \mathbf{v}(\mathbf{x}, t), \quad \mathbf{x}(t = t_0, t; \mathbf{X}) = \mathbf{X}, \quad (37)$$

and so represents a transformation from Lagrangian ( $\mathbf{X}$ ) to Eulerian ( $\mathbf{x}$ ) spatial coordinates. The FTLE is computed from the fluid deformation gradient tensor  $\mathbf{F}(t, t_0; \mathbf{X})$  which quantifies how the infinitesimal vector  $d\mathbf{x}(t, t_0; \mathbf{X})$  deforms from its reference state  $d\mathbf{x}(t = t_0, t_0; \mathbf{X}) = d\mathbf{X}$ , and so represents the Jacobian tensor associated with a transformation from Lagrangian to Eulerian coordinates:

$$d\mathbf{x} = \mathbf{F} \cdot d\mathbf{X}, \quad (38)$$

and, equivalently,

$$F_{ij} \equiv \frac{\partial x_i}{\partial X_j} \quad \text{where} \quad \mathbf{F} \equiv [F_{ij}]. \quad (39)$$

Following this definition, the deformation gradient tensor  $\mathbf{F}(t, t_0; \mathbf{X})$  evolves with travel time  $t$  along a Lagrangian trajectory (streamline) as

$$\frac{\partial \mathbf{F}}{\partial t} = \nabla \mathbf{v}[\mathbf{x}(t, t_0; \mathbf{X}), t]^\top \cdot \mathbf{F}(t, t_0; \mathbf{X}), \quad \mathbf{F}(t = t_0, t_0; \mathbf{X}) = \mathbf{1}, \quad (40)$$

where the superscript  $\top$  denotes the transpose. We refer to (40) as the *evolution equation* for  $\mathbf{F}$ . Given computation of the deformation gradient tensor via, the FTLE is then defined as

$$\Lambda(t, t_0; \mathbf{X}) \equiv \frac{1}{2(t - t_0)} \ln v_d, \quad (41)$$

where  $v_d$  is the largest eigenvalue of the right Cauchy-Green deformation tensor  $\mathbf{C}$

$$\mathbf{C} = \mathbf{F}(t, t_0; \mathbf{X})^\top \cdot \mathbf{F}(t, t_0; \mathbf{X}). \quad (42)$$

Note that in the limit  $t - t_0 \rightarrow \infty$ , the FTLE converges to the (infinite-time) Lyapunov exponent  $\Lambda_\infty$ , and due to ergodicity in chaotic regions, the ensemble average  $\langle \Lambda(t, t_0; \mathbf{X}) \rangle$

(where the average is performed over many starting positions  $\mathbf{X}$ ) also converges to  $\Lambda_\infty$ . In this way, the infinite-time Lyapunov exponent in for chaotic regions in open flows may be accurately estimated even if the typical orbit residence time is short.

For incompressible flows,  $\nabla \cdot \mathbf{v} = 0$ , (40) yields the result  $\det(\mathbf{F}) = 1$ , i.e. the volumes of fluid elements are preserved under the flow. However the groundwater velocity  $\mathbf{v} = \mathbf{q}/\varphi$  is not divergence-free, so care needs to be taken in computing the fluid deformation gradient tensor  $\mathbf{F}(t, t_0; \mathbf{X})$  and the associated FTLEs  $\Lambda(t, t_0; \mathbf{X})$  in the linear groundwater flow (7) due to Spatio-temporal variability of the porosity  $\varphi(\mathbf{x}, t)$ . Conservation of fluid mass under the linear groundwater flow is captured explicitly by the continuity equation (4) and tracking of fluid “particles” must be performed with respect to the groundwater velocity. Note that whilst the variable nature of  $\varphi$  renders neither  $\mathbf{v}$  nor  $\mathbf{q}$  divergence-free, it is important that constraints imposed by (4) on particle advection kinematics and fluid deformation are enforced so to eliminate spurious transport and mixing behaviours (see Subsection 3.3.3).

From the evolution equation (40), we find

$$\det \mathbf{F}(t, t_0; \mathbf{X}) = \exp \left[ \int_{t_0}^t \nabla \cdot \mathbf{v}(\mathbf{x}(t', t_0; \mathbf{X}), t') dt' \right], \quad (43)$$

where the integral is also applied in fixed Lagrangian position  $\mathbf{X}$ . We derive an explicit expression for the divergence  $\nabla \cdot \mathbf{v}$  as follows. We define the fluid material derivative as

$$\frac{D_f}{Dt} \equiv \frac{\partial}{\partial t} + \mathbf{v} \cdot \nabla, \quad (44)$$

and so from equation (4),

$$\nabla \cdot \mathbf{v} = -\frac{D_f}{Dt} \ln \varphi, \quad (45)$$

hence

$$\det \mathbf{F}(t, t_0; \mathbf{X}) = \exp \left[ \int_{t_0}^t -\frac{D_f}{Dt'} \ln \varphi \, dt' \right] = \frac{\varphi(\mathbf{X}, t_0)}{\varphi(\mathbf{x}(t, t_0; \mathbf{X}), t)}. \quad (46)$$

The impact of mass conservation (4) is that the volume of a moving fluid element scales inversely with the local porosity  $\varphi$ . While this imposes temporal fluctuations in  $\det \mathbf{F}$ , these are transient and bounded. Hence mass is conserved over arbitrarily long times. As such (46) serves as a consistency check during particle tracking and computation of FTLEs.

### 3.6. Chapter Summary

This chapter introduces a conventional model 2D Darcian system representing a heterogeneous, tidally forced confined aquifer that is used as a basis for a Lagrangian analysis of the flow regime. Key dimensionless parameter groups are introduced, which include the attenuation of the tidal fluctuation into the aquifer ( $\mathcal{T}$ ), the strength of tidal forcing relative to that of the regional flow ( $\mathcal{G}$ ), and the relative compressibility of the aquifer ( $\mathcal{C}$ ), as well as the statistical parameters of the random hydraulic conductivity field  $(K_{\text{eff}}, \sigma_{\log K}^2, \lambda)$ .

The tidal flow problem is solved numerically, and the basic solution properties are explored, focusing on the flux and velocity distributions. The techniques and tools to visualize Lagrangian transport structures are also introduced, which include Poincaré sections, Residence Time Distributions (RTDs) and Finite-Time Lyapunov Exponents (FTLEs). In the next chapter, a survey of Lagrangian and chaotic phenomena arising in the model tidal system is presented.

## Chapter Four

### 4. Complex Transport in Transiently Forced Aquifers

In this chapter, we study the complex transport dynamics that arise in transiently forced aquifers via the numerical model, particle tracking, visualization and analysis methods described in Chapter 3. Sections 4.1 - 4.4 provides a brief description of the physical characteristics in transiently forced aquifers, including the mechanisms that generate complex transport. Specifically, these sections also demonstrate how the interplay between conductivity and compressibility of the aquifer can induce flow reversal, and why compressibility of the porous medium is a necessary condition for chaotic particle trajectories. Section 4.5 considers the Lagrangian kinematics of a tidally forced flow in a heterogeneous aquifer for a single set of governing parameters. Finally, Section 4.6 uses a series of visualization and analysis tools to classify and understand the transport structures of this flow.

#### 4.1. Basic Hydraulic Characteristics

Early analytical results for tidal influences in one-dimensional aquifers with uniform and homogeneous conductivity fields were derived for semi-infinite domains by Jacob (1950) and were subsequently extended to finite (Townley, 1995), layered (Li & Jiao, 2002) and composite (Trefry, 1999) domains. Analytical results were also obtained in two dimensions for uniform (Li et al., 2000) and stochastic (Trefry et al., 2011) aquifer property distributions. Many other analytical results for tidal groundwater systems have been reported.

A key feature of the tidal solutions is a finite propagation speed of pressure fluctuations from the tidal boundary to the aquifer interior, so that induced oscillations measured at locations inside the aquifer domain are lagged (out of phase) and attenuated (reduced in amplitude) with respect to the boundary forcing condition. For a one-dimensional, semi-infinite homogeneous aquifer, the phase lag  $\Delta\tau$  and attenuation  $\alpha$  are related to the forcing

frequency  $\omega$ , aquifer diffusivity  $D = K/S$  and distance  $x$  from the tidal boundary as (Ferris, 1952; Jacob, 1950)

$$\Delta\tau = x/\sqrt{2\omega D}, \quad \alpha = \exp(-x\sqrt{\omega/2D}). \quad (47)$$

The dissipative nature of the periodic head equation (20) provides an exponential decay of oscillation amplitude with distance from the forcing boundary and phase lag increasing linearly with distance, with the attenuation greatest for high  $\omega$  and least for low  $\omega$ .

#### 4.2. Flux Ellipses and Flow Reversal

As shown by Kacimov et al. (1999) and Smith et al. (2005), time-periodic groundwater forcing can cause elliptical velocity orbits at each point in the aquifer domain. More precisely, the family of possible velocity orbits includes ellipses, circles, lines and points, depending on degeneracies in the semi-axes and component phases of the underlying flux ellipses. Returning to the present tidal problem, the combination of a time varying boundary condition with spatial heterogeneity of  $\kappa$  produces elliptical Darcy flux orbits. The induced Darcy flux  $\mathbf{q}(\mathbf{x}, t) = (q_x, q_y)$  at a location  $\mathbf{x} = (x, y)$  and time  $t$  can be decomposed into steady and periodic components as

$$\mathbf{q}(\mathbf{x}, t) = \mathbf{q}_s(\mathbf{x}) + \mathbf{q}_p(\mathbf{x}, t) \equiv \mathbf{q}_s(\mathbf{x}) + \mathbf{q}_p(\mathbf{x})e^{i\omega t}, \quad (48)$$

where  $\mathbf{q}_s = -K\nabla h_s$ ,  $\mathbf{q}_p = -K\nabla h_p$ . For any location  $\mathbf{x}$  in the flow domain, the steady flux  $\mathbf{q}_s(\mathbf{x})$  fixes the location of the centre of the flux ellipse shown in Figure 9, whereas the periodic flux  $\mathbf{q}_p(\mathbf{x}, t)$  governs the orientation, eccentricity and magnitude of the flux ellipse that is swept out parametrically with  $t$  over a flow period. The sign of  $\mathbf{q}_p$  dictates whether the flux ellipse is traced out clockwise or anti-clockwise in time. For more complex multi-modal tidal forcing  $g(t)$ , the orbit traced out by  $\mathbf{q}$  may be more complex than a simple ellipse, but the qualitative aspects of the system are conserved.

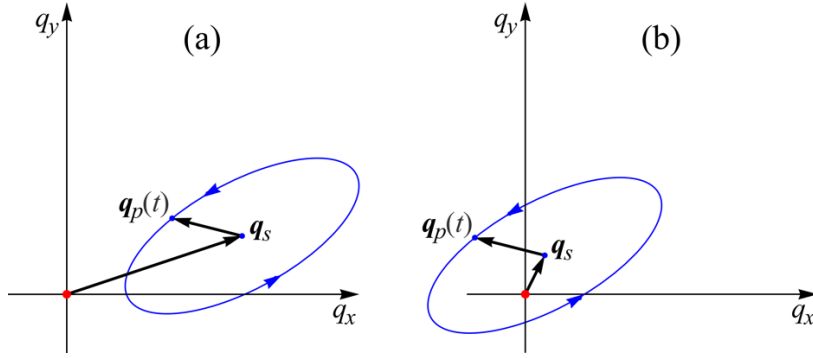


**Figure 9.** Schematic of flux ellipses drawn in blue - (a) regular (excluding the origin), and (b) canonical (containing the origin). Arrows on the ellipses indicate the direction of increasing time  $t$ . Both flux components of the canonical ellipse change sign at times during the oscillation period.

Under the condition that the magnitude of the periodic flux is greater than that of the steady flux at a given point  $\mathbf{x}$ , i.e.  $\|\mathbf{q}_p(\mathbf{x})\| > \|\mathbf{q}_s(\mathbf{x})\|$ , then *flow reversal* occurs at some time in the flow cycle, i.e. the total flux  $\mathbf{q}$  is in the opposite direction to the steady flux  $\mathbf{q}_s$ , and the flux ellipse over the entire flow cycle contains the origin  $\mathbf{q} = \mathbf{0}$ . Flux ellipses that contain the origin (and hence admit flow reversal) will henceforth be referred to as *canonical*. In Section 4.3, we show that periodic flow reversal occurs due to the interplay between conductivity variations and compressibility of the aquifer.

As shown in Section 4.4, for incompressible aquifers ( $S = 0$ ) the periodic flux vector  $\mathbf{q}_p(\mathbf{x}, t)$  aligns with the steady flux vector  $\mathbf{q}_s(\mathbf{x})$  and the sign and magnitude of  $\mathbf{q}_p$  simply oscillates over a tidal forcing cycle. Consequently, the flux ellipses in the incompressible limit have zero width (or infinite eccentricity). This leads to fluid particle trajectories that follow simple, smooth streamlines (although particles move backwards and forwards as they propagate along these streamlines), leading to regular, non-chaotic fluid motion. Accordingly, we denote any flux ellipse with an eccentricity greater than 100 as a *trivial* ellipse as it will not contribute significantly to complex fluid motion.

### 4.3. Connection of Flow Reversal to Matrix Conductivity and Poroelasticity

The effect of the tidal boundary is to generate significant flow reversals that stimulate the Lagrangian phenomena of interest. Vorticity provides a measure of flow reversal and can be related to key physical processes in the poroelastic system. Consider the vorticity  $\boldsymbol{\omega}$  of our 2D groundwater flow, defined by  $\boldsymbol{\omega} \equiv \nabla \times \mathbf{v} = \nabla \times (\mathbf{q}/\varphi)$ . By a standard vector identity, the curl of a product of a scalar and a vector is, in the notation of our system,

$$\nabla \times \left( \frac{\mathbf{q}}{\varphi} \right) = \nabla \left( \frac{1}{\varphi} \right) \times \mathbf{q} + \left( \frac{1}{\varphi} \right) \nabla \times \mathbf{q} = \varphi^{-2} (\nabla \varphi \times \mathbf{q}) + \varphi^{-1} (\nabla \times \mathbf{q}). \quad (49)$$

Noting that  $\nabla \varphi = S \nabla h$  (see equation (6)) and that the curl of the gradient of a scalar is zero results in the vorticity relation

$$\boldsymbol{\omega} = \frac{\nabla h \times \nabla \kappa}{\varphi}, \quad (50)$$

expressed in terms of the conductivity and porosity of the matrix. Using the expression for the linear poroelasticity (6) and defining  $\hat{h}(\mathbf{x}, t) \equiv (h(\mathbf{x}, t) - h_{\text{ref}})/g_p$  as the non-dimensional local forcing, equation (50) becomes

$$\boldsymbol{\omega} = \frac{\boldsymbol{\omega}_\kappa}{1 + \mathcal{C} \hat{h}} \quad (51)$$

with

$$\boldsymbol{\omega}_\kappa = \frac{\nabla h \times \nabla \kappa}{\varphi_{\text{ref}}}, \quad (52)$$

the vorticity from shear flows generated solely by conductivity variations.

Equation (51) implies that flow reversal occurs due to conductivity variations and poroelasticity (if the storativity varies in space, (50) includes an additional term  $\kappa h (\nabla h \times \nabla S)$  that could separately generate vorticity due to non-trivial variation of the storage field). The magnitude of  $\boldsymbol{\omega}_\kappa$  is controlled by the conductivity variance  $\sigma_{\log \kappa}^2$ . However, as discussed in Section 4.4, it is the trajectory symmetry breaking due to poroelasticity that produces interesting Lagrangian transport structure. Flow reversal from non-trivial conductivity

variation and symmetry breaking from poroelasticity are the two crucial physical ingredients in the creation of the transport dynamics we observe.

#### 4.4. Integrability of Particle Trajectories for Incompressible Media

To show that fluid particle trajectories are *integrable* for incompressible media (i.e. they cannot exhibit chaotic dynamics), we consider the linear groundwater equation (7) in the limit  $S = 0$  in terms of the steady  $h_s(\mathbf{x})$  and periodic  $h_p(\mathbf{x}, t)$  head solutions

$$\nabla \cdot (K(\mathbf{x})\nabla[h_s(\mathbf{x}) + h_p(\mathbf{x}, t)]) = 0, \quad (53)$$

subject to the fixed head boundary conditions  $h|_{x=L} = g_L$ ,  $h|_{x=0} = g(t)$ , the latter of which may be decomposed into steady and zero-mean fluctuating components as  $g(t) = \bar{g} + g'(t)$ . Due to linearity, (53) is satisfied individually by the steady and periodic solutions, which may be expressed as

$$h_s(\mathbf{x}) = g_L + (\bar{g} - g_L)f(\mathbf{x}), \quad (54)$$

$$h_p(\mathbf{x}, t) = g'(t)f(\mathbf{x}), \quad (55)$$

where  $f(\mathbf{x})$  is the solution to (53) subject to the fixed head boundary conditions  $h|_{x=L} = 1$ ,  $h|_{x=0} = 0$ . As the porosity  $\varphi = \varphi_{\text{ref}}$  is constant in the limit  $S = 0$ , from (23) both the fluid velocity and Darcy flux are separable in space and time as

$$\mathbf{v}(\mathbf{x}, t) = \frac{1}{\varphi_{\text{ref}}} \mathbf{q}(\mathbf{x}, t) = \frac{1}{\varphi_{\text{ref}}} K(\mathbf{x})\nabla h(\mathbf{x}, t), \quad (56)$$

$$= \mathbf{v}_0(\mathbf{x})G(t), \quad (57)$$

where  $\mathbf{v}_0(\mathbf{x}) = K(\mathbf{x})\nabla f(\mathbf{x})$ ,  $G(t) = \bar{g} - g_L + g'(t)$ . The evolution of the position of fluid particles is then given by the steady 2D advection equation

$$\frac{d\mathbf{x}}{d\tau} = \mathbf{v}_0(\mathbf{x}), \quad (58)$$

where  $d\tau = G(t)dt$ . Following the discussion in Section 2.2, because (58) is a steady 2D vector field; it cannot admit chaotic behaviour (Aref et al., 2017). Note that as the porosity

$\varphi_{\text{ref}}$  is constant, the fluid velocity may be described in terms of the streamfunction  $\psi_0$  as  $\mathbf{v}_0 = \nabla \times \psi_0(\mathbf{x})\mathbf{e}_z$ . Hence for incompressible media ( $S = 0$ ), fluid particle trajectories are confined to fixed one-dimensional “streamlines” which correspond to level sets of the streamfunction  $\psi_0$ , even though the flow is unsteady. Evolution along these “streamlines” is not monotone but may oscillate according to the forcing  $G(t)$ . This is evident in Figure 11 where flow paths calculated from a compressible flow solution ( $S > 0$ ) are compared with flow paths calculated for incompressible flow ( $S = 0$ ). The former paths display flow reversal loops and braiding dynamics, while the latter resemble laminar streamlines, inherently excluding chaos. Compressibility of the porous medium ( $S > 0$ ) is a necessary condition for the attainment of chaotic dynamics.

#### 4.5. Tidal Flow in Heterogeneous Domains

In this section, we focus on the Lagrangian kinematics of the tidally forced groundwater system described in Chapter 3 (Section 3.3) with parameter set  $(\mathcal{T}, \mathcal{G}, \mathcal{C}) = (10\pi, 10, 0.5)$  which corresponds to a highly compressible and diffusive aquifer system subject to a diurnal tidal signal. In Chapter 6 (Section 6.2), we place this parameter set in context with respect to known parameter values from particular field studies. In Chapter 5, we shall explore the distribution of Lagrangian kinematics over the tidal flow parameter space  $\mathcal{Q} = \mathcal{T} \times \mathcal{G} \times \mathcal{C}$ . The hydraulic conductivity field  $\kappa$  used is a single  $(164 \times 164)$  realization generated according to the algorithm of Ruan and McLaughlin (1998) corresponding to an aquifer of moderate heterogeneity ( $\lambda = 0.049$ ,  $\sigma_{\log K}^2 = 2$ ). This field yields reversal number  $\mathcal{G} \sigma_{\log K}^2 = 20$  and heterogeneity characters  $(\mathcal{H}_t, \mathcal{H}_x) = (4.9, 13.6)$ , i.e. the system is near temporal resonance ( $\mathcal{H}_t = 1$ ) and has  $\mathcal{O}(10)$  correlation scales within the tidally active zone. The  $\kappa$  field is shown in Figure 10, along with the associated steady and periodic head components and evolution of the porosity profile over a forcing cycle. These plots clearly

show a mean exponential decay in oscillation amplitude with distance from the tidal boundary for both heterogeneous and homogeneous aquifers, along with a phase lag that increases with distance. Fluctuations in the heterogeneous head solutions away from the homogeneous state have spatial scales that are somewhat larger than  $\lambda$  (Trefry et al., 2011). As shown in Figure 10d, the normalized porosity ( $\varphi/\varphi_{\text{ref}}$ ) oscillates around unity (with amplitude  $\mathcal{C}$ ) synchronously with the tidal condition at the left boundary, and tends to a value determined by the upstream boundary head  $\varphi/\varphi_{\text{ref}} \rightarrow 1 + JLS/\varphi_{\text{ref}} = 1 + \mathcal{C}/\mathcal{G}$  as  $x \rightarrow 1$ .

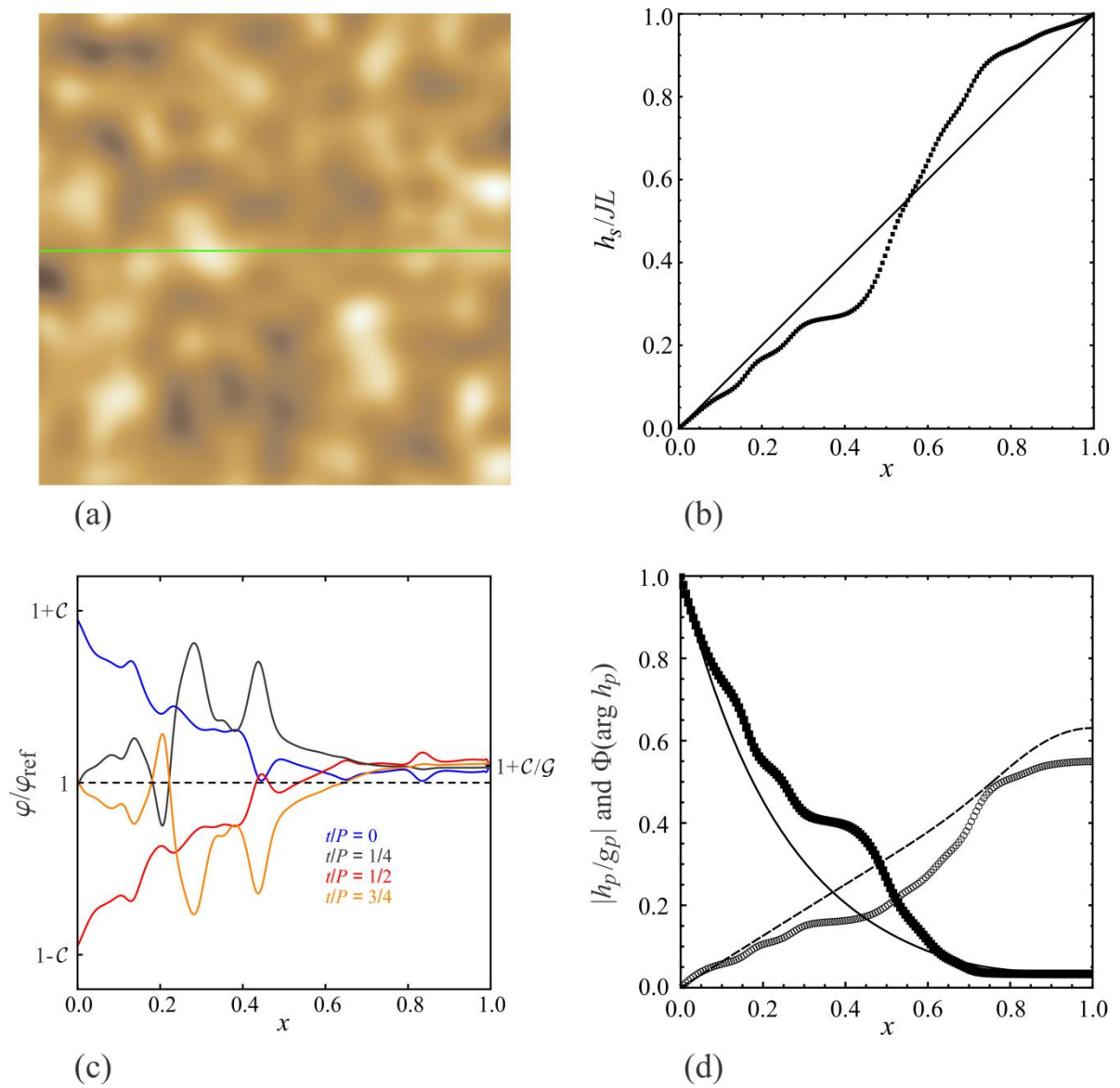


**Figure 10.** (a) Density map of log hydraulic conductivity  $\kappa$  where lower (higher) values are darker (lighter). (b) Profile of the steady head  $h_s$  for the heterogeneous simulation (squares)

and reference homogeneous solution (line) along the green line  $y = 0.5$  shown in (a). (c) Variation of the normalized total porosity  $\varphi/\varphi_{\text{ref}}$  along  $y = 0.5$  over the tidal cycle. (d) Same as for (b) but showing the periodic head solution  $h_p$  (square) and phase lag  $\text{arg}h_p$  (circles) for the heterogeneous simulation with the reference homogeneous solutions shown as curves.

Of primary interest are the flow paths shown in Figure 11 which are calculated from a set of equally spaced starting locations near the inland boundary  $x = 1$ ; the elapsed number of flow periods is annotated along each flow path. As expected, the spatial heterogeneity of  $\kappa$  causes significant deflections of flow paths around low conductivity zones, and travel speeds also vary greatly along and between flow paths. In addition, as the paths move closer to the tidal boundary, they encounter flow reversal cells, causing some paths to undergo many sweeps back and forth (flow reversals) with relatively slow net progress toward the tidal boundary. Such flow reversal can result in *braiding* of particle trajectories, as clearly evidenced by the different vertical ordering of the trajectories at the left and right boundaries in Figure 11 (bottom left). Note that such braiding and transient “crossing” of streamlines can be a signature of chaotic mixing; however, such behaviour is not possible in steady 2D or 3D Darcy flows.

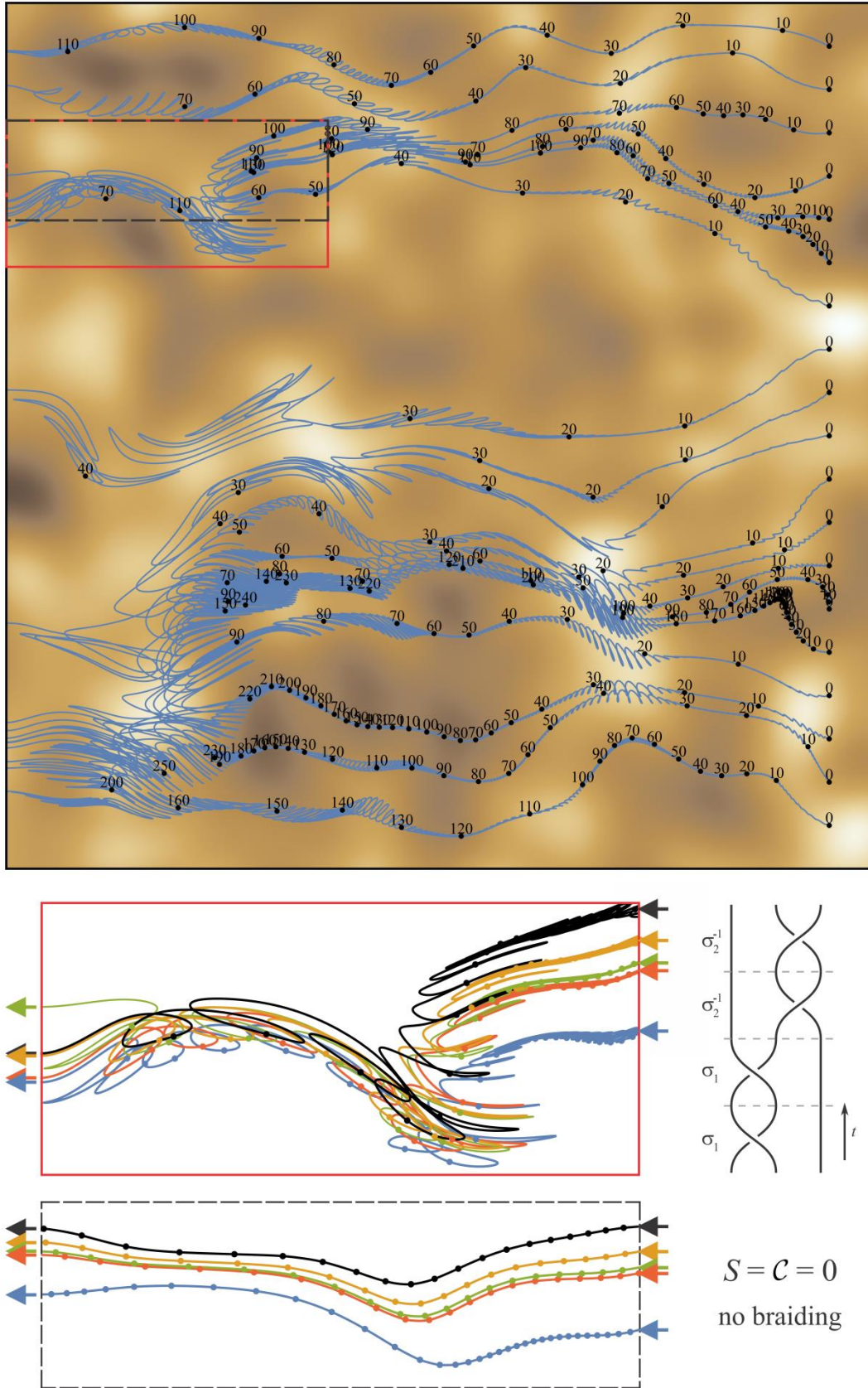


**Figure 11.** (top) Flow paths, with the number of flow periods shown along each trajectory. (middle left) Detail of the red box with flow paths coloured and dotted every period. Note the

change in vertical order of the flow paths from entry to exit (braiding). (middle right) Schematic of generic braiding of fluid trajectories with time  $t$  (adapted from Finn and Thiffeault (2011)). (bottom) Corresponding flow paths for the zero-compression case – no braiding is possible (see Section 4.4).

Recent studies (Finn & Thiffeault, 2011; Thiffeault, 2010a) have shown that symbolic representation of the braiding motions shown in Figure 11 (lower right) allow the complexity of the braiding motions to be calculated in terms of the so-called *topological entropy* which provides an accurate lower bound for the Lyapunov exponent that characterises chaotic mixing. Trivial braids, such as two sequential crossings that cancel each other out have zero complexity, indicating non-chaotic kinematics. Although not evaluated here, the orbits shown in Figure 11 (bottom left) indicate non-trivial braids with positive complexity and hence chaotic dynamics. In Subsection 4.6.5, we calculate a different quantitative measure of chaos in terms of finite-time Lyapunov exponents.

## 4.6. Mechanisms and Measures of Transport Complexity

### 4.6.1. Flow Reversal Ellipses

As shown above, flow paths for the heterogeneous tidal problem can become entwined and generally present a complicated picture that may obscure the underlying dynamical structures. In this section, we seek methods to elucidate and quantify the structure of the tidal discharge map. We do this in the Lagrangian frame in order to uncover the Lagrangian transport structure of the flow.

Figure 12 shows that almost all of the tidally active zone undergoes flow reversal. The distribution of flow reversal ellipses in the model aquifer domain is dense near the tidal boundary, and these ellipses appear to extend into the aquifer domain with mean distance similar to  $x_{\text{taz}}$ . The distribution of ellipse rotation (clockwise/anti-clockwise) is also

heterogeneous and is spatially correlated with a somewhat larger integral scale than the underlying hydraulic conductivity field. Whilst flow reversal is directly involved in the generation of complex Lagrangian kinematics (as discussed in Subsection 4.6.4), we find little correlation between the distribution of flow reversal ellipses and their orientation and the Lagrangian topology of the flow which is discussed throughout this section. Lack of direct correlation between Eulerian flow measures (e.g. flow reversal) and Lagrangian kinematics and topology is characteristic of chaotic flows and highlights the necessity of visualizing transport in the Lagrangian frame.

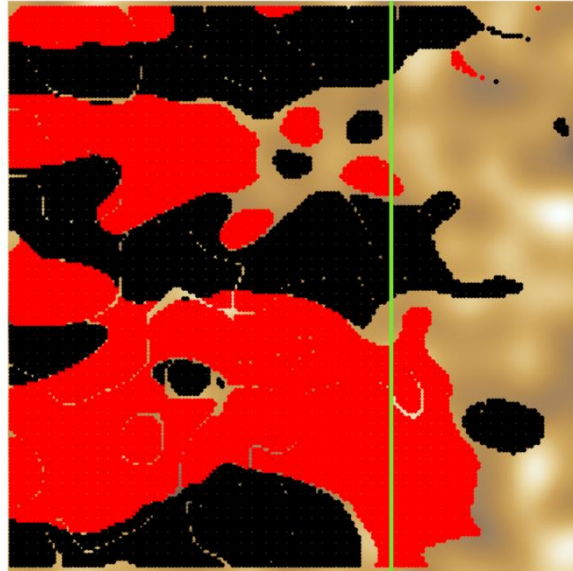


**Figure 12.** Location of clockwise (black) and anticlockwise (red) canonical flux ellipses (red/black points) evaluated over the aquifer domain. The edge of the canonical flux ellipse distribution approximates the extent of the tidally active zone shown by the green line drawn at  $x = x_{\text{taz}}$ .

#### 4.6.2. Residence Time Distributions (RTDs)

Transport characteristics of coastal aquifers are primarily quantified in terms of the residence time distributions (RTDs) associated with transport of fluid particles through the

aquifer. Figure 13a shows the RTD (denoted  $\tau$ ) for  $10^4$  fluid particles seeded in a flux-weighted distribution along the inland boundary ( $x = 1$ ) for both a steady discharge flow (blue curve) without tidal forcing (i.e.  $\mathcal{G} = 0$ ), and for the case of a steady discharge flow coupled with transient tidal force (black dots and grey lines),  $\mathcal{G} > 0$ . Figure 13b shows a map of the RTD for the transient tidal flow plotted as a function of initial position for a  $1000 \times 1000$  grid of fluid particles seeded across (centre) the aquifer domain  $\mathcal{D}$  and (right) a square inset region covering the largest mixing region of the flow.

The steady regional flow RTD shown in Figure 13a (blue curve) is continuous and consists of well-defined peaks and troughs that are controlled solely by the heterogeneity of the conductivity field. Conversely, the tidal RTD displays some regions with well-defined, smooth, continuous peaks and troughs, but also other zones of apparently stochastic nature where residence times vary abruptly. Highly resolved plots (not shown) of these residence times indicate they are indeed smooth but at very small scales. These stochastic zones are interpreted as intervals where neighbouring flow paths are braided (entwined), as demonstrated in Figure 11 (top), so that adjacent discharges at the tidal boundary may originate from widely separated flow paths with very different travel times.

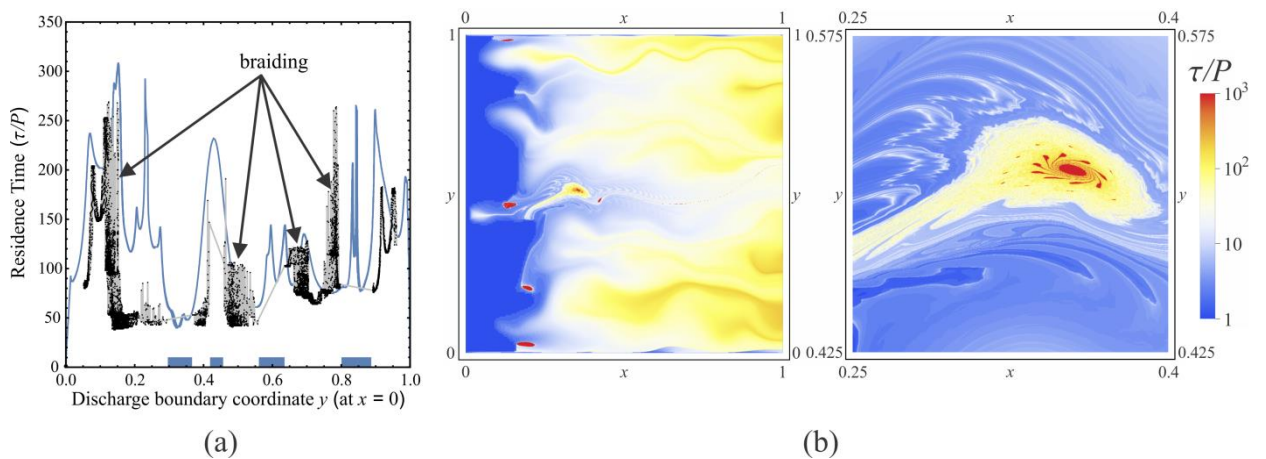


**Figure 13.** (a) The blue curve shows the RTD for the steady regional discharge flow, and the black dots indicate residence times for the tidally forced flow. Blue bars indicate zones excluded to regional discharge. Several zones of braided tidal discharge are noted. (b) Maps

of RTD for the transient tidal flow plotted in terms of initial position for a  $1000 \times 1000$  grid of particles seeded over (left) the entire tidal domain and (right) a square region covering the structure centred at  $(x, y) \approx (0.35, 0.51)$ . Particle tracking is performed up to  $t/P = 10^3$ , hence red points have residence time  $\tau > 10^3 P$ .

The tidal RTD appears to be discontinuous at the macroscale in that there are large gaps in the discharge boundary position shown in Figure 13a. These are indicated by straight grey lines between black points in the RTD trace and the blue bars along the horizontal axis. The RTD gaps correspond to "exclusion zones" along the tidal boundary ( $x = 0$ ), through which inland flow originating at the inland boundary never exits. Rather, the inland flow discharges in the gaps between these exclusion zones. This unexpected result means that the combination of tidal forcing with aquifer heterogeneity can lead to significant intervals of the tidal boundary being inaccessible to the discharge of regional flow. Below we offer a tentative explanation for the existence of exclusion zones.

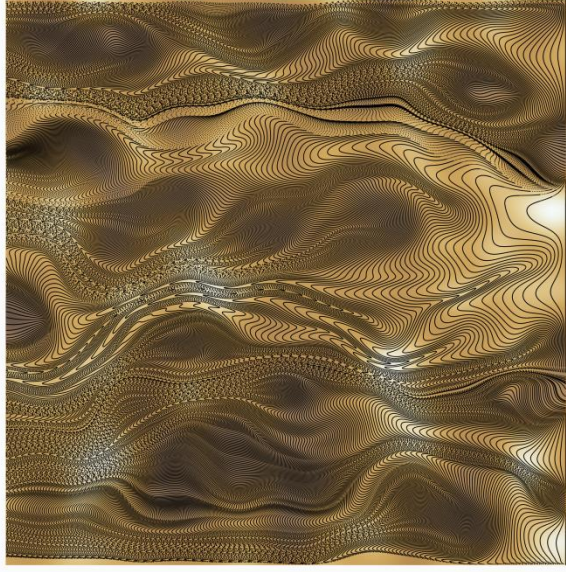
Note that the RTD for particles seeded along the inland boundary ( $x = 1$ ) for the transient tidal flow (or steady regional flow) do not exhibit diverging residence times (even when much higher resolution of the RTD distribution is computed than that shown in Figure 13a), despite observations of such divergent residence times (red points) as shown in Figure 13b. This is due to the fact that particles which are seeded at the inland boundary cannot enter these trapping regions for reasons which are explained in Subsection 4.6.3. Conversely, Figure 13b shows that when particles are seeded over the entire flow domain, there are several distinct regions with very long RTDs but which are impervious to particles seeded at the inland boundary. Detail of the largest long RTD "island" indicates a complex, fractal-like structure; the nature and origin of this structure are explained in Subsection 4.6.3. The blue region ( $\tau \leq P$ ) indicates the set of trajectories that exit the domain within one flow period;

we denote this region the *tidal emptying region* and the rightmost boundary of this region as the *tidal emptying boundary*.

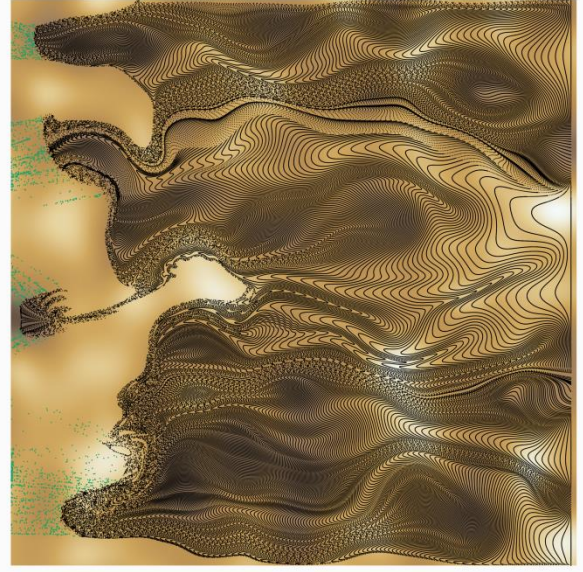
#### 4.6.3. Poincaré Sections

The RTD distributions in the previous section indicate the presence of complex transport and mixing dynamics within tidally forced aquifers. As indicated by Figure 11, plotting these complex flow trajectories results in a tangle from which it is difficult to discern any coherent structures or Lagrangian topology. To circumvent this problem, we use the Poincaré section, which described in Chapter 3 to resolve these transport structures.

Figure 14 shows two Poincaré sections generated by releasing over 3,000 particles along a vertical line near the inland boundary ( $x = 1$ ) for (a) the steady regional flow and (b) the full (periodic) tidal flow. In each section, particle locations are recorded and displayed using a Poincaré period  $\mathcal{P} = P$ . The structure of the Poincaré section for the steady flow arises solely from heterogeneity of the aquifer, where focussing of particles into (away from) high (low) permeability regions is apparent (see, e.g., Trefry et al. (2003)), along with differences in advective speed through these high/low permeability regions. Whilst the Poincaré section of the tidal flow is almost identical to that of the steady flow in the vicinity of the inland boundary; significant deviations occur near the tidal boundary. Most apparent is a large region (the *tidal emptying region*, where  $\tau < P$ ) near the tidal boundary which is devoid of fluid tracer particles seeded from the inland boundary. Within this tidal emptying region there may be subregions where tracer particles may be (i) discharged in times less than a flow period (a *discharge region*), (ii) enter from outside the aquifer domain ( $x < 0$ ) (an *entry region*), or (iii) are trapped within a subregion indefinitely (a *trapped region*).



(a) Steady flow solution



(b) Full tidal solution

**Figure 14.** Poincaré sections formed from locations of points (black) advecting through the flow fields. Sections are assembled with time intervals  $\mathcal{P} = P$  for both steady (a) and tidal flow (b) cases. The tidal section also shows discharging points in green (near the left boundary), calculated with  $\mathcal{P} = P/10$  from the particle locations at the last completed tidal period before discharge.

Discharge regions are illustrated by the green points in Figure 14b, which indicate the locations of particles that originated from the inland boundary ( $x = 1$ ) within the tidal region at temporal increments of  $t = P/10$ . As shown, discharge along the tidal boundary ( $x = 0$ ) coincides with gaps in the exclusion zones shown in the RTD plot in Figure 13a. This indicates that the exclusion zones along the tidal boundary are associated with the inflow of particles from the oceanic side of the tidal boundary ( $x < 0$ , not modelled). Although the dynamics in these discharge regions appear to be quite rich (as indicated by the green points in Figure 15), we do not consider them further in this study. Exclusion zones correspond to

the blue bars and gaps in the outflow RTD has shown in Figure 13a, and which themselves correspond to inflow regions into the tidal emptying region.

When compared with the residence time distribution plot in Figure 13b, the tidal region appears to be mainly (but not completely) comprised of particle initial positions with residence times that are either less than one period ( $\tau < P$ ) or have diverging residence time ( $\tau \rightarrow \infty$ ). The short residence time regions indicate discharge or entry regions, whilst the diverging residence times indicate trapped regions within the tidal flow system.

#### **4.6.4. Elucidation of Lagrangian Kinematics and Lagrangian Topology**

Whilst these observations give a qualitative picture of the complex transport and mixing dynamics in the tidal region; many features are hidden due to selectivity from seeding particles only at the inland boundary ( $x = 1$ ). To fully resolve the Lagrangian kinematics of the flow, we perform a closer inspection of the Poincaré section by seeding fluid particles throughout the tidal region and resolving Lagrangian coherent structures such as periodic points and invariant manifolds. Here we see for the first time, how fluid transport due to tidal flows in heterogeneous aquifers is organized and the associated Lagrangian transport structure. These are described in detail as follows.

##### ***Periodic Points and Manifolds***

The result of this detailed Lagrangian analysis is shown in Figure 15, which contains transport structure annotations added to Figure 14b. The significance of these annotations is discussed in the succeeding subsections. In Figure 15, strikingly, the exclusion zones penetrate far into the aquifer, each terminating at a *hyperbolic point* (H) at an intersection of associated stable and unstable manifolds. Unstable manifolds (departing blue curves) define the exclusion zone boundaries, while stable manifolds (arriving red curves) act as separatrices for slow fluid trajectories. It is important to remember that whilst structures in the Poincaré

section govern the *slow flow* of particles, complete trajectories of fluid particles include the fast oscillatory motion (as shown in Figure 11) between periods.

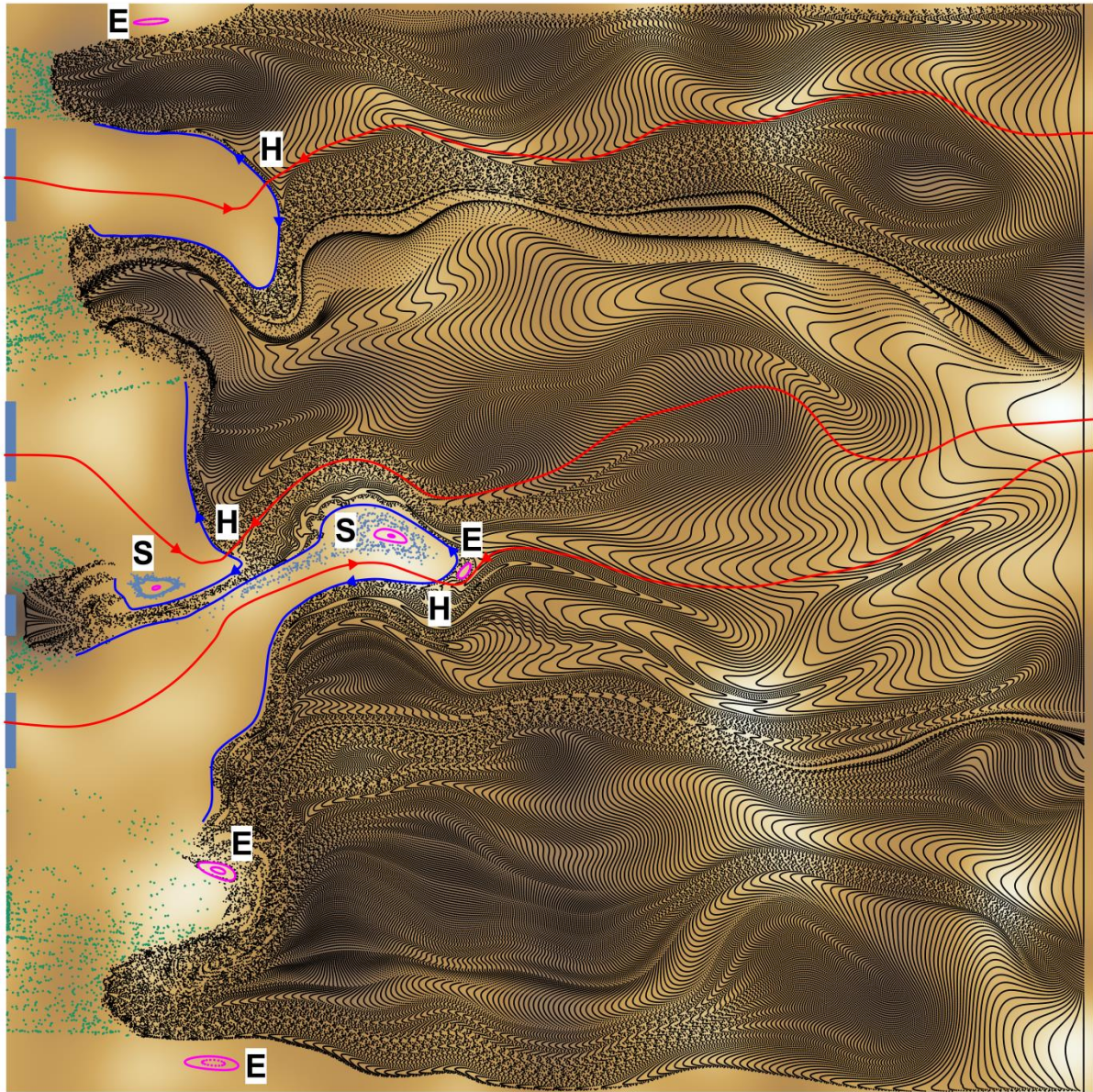


**Figure 15.** Annotated Poincaré section of the tidally forced aquifer showing hyperbolic (H) and elliptic (E) points, stochastic layers (S), stable (red lines) and unstable (blue lines) manifolds, KAM islands (magenta orbits), discharge points (green points) and exclusion zones (blue bars).

The inland stable manifolds divide the regional discharge flow, deflecting to either side of the hyperbolic point. The stable manifolds that intersect the tidal boundary likewise divide the slow flow circulating within the exclusion zone into clockwise or anticlockwise slow motions. The nature of the exclusion zones is now apparent – at high tides, water enters the aquifer at the boundary and a fraction of this water performs long excursions into the aquifer, over many tidal periods, moving slowly towards the hyperbolic point before eventually returning to the boundary guided by the nearest unstable manifold. Three separate hyperbolic points are identified in the section, each with their own stable and unstable manifolds. In this way the aquifer contains significant volumes of fluid sourced from the tidal boundary and from the inland boundary; fluids within these two volumes are segregated by the unstable manifolds and do not intermingle until encountering the discharge region (indicated by green points). Note that stable/unstable manifolds cannot terminate in the fluid interior; the unstable manifolds which appear to terminate at the discharge regions in Figure 15 do so as they have not been fully resolved.

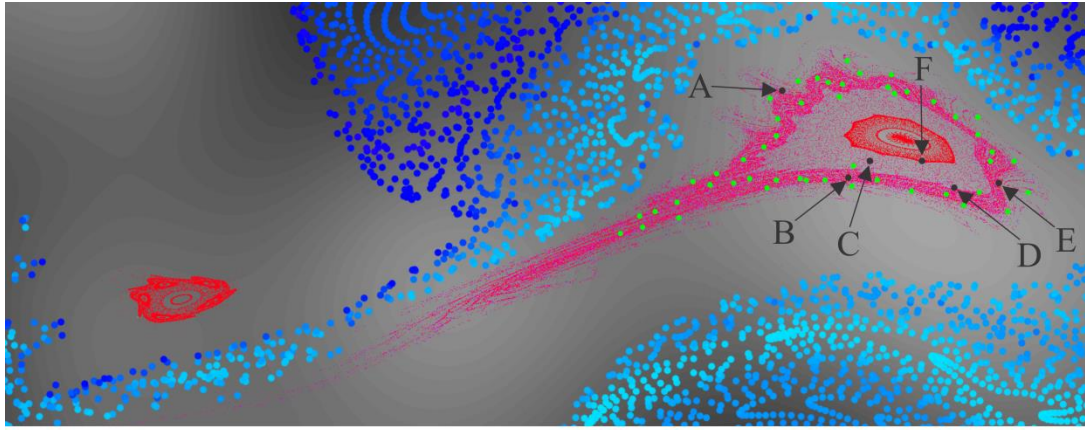
### ***Elliptic Points***

A number of *elliptic points* (E, enclosed by magenta ellipses) are also identified in the Poincaré section. These occur both within the regional discharge flow and within the exclusion zones. The important dynamical characteristic of elliptic points is that they are surrounded by closed orbits of the slow motion, i.e. the orbits are fixed structures within which fluid circulates perpetually, with infinite residence time. These effects are not reflected in the residence time distributions initiated from the regional flow boundary (Figure 13a) since fluid in the elliptic orbits is never released to the discharge boundary (Figure 13b). The presence of elliptic points also indicates the potential for strong flow segregation in the natural tidal system. Figure 15 shows the presence of elliptic points within the aquifer domain

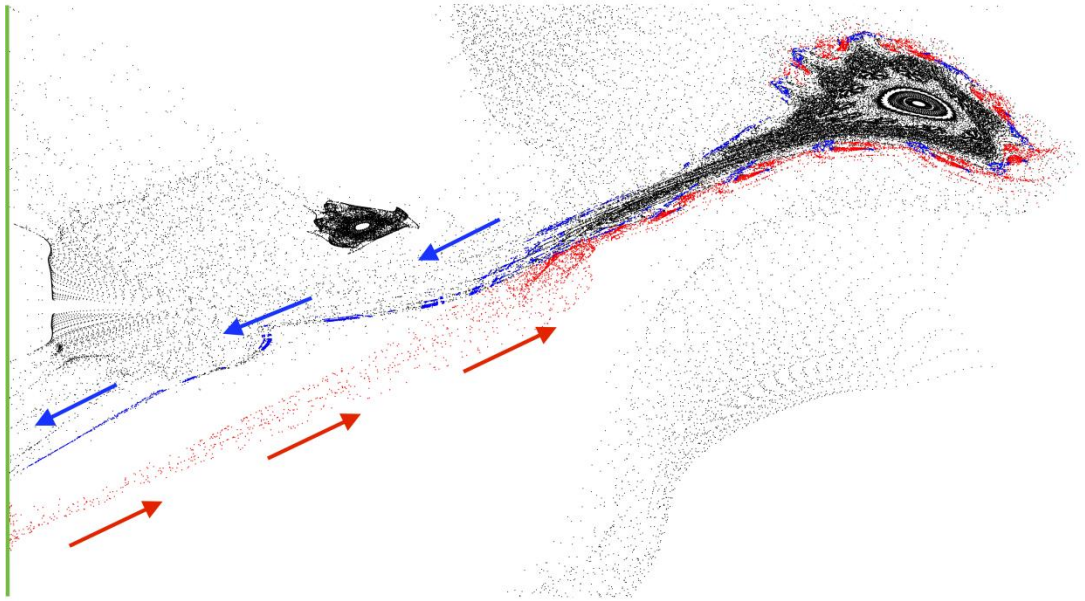
(four labelled E and two associated with stochastic layers), indicating the presence of trapping regions (KAM islands) which hold diffusionless fluid particles perpetually. Even in the presence of diffusion and hydrodynamic dispersion, these finite-sized regions can have a significant impact on solute transport (Lester et al., 2014).

### ***Chaotic Saddles, Stochastic Layers and Cantori***

Two *stochastic layers* are also identified, labelled by S and indicated by blue points. Each stochastic layer surrounds a set of (magenta) elliptic orbits around an elliptic point (unlabelled). Even though the inner elliptic orbits are perfectly closed, the stochastic layers consist of assemblages of finite orbits where fluid is trapped to circulate the elliptic point for long (e.g. hundreds or thousands of tidal periods) but apparently random circulation times, before being released back into the influence of the nearby unstable manifold for eventual discharge to the tidal boundary. Formally, stochastic layers arise from *cantori* which are fractal distributions of elliptic points. Figure 16 shows a high resolution Poincaré section focused on the two stochastic layers in Figure 15. This high resolution section provides a much clearer (though still imperfect) picture of the rich dynamical nature of the stochastic layer and associated cantori.



(a)



(b)

**Figure 16.** (a) Zoomed view of Poincaré section shown in Figure 15, illustrating the stochastic layers (pink dots) and elliptic orbits (red dots) in the mixing regions and regular orbits (blue dots) in the regular regions of the tidal domain. Points are coloured according to residence time, from the least (cyan) to the greatest (red). Roman letters, black and green dots indicate initial positions for FTLE calculations discussed in Subsection 4.6.5. (b) Detail of Poincaré sections for the mixing regions and surrounding non-chaotic structures in (a) as (black dots), showing points associated with stable (red) and unstable (blue) manifolds, respectively, entering and leaving the aquifer domain via the tidal boundary (green line). The

chaotic saddle is the intersection of these manifolds, which surround the elliptic orbits (KAM islands), cantori and stochastic layers.

Figure 16a shows the stochastic layer (pink points) that surrounds the series of nested elliptic orbits (KAM islands) (red points), and the non-chaotic (regular) regions are denoted by cyan and blue points. These points are coloured with respect to the logarithm of residence time, where cyan/blue points leave the domain after  $\mathcal{O}(10)$  periods, pink points  $\mathcal{O}(10^2)$  periods and red points appear to stay within the domain indefinitely. These transport kinematics correspond to the residence time distributions shown in Figure 13c, where indefinitely trapped particles in the KAM islands and cantori are surrounded by long-lived (but finite-time) orbits in the stochastic layer.

Figure 16b illustrates the stable (red) and unstable (blue) manifolds (shown as discrete points rather than the continuous lines shown in Figure 14). For the aquifer model under consideration, the stable and unstable manifolds respectively enter and leave the aquifer domain via the tidal boundary ( $x = 0$ ) rather than having the stable and unstable manifolds near-orthogonal as shown in Figure 14. It is presently unknown whether this behaviour is universal to all chaotic saddles in tidally forced aquifers. The chaotic saddle is formed by the transverse intersection of the stable and unstable manifolds which both enter from the tidal boundary ( $x = 0$ ): the stochastic layer is formed by the chaotic mixing dynamics associated with the heteroclinic tangle between the stable and unstable manifolds, which leads to a fractal (spatial) distribution of residence times in the stochastic layer.

The interplay of transient forcing, compressibility and heterogeneity in periodically forced aquifers leads to complex transport dynamics and a rich Lagrangian topology (all three phenomena are necessary to generate the observed Lagrangian structure; see Section 4.3 and 4.4). Partitioning the Lagrangian topology into distinct regions (which include particle trapping, mixing, particle inflow and outflow) and analysis of the transport within these

regions gives an overview of the complex Lagrangian kinematics within tidally forced heterogeneous aquifers. In Chapter 6 (Section 6.3), we discuss the practical implications of these complex transport dynamics on solute mixing, transport and chemical reactions.

#### 4.6.5. Finite-Time Lyapunov Exponents (FTLEs)

Figure 17 provides FTLE traces calculated from arbitrarily chosen starting locations in the large stochastic layer of Figure 16. The FTLE traces are noisy at short times but become smoother after several hundred  $P$  of elapsed time. The stochastic layers circulate fluids entering the domain at the tidal boundary before releasing them for subsequent discharge. The recirculation times form a random process depending on the particle starting location. Particles at locations A–E all eventually discharge, whereas particles at F circulate indefinitely ( $> 10^3 P$ ). The finite natures of trajectories A–E cause short-term shifts of the FTLE traces as the escaping particles encounter a finite sequence of different Lagrangian regions on their way to the boundary. Thus the FTLE traces in Figure 17 are not monotonically convergent to limiting values, as is common for evaluations of infinite-time Lyapunov exponents ( $\Lambda_\infty$ ). To overcome this estimation problem we calculated FTLE values for a random ensemble of 42 starting locations (green and black dots in Figure 17), gaining an ensemble mean FTLE  $\approx 0.149$  with low standard error. For comparison, Lester et al. (2013) show that pore-scale branching networks have  $\Lambda_\infty \approx 0.12$ . Thus our ensemble of (finite) open flow trajectories in the stochastic layer displays a positive mean FTLE indicative of chaos, while the infinite KAM orbit (F) displays only algebraic ( $\Lambda = 0$ ) deformation.

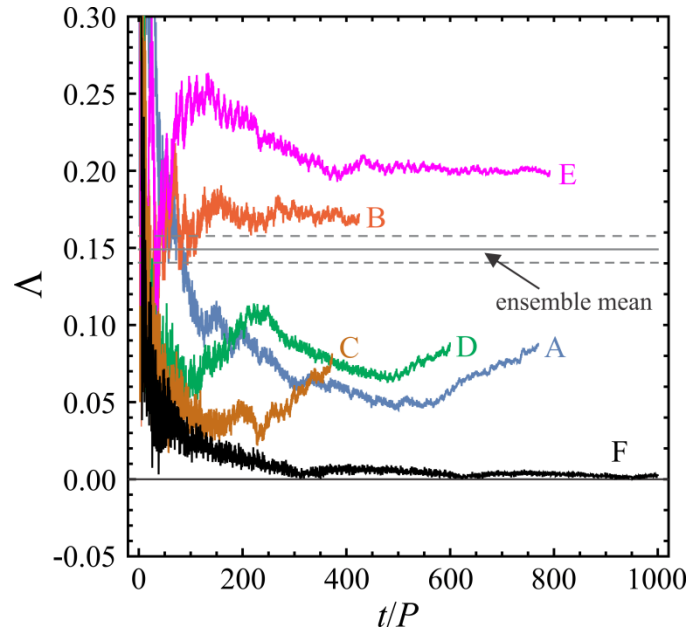


**Figure 17.** Finite-time Lyapunov exponents calculated from five arbitrarily chosen starting locations in the stochastic layer (see Figure 16). All traces eventually exit at the tidal boundary, except trace F (KAM orbit) which does not terminate and was truncated for display. The ensemble mean and standard error bounds are indicated.

#### 4.7. Chapter Summary

The occurrence of chaotic kinematics in groundwater flow is an issue of high relevance for mixing, transport and dispersion (which may cause relevant reactions) and has been received more attention in subsurface hydrology in the past couple of years. Using a conventional linear groundwater flow model subject to tidal forcing, this chapter shows that under time-dependent conditions, these flows generate complex Lagrangian transport and mixing phenomena (chaotic advection) near the tidal boundary. The combination of aquifer heterogeneity, compressibility and transient forcing leads to flow recirculation is responsible for generating non-trivial Lagrangian coherent structures and chaos.

Specialized mathematical techniques and tools (e.g. Poincare sections, RTDs, FTLEs) are used to uncover and quantify underlying transport structures and mixing dynamics. This

chapter found flow reversal leads to two fundamental changes of the aquifer transport structure, the first one is closed orbits that may trap particles for a significant amount of time. The second one is chaotic regions which involve accelerated mixing dynamics and augmented reaction kinetics. Such transport dynamics that are radically different to those of steady Darcy flow.

The key dimensionless parameters (introduced in the Methodology chapter) govern such fundamental changes in the transport structure of tidal aquifers. This chapter used a single set of governing parameters that represent well-characterized tidal systems. In the next chapter, we consider the transport and mixing behaviour of these systems over this dimensionless parameter space.

## Chapter Five

### 5. Parametric Variability of Complex Transport

In the previous chapter, we showed that complex transport dynamics could arise in coastal aquifers with physical properties similar to those of naturally occurring aquifer systems. However, as this study only considered a single set of governing parameters, the parametric dependence of these transport and mixing behaviour of these systems is unknown, as well as the prevalence of complex transport dynamics across natural systems more broadly. To address these questions, in this chapter, we perform a range of simulations using the periodically forced 2D aquifer model introduced in the Methodology chapter to resolve the aquifer transport dynamics over the relevant parameter space. From these results, the key transport characteristics over the flow parameter space are determined, and phase diagrams for the different transport structure topologies (i.e. open, closed or chaotic) are presented. These results are then used to develop mechanistic arguments for how and why transport varies over the parameter space.

#### 5.1. Key Dimensionless Parameters

In Chapter 3 (Methodology), we identified a set of key dimensionless parameters that characterize the dynamics of transiently forced aquifer systems. In addition to these dynamical parameters, there also exists a number of statistical parameters which characterize the heterogeneous hydraulic conductivity field  $K(\mathbf{x})$ . Whilst generation of complex transport dynamics in periodically forced aquifers requires heterogeneity of the hydraulic conductivity field to generate flow reversal; we assume that this phenomenon persists regardless of the particular statistical autocorrelation model used for the conductivity field. Thus, we consider a random log-Gaussian conductivity field  $K$  that is statistically determined by its mean

conductivity  $K_{\text{eff}}$ , log-variance  $\sigma_{\log K}^2$  and correlation length  $\lambda$ . As the Townley number  $\mathcal{T}$  is dependent upon the mean conductivity  $K_{\text{eff}}$ , the set of independent physical parameters that characterize the statistical conductivity field is then  $(\sigma_{\log K}^2, \lambda)$ . These parameters define the conductivity parameter set  $\chi = (\mathcal{H}_t, \mathcal{H}_x, \mathcal{G} \sigma_{\log K}^2)$  which, in conjunction with the dynamical parameter set  $\mathcal{Q} = (\mathcal{T}, \mathcal{G}, \mathcal{C})$ , fully characterize the tidal forcing problem as summarized in Table 1. In this chapter, we analyse the transport structures outlined in the methodology chapter in order to explore the distribution of Lagrangian kinematics over the parameter space and understand of how the underlying physical mechanisms represented by the dimensionless parameters control these transport structures. We also will study advective flow in the linear groundwater model over the tidal flow parameter space  $\mathcal{Q} \equiv \mathcal{T} \times \mathcal{G} \times \mathcal{C}$ , identify regions of anomalous and chaotic transport, and comment on how  $\mathcal{Q}$  and  $\chi$  together control these topological transitions and the underlying physical mechanisms.

**Table 1.** Dimensionless parameters for the tidal forcing problem.

Dimensionless Parameter	Name	Definition	Range	Physical Meaning
<i>Dynamical Parameter Set <math>\mathcal{Q}</math></i>				
$\mathcal{T}$	Townley number	$\mathcal{T} \equiv \frac{L^2 S \omega}{K_{\text{eff}}}$	$[0, \infty)$	Ratio of diffusive and tidal forcing time scales
$\mathcal{G}$	Tidal strength	$\mathcal{G} \equiv \frac{g_p}{JL}$	$[0, \infty)$	Ratio of tidal amplitude to inland head
$\mathcal{C}$	Tidal compression ratio	$\mathcal{C} \equiv \frac{\Delta \varphi}{\varphi_{\text{ref}}} = \frac{S g_p}{\varphi_{\text{ref}}}$	$[0, 1]$	Maximum relative change in porosity due to tidal variation
<i>Conductivity Parameter Set <math>\chi</math></i>				
$\mathcal{H}_t$	Temporal character	$\mathcal{H}_t \equiv \frac{\lambda \varphi_{\text{ref}} \omega}{2\pi K_{\text{eff}}  J }$	$[0, \infty)$	Ratio of Darcy drift and tidal time scales
$\mathcal{H}_x$	Spatial character	$\mathcal{H}_x \equiv x_{\text{taz}}/\lambda$	$[0, L/\lambda)$	Number of correlation scales in the tidally active zone $x_{\text{taz}}$
$\mathcal{G} \sigma_{\log K}^2$	Vorticity number / Flow reversal number	$\mathcal{G} \sigma_{\log K}^2$	$[0, \infty)$	Density of flow reversals in the tidally active zone

Unless stated otherwise, all simulations in this chapter use a  $164 \times 164$  finite difference grid to resolve flow over the 2D hydraulic conductivity field with mean value  $K_{\text{eff}} = 2 \times 10^{-4}$ , log-variance ( $\sigma_{\log K}^2 = 2$ ) and correlation length ( $\lambda = 0.049$ ). We use the finite difference, and particle mapping methods described in Chapter 3 to provide numerical solutions to the flow field  $\mathbf{v}(\mathbf{x}, t)$  and then generate the associated Poincaré sections over the flow parameter space  $\mathcal{Q} = \mathcal{T} \times \mathcal{G} \times \mathcal{C} = (1, 10, 100) \times (1, 10, 100) \times (0, 0.01, 0.02, 0.05, 0.1, 0.2, 0.5)$ . To test the impact of the complexity of the hydraulic conductivity field upon transport, we also perform studies over the hydraulic conductivity parameter space spanned by the log-variance  $\sigma_{\log K}^2$  and correlation length  $\lambda$  as  $(\sigma_{\log K}^2, \lambda) = (0.5, 1, 2, 4) \times (0.025, 0.049, 0.074, 0.098)$ . We also test for statistical invariance in all cases by performing simulations for three different realizations of the random hydraulic conductivity field. Of primary interest are the transport dynamics that arise within the periodically forced aquifer, the topological bifurcations between transport structures and the physical implications of the transport dynamics over the aquifer parameter space defined by  $\mathcal{Q}$  and  $\chi$ . These results will also elucidate the potential ramifications for coastal groundwater systems, e.g. transport, mixing and chemical reactions and uncovers the physical mechanisms that control these processes.

## 5.2. Impact of Tidal Strength and Attenuation on Aquifer Transport

To begin, we consider the impact of both tidal strength and attenuation on the transport dynamics in the tidally forced aquifer by varying the Townley number  $\mathcal{T}$  and tidal strength  $\mathcal{G}$  at a fixed value ( $\mathcal{C} = 0.1$ ) of the tidal compression ratio. The Poincaré sections generated by the distributed injection protocol are shown in Figure 18, where the purple curves indicate the tidal emptying boundary, and the region between this boundary and the tidal boundary ( $x = 0$ ) is the tidal emptying region which indicates the part of the aquifer for which intense mixing between freshwater and saltwater occurs over a single flow period. We also note that the

rightmost boundary (brown) in Figure 18 is the *inland boundary*, given by the location of particles that have been seeded along the inland boundary ( $x = L$ ) after one flow period. Whilst this boundary gives some information regarding inland transport; this is of less physical importance than the tidal emptying boundary ( $x = 0$ ) as the inland domain boundary ( $x = L$ ) is arbitrary in that it represents the extent of the computational domain.

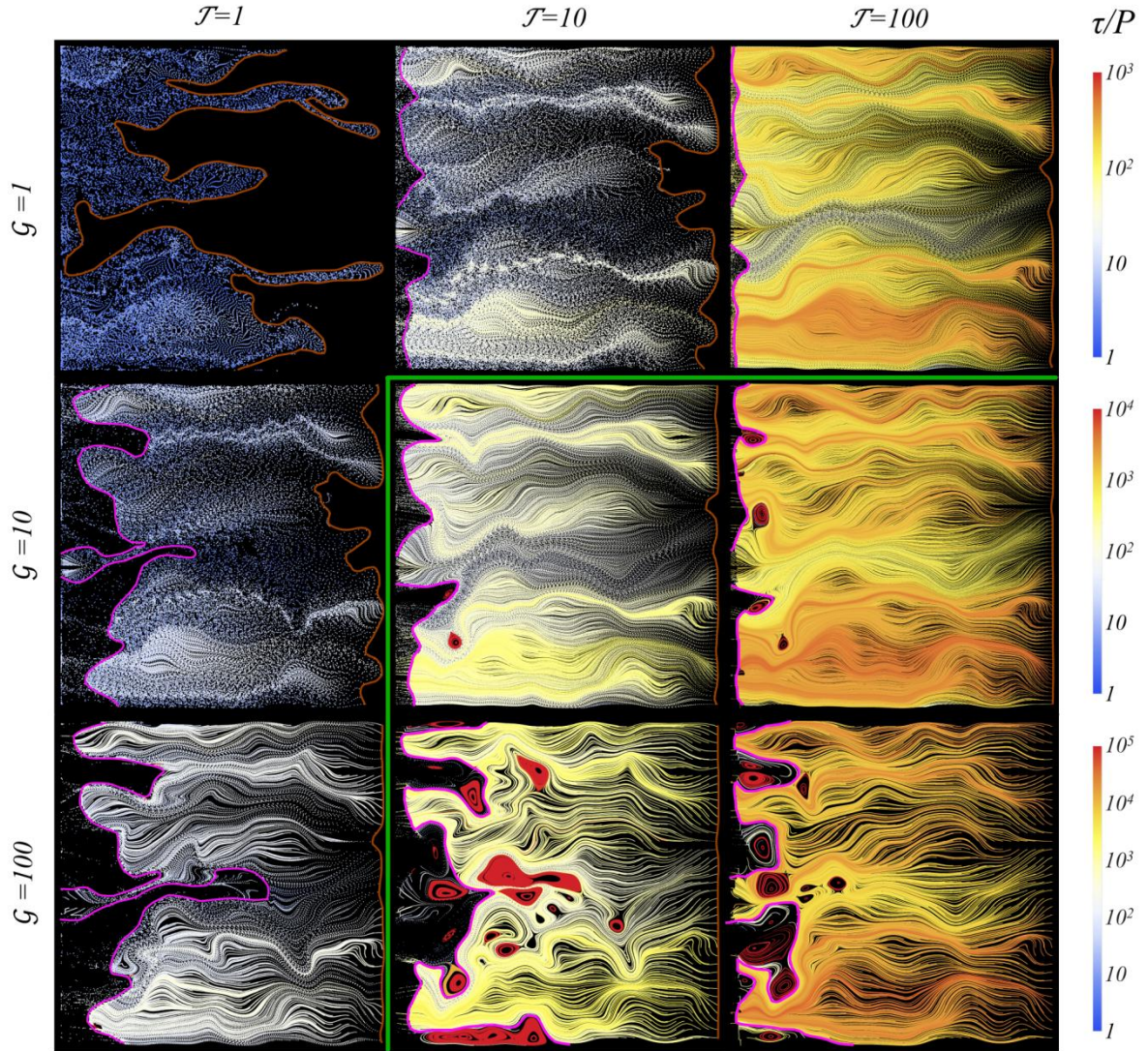


**Figure 18.** Summary of Poincaré sections for  $\mathcal{C} = 0.1$  calculated via the distributed injection of particles. Particle trajectories are coloured according to residence time, from shortest (blue) to longest (red), and the colour scales change with  $\mathcal{G}$ . Green lines indicate Poincaré sections

that possess trapped orbits. Purple and brown curves are the tidal emptying and inland boundaries respectively.

The grid of Poincaré sections shown in Figure 18 contains rich information about the transport dynamics throughout the aquifer domain and their variation with the control parameters. When the value of either the Townley number  $\mathcal{T}$  or tidal strength  $\mathcal{G}$  is small ( $< 10$ ), all of the time-averaged particle orbits have open trajectories that travel from the inland boundary ( $x = L$ ) to the tidal emptying boundary in a manner similar to that of steady Darcy flow. Conversely, when both  $\mathcal{T}$  and  $\mathcal{G}$  are larger ( $> 10$ ), these time-averaged orbits undergo a topological bifurcation to admit localized closed orbits (trapping regions) and periodic points. This transition is predicted by the temporal character  $\mathcal{H}_t$  which measures the propensity for flow reversal to occur and increases with both  $\mathcal{T}$  and  $\mathcal{G}$ . If the value of  $\mathcal{H}_t$  is large, particles will drift many tidal periods, but their elliptical velocity orbits become too small to generate significant flow reversal. The spatial character  $\mathcal{H}_x$  provides information on how many vortices are likely to occur within the aquifer, so complex transport arises when  $\mathcal{H}_x$  is greater than one. As shown in Figure 18, both  $\mathcal{H}_x$  and the width of the tidally active zone decrease with increasing  $\mathcal{T}$ , and these values increase with increasing tidal strength  $\mathcal{G}$ . Hence, complex transport structures arise for moderate values of  $\mathcal{T}$  and large values of  $\mathcal{G}$ . These trends persist for different values of the tidal compression ratio  $\mathcal{C}$  beyond that ( $\mathcal{C} = 0.1$ ) used in Figure 18.

The closed regions shown in Figure 18 occur in both the aquifer bulk and in the tidal emptying region, with significant implications for transport of solutes. If trapped regions in the tidal emptying region are initially filled with fresh water, then these trapped regions represent “islands” of freshwater within a “sea” of brackish water in the tidal emptying region, where salt may only enter via diffusion or dispersion. In Chapter 6 (Section 6.2), we show

that these regions persist for long times and strong concentration gradients are expected at their boundaries. Conversely, trapped regions within the aquifer bulk may represent islands of different water composition to that of the fluid entering via the inland boundary ( $x = L$ ), and the only transport mechanism into or out of these regions is diffusion or dispersion. Hence these augmented dynamics and concentration gradients will have strong impacts upon transport, mixing and chemical reactions within the aquifer.

As the parameter intervals for  $\mathcal{T}$  and  $\mathcal{G}$  in Figure 18 are too broad to accurately discriminate the flow structure transition boundary, we improve resolution of the parameter space to the values  $\mathcal{T}, \mathcal{G} = (1, 2, 5, 10, 20, 50, 100)$  for  $\mathcal{C} = 0.01$  and  $\mathcal{C} = 0.1$  and summarize the observed transport structure types in Figure 19. Using this higher resolution, we observe a bifurcation to closed time-averaged orbits for a broad range of  $\mathcal{T}$  values when  $\mathcal{G} \gtrsim 50$  for  $\mathcal{C} = 0.01$  and  $\mathcal{G} \gtrsim 10$  for  $\mathcal{C} = 0.1$ . No evidence of chaotic trajectories was observed in these simulations for the tidal compression ratios  $\mathcal{C} = 0.01$  and  $0.1$ . As expected, we observe an increase in the probability of closed orbits with increasing  $\mathcal{T}, \mathcal{G}, \mathcal{C}$  across all cases computed.

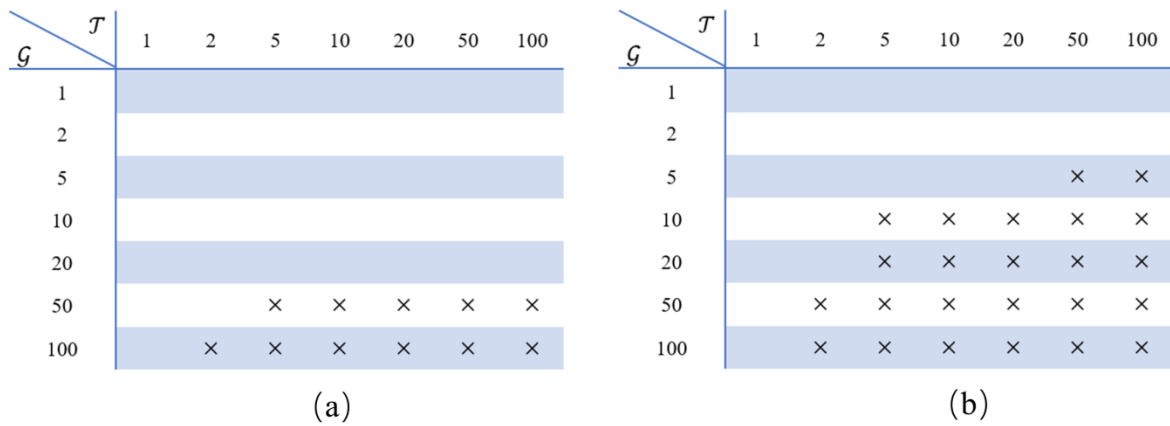


**Figure 19.** Summary of transport simulations that exhibit closed transport structures (as indicated by crosses) for compressibility ratio (a)  $\mathcal{C} = 0.01$  and (b)  $\mathcal{C} = 0.1$ .

### 5.3. Impact of Aquifer Compressibility on Transport

To understand the role of aquifer compressibility on transport, we now vary the compressibility parameter  $\mathcal{C}$ . Figure 20 shows a series of aquifer Poincaré sections using the distributed injection protocol at various values of  $\mathcal{C}$  in the range  $\mathcal{C} = 0 - 0.5$  for  $\mathcal{T} = 10$  and  $\mathcal{G} = 100$ . With increasing  $\mathcal{C}$ , the particle drift velocity increases and the tidal emptying region widens. In Chapter 4 (Section 4.4), we predicted that fluid tracer particle trajectories are integrable for incompressible ( $\mathcal{C} = 0$ ) aquifers, which means they propagate in an oscillatory manner along smooth 1D streamlines and so cannot exhibit trapping or chaotic dynamics. Figure 20 confirms that particle trajectories are indeed confined to 1D orbits for  $\mathcal{C} = 0$ , and this behaviour appears to extend to very weakly compressible aquifers ( $\mathcal{C} = 0 - 0.002$ ). Closed particle orbits are observed for weakly compressible aquifers ( $\mathcal{C} = 0.005 - 0.1$ ), whereas strongly compressible aquifers ( $\mathcal{C} = 0.2 - 0.5$ ) undergo a further topological bifurcation to exhibit chaotic transport structures, as indicated by the chaotic saddles highlighted in Figure 20.

As the region of parameter space  $(\mathcal{T}, \mathcal{G}, \mathcal{C})$  for which chaotic transport is observed is a subset of that for which closed time-averaged orbits are observed, we hypothesize that as either  $\mathcal{T}$ ,  $\mathcal{G}$  or  $\mathcal{C}$  are increased, the basic transport structure may bifurcate from open to closed orbits and admit periodic points that may be classed as elliptic (E) or hyperbolic (H). With further increases in  $\mathcal{T}$ ,  $\mathcal{G}$  or  $\mathcal{C}$ , the stable and unstable manifolds associated with the hyperbolic periodic points intersect transversely, corresponding to a bifurcation to chaotic transport dynamics, with important transport implications beyond that of simple trapping in closed orbits. Thus, there exists a hierarchy of transport complexity in periodically forced aquifers based on the route to chaos in aquifer flow structures as described above.

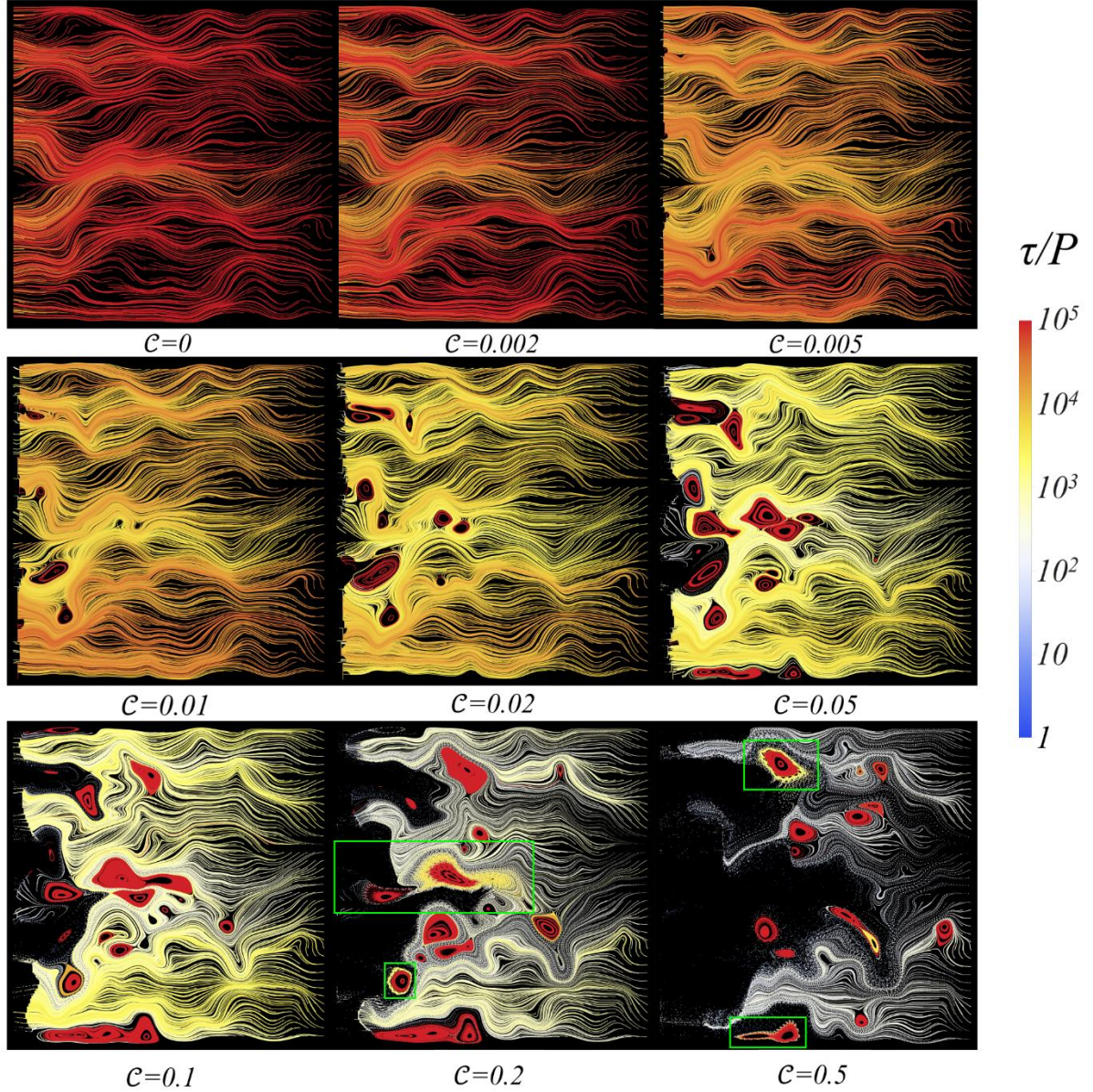


**Figure 20.** Poincaré sections in the periodically forced aquifer under the distributed injection protocol for different values of  $C$  over the range  $C = 0 - 0.5$  for  $T = 10$  and  $G = 100$ . Green rectangles identify chaotic transport structures.

#### 5.4. Sensitivity to Hydraulic Conductivity Field

All numerical treatments of Darcy flow in porous media depend on the model chosen to represent conductivity heterogeneity. Of primary interest, however, is the essential physics of the studied flow, i.e. those features which are robust to both the class and details of the conductivity model. In Chapter 4, we used a simple Gaussian autocorrelation function for

log-conductivity that is statistically determined by the mean conductivity ( $K_{\text{eff}}$ ), conductivity log-variance ( $\sigma_{\log K}^2$ ) and correlation length ( $\lambda$ ) to analyze the transport structure of the associated flow field. The concept was that if complex transport dynamics can occur in these simple conductivity fields, then it is possible that similar dynamics will occur in more sophisticated geostatistical models. Here we examine how the transport structures of these flows vary with the statistical parameters of the Gaussian autocorrelation model. Specifically, we consider the effects of different spatial realizations of the conductivity field, different correlation lengths ( $\lambda = 0.025, 0.049, 0.074, 0.098$ ) and different log-variances ( $\sigma_{\log K}^2 = 0.5, 1, 2, 4$ ). Whilst these smaller correlation lengths and larger log-variances may demand greater numerical resolution to accurately resolve these flows; we find the original finite-difference grid is sufficient to accurately resolve these cases. We also study the sensitivity of the type and number of predicted transport structures by generating a set of different realizations of the log-conductivity fields according to the algorithm of Ruan and McLaughlin (1998).

#### 5.4.1. Statistical Invariance of Model Predictions

Figure 21 shows three arbitrary realizations of the log-conductivity field (for fixed  $K_{\text{eff}}$ ,  $\sigma_{\log K}^2$  and  $\lambda$ ), with the corresponding shaded density maps in the top row. For each realization, the Poincaré sections are provided for two different dynamical parameter sets (see figure caption for details). The three realizations provide similar flow topologies for each of the two dynamical parameter sets, i.e. within each row, the numbers and densities of periodic points are similar, as are the spatial extents of the tidal emptying zones. Further testing indicates that these similarities persist between realizations over a broader range of dynamical parameters (results not shown). Thus, there is no essential change in the Lagrangian topologies arising from change of log-conductivity realization, although the Poincaré sections differ in detail.

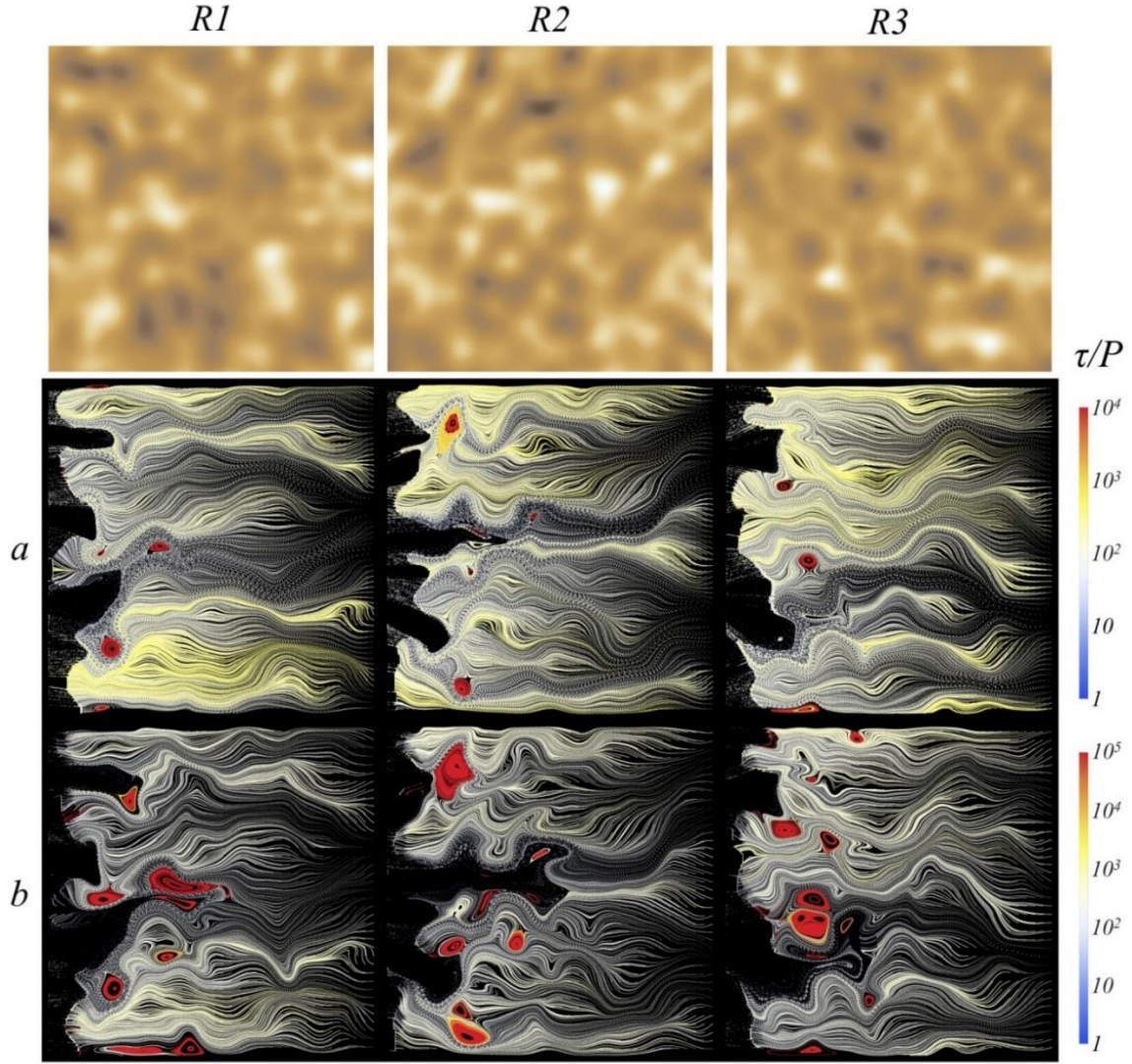


**Figure 21.** Density map of log hydraulic conductivity for three different realizations of the log-Gaussian hydraulic conductivity field and associated Poincaré sections (distributed injection) for two cases, row a:  $\mathcal{T} = 20$ ,  $\mathcal{G} = 10$ ,  $\mathcal{C} = 0.2$ , row b:  $\mathcal{T} = 5$ ,  $\mathcal{G} = 50$ ,  $\mathcal{C} = 0.1$ .

#### 5.4.2. Impact of Correlation Length

Figure 22 illustrates the effect of different correlation lengths ( $\lambda = 0.025, 0.049, 0.074, 0.098$ ) upon the aquifer transport structures for the fixed dynamical parameters  $\mathcal{T} = 10$  and  $100$ ,  $\mathcal{G} = 100$ ,  $\mathcal{C} = 0.1$  and log-conductivity variance  $\sigma_{\log K}^2 = 2$ . As expected, the size and extent of the resulting closed flow regions are controlled by the correlation length in that as  $\lambda$  increases, fewer and larger closed flow regions occur in the domain. These results indicate

that the correlation length is a key aquifer property that controls the size of closed regions within the flow, and in Chapter 6 (Section 6.3) of the manuscript, we show that this size is important in the transport of dispersive solutes.

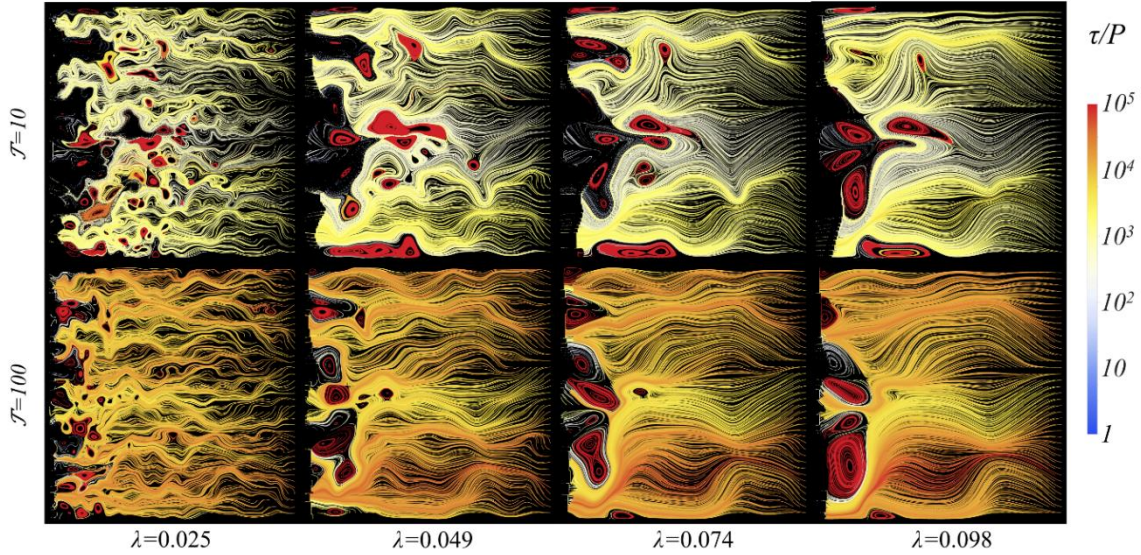


**Figure 22.** Poincaré sections (distributed injection) for  $\mathcal{G} = 100$  and  $\mathcal{C} = 0.1$  with varying  $\mathcal{T}$  and  $\lambda$ .

Figure 23 shows that the average radius of trapped regions for two cases where  $\mathcal{G} = 100$ ,  $\mathcal{C} = 0.1$  and  $\mathcal{T}$  varies between 10 and 100 against a range of correlation lengths ( $\lambda = 0.025, 0.049, 0.074, 0.098$ ). For both cases, this mean radius of trapped regions increases linearly with correlation length  $\lambda$  and this rate of increase also decreases with Townley number  $\mathcal{T}$ . This is expected as decreasing  $\mathcal{T}$  corresponds to increasing width of the tidal region and a larger number of trapped regions in the aquifer domain.

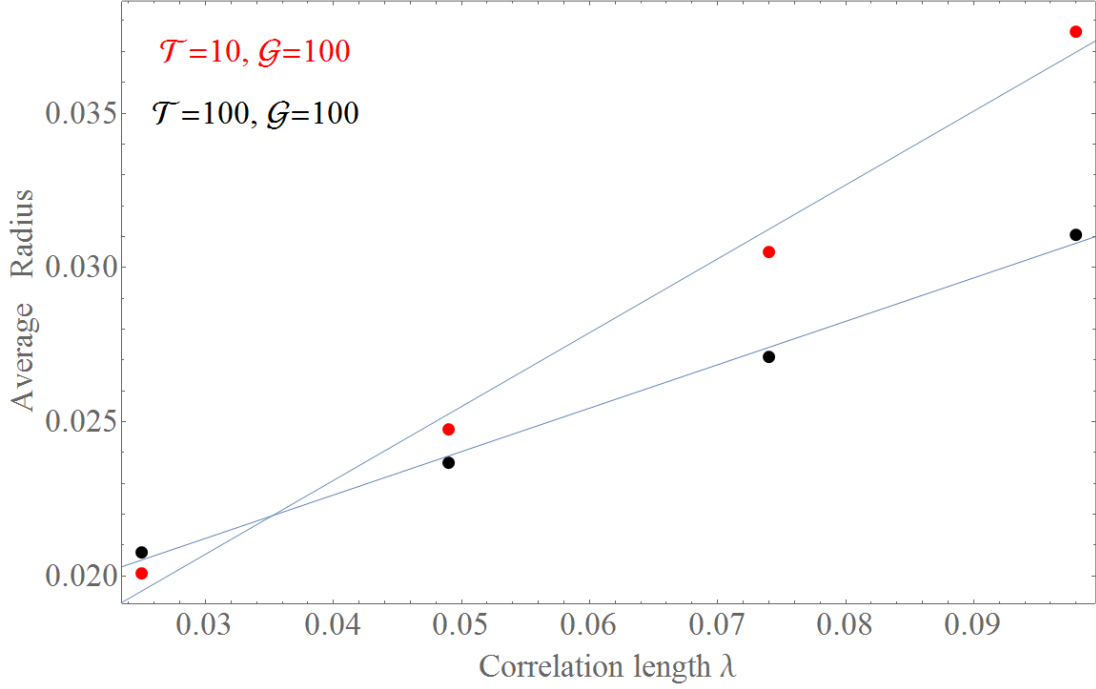


**Figure 23.** Average radius of trapped regions in the aquifer for different values of the correlation length  $\lambda$  for two cases ( $\mathcal{T} = 10$  and  $100$ ) with fixed tidal strength and compressibility ( $\mathcal{G} = 100, \mathcal{C} = 0.1$ ).

In Chapter 3, we introduced numerical methods to generate self-consistent numerical solutions to physically constrained flows and accurate advection methods to construct Poincaré sections. It was shown that the accuracy of the method for generating physically constrained flows declines as log-conductivity variance  $\sigma_{\log K}^2$  increases and as the spatial resolution  $\lambda/\Delta$  is reduced (where  $\Delta$  is the spatial resolution of the finite difference grid). Thus, while the sections in Figure 22 show a trend of increasing structure and complexity as  $\lambda/\Delta$  *decreases*, the accuracy of the underlying flow fields increases as  $\lambda/\Delta$  *increases*. Even so, it is clear from the figure that the calculated time-averaged particle trajectories are smoothly varying for increasing  $\lambda/\Delta$ .

### 5.4.3. Impact of Conductivity Variance

We measure the effect of different log-conductivity variances ( $\sigma_{\log K}^2 = 0.5, 1, 2, 4$ ) with fixed correlation lengths  $\lambda = 0.049$ . As shown in Chapter 4 (Section 4.3), flow reversal plays a critical role in generating complex transport dynamics. Log-conductivity variance controls the magnitude of vorticity and so is strongly correlated with flow reversal. Hence, the density of canonical flux ellipses is related to the reversal number  $\mathcal{G} \sigma_{\log K}^2$ . Figure 24 shows that as the reversal number increases, the number and size of closed flow regions increases until these closed regions bifurcate into chaotic regions (for  $\sigma_{\log K}^2 = 4$ ).

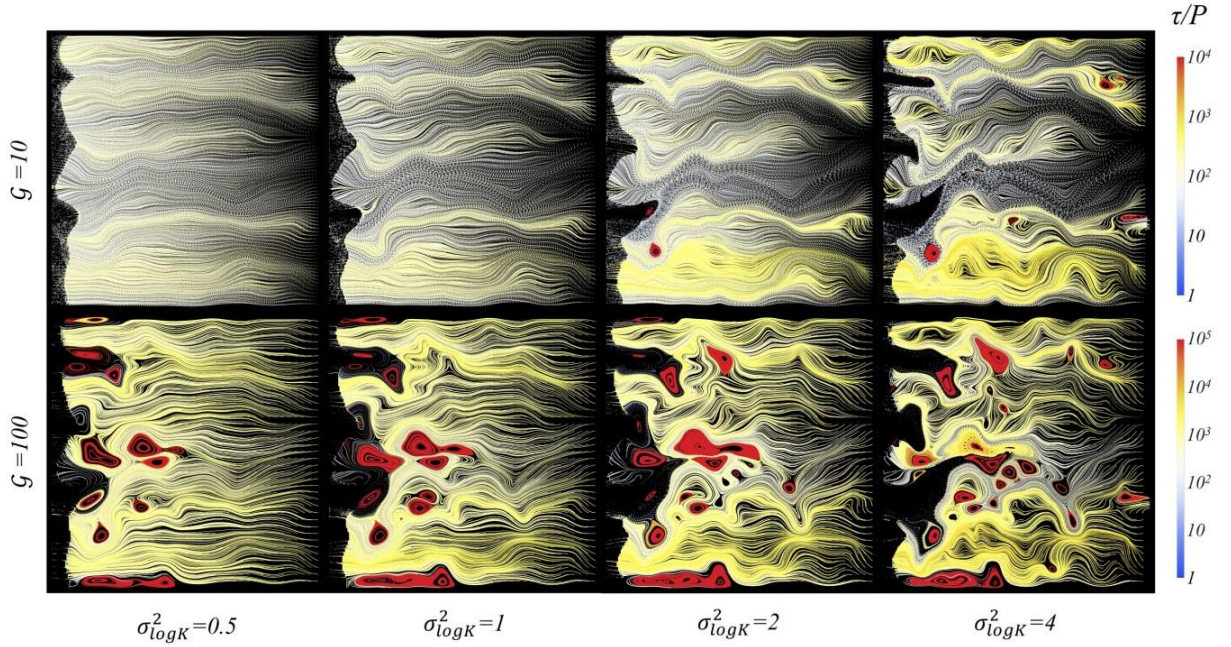


**Figure 24.** Poincaré sections (distributed injection) of flow in a single log- $K$  realization for  $\mathcal{T} = 10$  and  $\mathcal{C} = 0.1$  with varying  $\mathcal{G}$  and  $\sigma_{\log K}^2$ .

## 5.5. Chapter Summary

In this chapter, we investigated the various transport structures and dynamics that can arise in tidally forced aquifers across the dimensionless parameter space which spans the Townley number ( $\mathcal{T}$ ), relative tidal strength ( $\mathcal{G}$ ), and tidal compression ratio ( $\mathcal{C}$ ). We also

tested the impact of the independent statistical parameters of the log-Gaussian hydraulic conductivity field  $(\sigma_{\log K}^2, \lambda)$  upon solute transport and mixing.

For the dynamical parameter set  $\mathcal{Q} = (\mathcal{T}, \mathcal{G}, \mathcal{C})$ , the interplay between tidal forcing and aquifer compressibility induce topological bifurcations of the aquifer transport structure, i.e. the observed transport structures change from open to closed to chaotic with either increasing  $\mathcal{T}$ ,  $\mathcal{G}$  or  $\mathcal{C}$ . These bifurcations fundamentally change the organization of fluid trajectories in the aquifer, and these three different types of transport structures arise at particular combinations of the dynamical parameter set  $\mathcal{Q}$ . We observe complex transport dynamics (which include both closed regions and chaotic dynamics) over a large proportion of the dimensionless parameter space, suggesting that such dynamics may be highly relevant to natural aquifer systems.

For the independent conductivity parameters  $(\sigma_{\log K}^2, \lambda)$ , we found that the correlation length scale  $\lambda$  is a key aquifer property that controls the size of closed regions within the flow, and the log-conductivity variance  $\sigma_{\log K}^2$  controls the magnitude of vorticity and can act as a surrogate for flow reversal. These results indicate that the Lagrangian complexity of the periodic flow system varies smoothly with key heterogeneity parameters (correlation length, log-variance) of the Gaussian statistical model and that our observations of transport dynamics are robust to common heterogeneity variations. Further studies using different statistical models for the heterogeneity field, such as multi-Gaussian, kriged and fractal models, would provide valuable checks and further insight.

## Chapter Six

### 6. Discussion and Physical Relevance for Natural Coastal Aquifers

In the previous chapters, we have established the prevalence and mechanisms of complex transport dynamics in tidally forced aquifers. These observations of complex Lagrangian phenomena alter our understanding of the possible modes of transport in these systems and have significant implications for solute transport. In this chapter, we consider the prevalence of these dynamics in natural aquifer systems and the potential impacts of these transport dynamics on transport, mixing and reactions. We present a phase diagram of the observed transport structures over the parameter space  $\mathcal{Q} = (\mathcal{T}, \mathcal{G}, \mathcal{C})$  and use these results to estimate the prevalence of complex transport in natural coastal aquifer systems around the globe. We also estimate the impacts of closed regions of the flow upon the trapping of solutes undergoing diffusion and hydrodynamic dispersion.

#### 6.1. Implications for Transport and Reaction

##### 6.1.1. Residence Time Distributions - Segregation and Singularity

In the parametric studies undertaken in Chapter 5, we saw that a range of complex transport dynamics could arise in transiently-forced aquifer systems. It was observed that the residence time distribution of fluid in the aquifer domain was singular (infinite) at closed regions of the flow that are controlled by elliptic periodic points. In addition, regional flux was diverted into several discrete discharge zones along the tidal boundary, and the fluids discharging in these zones had undergone complicated braiding dynamics which may mix and mask geochemical signatures. At other locations along the boundary, there were intervals of recirculation (with widths of the order of the log-conductivity correlation length  $\lambda$ ) where tidal fluids embarked on long incursions into the aquifer domain, lasting many tidal periods,

before eventually returning and discharging at the boundary. Thus, taken as a whole, fluids discharging along the tidal boundary may have vastly different (and possibly indeterminate) geochemical and chronological origins. This behaviour is fundamentally different from the familiar discharge dynamics for steady flow in heterogeneous domains (see the blue curve in Figure 10). Conventional groundwater sampling techniques near discharge boundaries, e.g. multilevel samplers and spear probes, may variously source fluids from an ensemble of histories and qualities. High sampling density, in space and time, maybe the best practical defence against these unpredictable effects in poorly characterized aquifers.

#### **6.1.2. Flow Reversal, Traceability and Reaction**

The origin of these complicated transport dynamics can be traced back to reversal of the Darcy flux vector during the tidal forcing period over a significant proportion of the aquifer domain (see Figure 12), leading to a fundamental change in the Lagrangian topology from open, parallel streamlines to the formation of periodic points, separatrices, non-mixing islands and chaotic saddles (see Figure 14, Figure 15). Moreover, our observations of punctuated inflow/outflow regions along the tidal boundary ( $x = 0$ ) significantly alter understanding of transport in these regions, especially from the perspective of, for example, salt water intrusion. Such complex transport dynamics are incompatible with many solute transport and biogeochemical reaction modelling studies which tend to rely on the identification of simple mean flow paths along which complicated mass balance and reaction kinetic calculations can be made. Conceptually, our results suggest that determination of the fate (provenance) of reacting fluids simply by (back-) tracking along an approximate steady streamline may well be a source of significant model error in tidal discharge environments. That is, determination of mean fluid flow paths for geochemical reaction modelling and transport may not be appropriate or even possible in some tidally forced groundwater discharge settings. In addition, it has been shown (Tél et al., 2005) that the complex mixing

dynamics that arise within chaotic regions can profoundly alter a wide range of chemical and biological reaction rates. Intriguingly, Ding et al. (2017) note that a high-resolution Lagrangian method can account for the well known upscaling effect on reaction rates, which reinforces the need for appropriately resolved flows as inputs to transport and reaction models.

The highly oscillatory nature of particle motion near the tidal boundary (see Figure 11) can also significantly skew estimates of tracer migration speed. Although the net displacement of a particle over a tidal period  $P$  may be small, the mid-cycle particle displacement can be much larger. Noting that most tidal spectra are multi-modal and that the Townley number  $\mathcal{T}$  is frequency-dependent, the appropriate sampling frequency may be a function of sampling location in the aquifer. It is clear from our results that tracer test analysis in strongly tidally influenced aquifers is potentially fraught.

## 6.2. Potential for Chaos in Field Settings

It is important to consider how the dimensionless parameter set  $\mathcal{Q} = (\mathcal{T}, \mathcal{G}, \mathcal{C}) = (10\pi, 10, 0.5)$  and conductivity parameters ( $\sigma_{\log K}^2 = 2, \lambda = 0.049$ ) of the example problem considered in Chapter 4 relates to those of typical coastal aquifers. Noting that the product  $\mathcal{G} \sigma_{\log K}^2$  correlates well with the density of canonical flux ellipses in the tidally active zone, in order to assess the relevance of these parameter values to field studies we estimate  $\mathcal{T}$  and  $\mathcal{G} \sigma_{\log K}^2$  values from a set of published coastal aquifer studies. The study locations are the Dridrate Aquifer, Morocco (D, sand and limestone; Fakir (2003)), Garden Island (GI, sand and limestone; Trefry and Bekele (2004)), Jervoise Bay (J, sand and limestone; Smith and Hick (2001)) and Swan River (SR, sand and clay; Smith (1999)), all in Western Australia, Largs North, South Australia (LN, sand and clay; Trefry and Johnston (1998)), and Pico Island, Azores (P, basalts, Cruz and Silva (2001)). Figure 25 plots these studies in  $\mathcal{T} -$

$\mathcal{G} \sigma_{\log K}^2$  space with error bars indicating uncertainty in hydrogeological parameter estimates. The GI, SR and J studies include multiple data points due to the use of frequency-resolved techniques. Estimates of  $\sigma_{\log K}^2$  are rare in tidal analyses although suitable estimation techniques exist (see e.g., Trefry et al. (2011)). The following ranges of  $\sigma_{\log K}^2$  were assumed: 0.5 - 2.5 (sand and limestone, sand and clay), 2.0 - 6.0 (basalts). Figure 25 shows that the example problem considered in Chapter 4 (star) lies well within the range of  $\mathcal{T}$  values of the field studies but at the upper end of the estimated flow reversal ( $\mathcal{G} \sigma_{\log K}^2$ ) values.

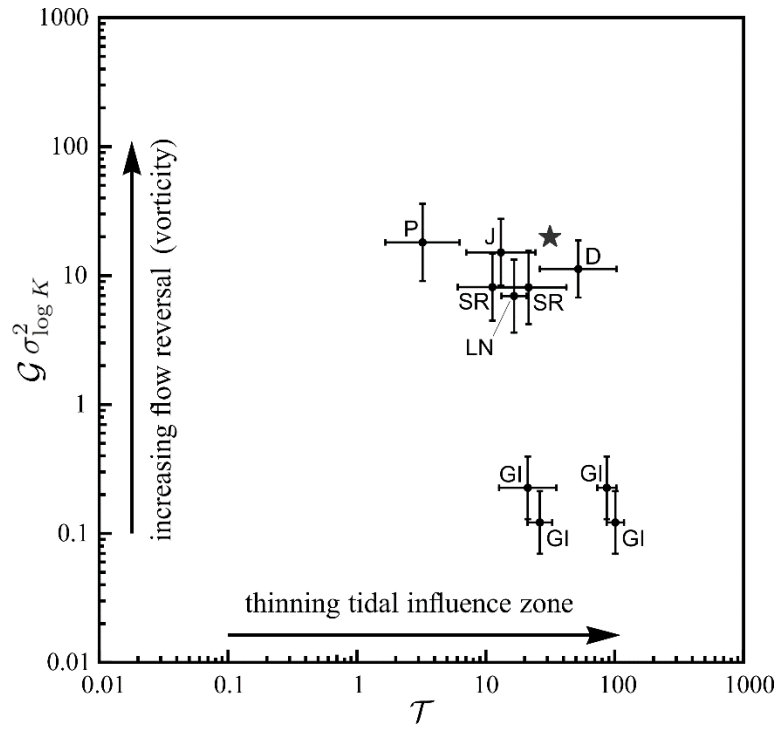


**Figure 25.** Location of the present example system (star) in  $\mathcal{T} - \mathcal{G} \sigma_{\log K}^2$  parameter space. Locations of some field studies (letters on error bars) reported in the literature are provided for reference.

The tidal compression ratio  $\mathcal{C} = S g_p / \varphi_{\text{ref}}$  is also a key parameter. As porosity  $\varphi_{\text{ref}}$  is not always well characterized in tidal aquifer studies, we resort to literature values for soil physical parameters (Domenico & Mifflin, 1965; Morris & Johnson, 1967). For sand and

limestone soils,  $\varphi_{\text{ref}}$  ranges from 0.2 - 0.5, while for sand and clay soils the range is 0.15 - 0.4. Basalts, often with significant fracture porosity, may show  $\varphi_{\text{ref}}$  in the range 0.03 - 0.35. Specific storages  $S_s$  typically range up to  $10^{-2} m^{-1}$  (sand and limestone, sand and clay) and  $10^{-4} m^{-1}$  (fractured rock), while tidal amplitudes can be as large as 10 m. With these ranges, the maximum  $\mathcal{C}$  values that can be anticipated are approximately 0.05 (sand and limestone), 0.4 (sand and clay) and 0.02 (basalts), but lower tidal amplitudes will reduce these proportionately. Thus we see that the example problem, with  $\mathcal{C} = 0.5$ , is at the high end of likely values in field settings, closest to a clay and sand matrix influenced by high tidal amplitude. It is beyond the scope of this study to identify specific instances of Lagrangian chaos in coastal aquifers, but the preceding analysis shows that the parameter choices in the example problem are not far removed from reality and there is a good prospect of complex transport structures being present near discharge boundaries in many field settings. Note that complex transport structures (such as closed regions of the flow) formally exist for any value of  $\mathcal{C} > 0$ ; however, the smaller the value of  $\mathcal{C}$ , the slower the overall Lagrangian transport and the more likely that diffusion/dispersion will be of similar importance as advection.

However, whether such structures may be detected in field investigations is another matter altogether. Submarine groundwater discharge (SGD) mapping techniques are directly relevant to the detection of Lagrangian structures in coastal systems, but the uncertainties involved in SGD are significant. Firstly, coastal discharge zones often display complex geomorphology, topography and fully three-dimensional heterogeneity at a range of spatial scales. This complexity is sufficient to render the SGD measurement task onerous, even at relatively poor spatial resolution. Once gathered, the measurements show significant spatial and temporal variability due to geological structure, temporal variations in flow regime, and measurement uncertainty. The measurement variability is often rationalized in terms of (unresolved) preferential flow paths (see, e.g., Hosono et al. (2012); Smith et al. (2003)),

although other mechanisms including density effects, wave action (Smith et al., 2009) and tidal and weather system influences are also reported to be important (Kobayashi et al., 2017). Our results indicate that tidal forcing introduces a new dynamical mechanism for generating preferential flow paths via the establishment of interior hyperbolic points, resulting in segregation of regional flow into discrete discharge zones. It remains to be seen whether techniques can be developed to isolate the presence and quantify the effects (on flow, mixing and reaction) of Lagrangian structures in coastal systems. Nevertheless, the potential for complex transport dynamics in these systems must be recognized and assessed.

### **6.3. Solute Trapping and Transport**

In this section, we consider the impact of closed transport regions upon solute transport by considering both the size distribution of closed regions across the parameter space and the impact of the size of trapped regions upon solute diffusion and dispersion.

#### **6.3.1. Size Distribution of Closed Regions**

When closed regions do occur within the aquifer, both the location (i.e. whether in the tidal emptying region or the aquifer bulk) and size distribution of these regions have important implications for solute transport, as solutes will more rapidly disperse out of smaller closed regions. We use tracer particle RTDs under the distributed injection protocol to determine the total of the area ( $a$ ) of trapped regions in the aquifer, where particles with indefinite RTDs are taken to be trapped within the aquifer. The resultant RTD histogram (probability density function) for  $\mathcal{T} = 100$ ,  $\mathcal{G} = 100$  and  $\mathcal{C} = 0.1$  is shown in Figure 26a. Particle tracking is performed up to  $\tau/P = 10^5$ , most tracer particles leave the domain within  $4 \times 10^4$  periods, but a significant proportion (4.28%) are confined indefinitely which are deemed to be trapped regions.

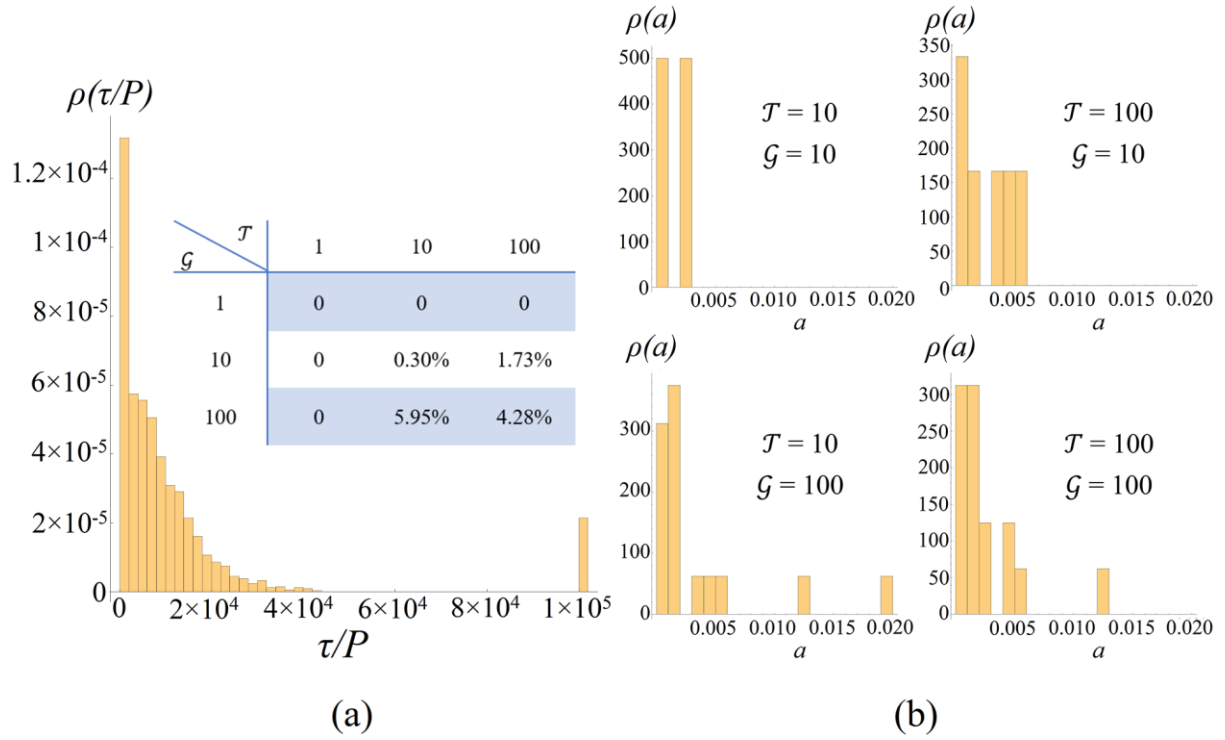


**Figure 26.** (a) Residence time distribution of fluid particles for the distributed injection protocol for  $\mathcal{T} = 100$ ,  $\mathcal{G} = 100$  at  $\mathcal{C} = 0.1$ . Inset: total of the area (a) of trapped regions (closed orbits) as a proportion of aquifer area for various values of  $\mathcal{T}$  and  $\mathcal{G}$  at  $\mathcal{C} = 0.1$ . (b) Histograms (probability density function) of the relative area (a) of individual trapped regions in the aquifer for various values of  $\mathcal{T}$  and  $\mathcal{G}$  at  $\mathcal{C} = 0.1$ .

The inset of Figure 26a summarizes the relative total area of trapped regions (closed orbits) in the aquifer for various values of  $\mathcal{T}$ ,  $\mathcal{G}$  at  $\mathcal{C} = 0.1$ . Whilst the total trapped area is large for  $\mathcal{T} = 10$ ,  $\mathcal{G} = 100$ , the total trapped area is smaller for  $\mathcal{T} = 100$ ,  $\mathcal{G} = 100$  due to the smaller tidal region shown in Figure 18. Figure 26b indicates that trapped regions are typically smaller for small values of  $\mathcal{T}$  and  $\mathcal{G}$ , but with parameter increases, the trapped regions increase in size and coalesce into fewer but larger regions. As we show explicitly in the next section, larger trapped regions trap diffusive solutes for a much longer time and so represent significant regions of retarded transport.

### 6.3.2. Solute Transport across Trapped Regions

Whilst the analysis in this study focuses predominantly upon the advection processes that govern these transport structures; solutes are typically transported by a combination of advection and diffusion or hydrodynamic dispersion. In the presence of dispersive transport mechanisms, closed regions of the flow become regions of retarded transport. To provide an order-of-magnitude estimate of the transport rate of solutes into or out of these regions, we approximate the trapped region as a disc of radius  $R_0 L$  (such that  $R_0$  is the disc radius relative to the aquifer dimension  $L$ ) that is surrounded by fluid with zero solute concentration in the open region of the flow. This estimate considers the dispersive “leakage” of the solute concentration field  $\mathbf{c}(\mathbf{x}, t)$  out of such a trapped region subject to homogeneous Dirichlet conditions ( $c = 0$ ) at the boundary. Under these assumptions, the solute concentration field is governed by the dispersion equation

$$\frac{\partial c}{\partial t} = \nabla \cdot (\mathbf{D}_H \cdot \nabla c), \quad (59)$$

where  $\mathbf{D}_H$  is the hydrodynamic dispersion tensor.

#### *Diffusive Transport*

We first consider the case of molecular diffusion, in which case  $\mathbf{D}_H = D_m \mathbf{I}$ , where  $D_m$  is the molecular diffusivity. In this case the total amount of solute  $C(t) \in [0,1]$  in the trapped region relative to the initial amount (such that  $C(0) = 1$ ) is

$$C(t) = \sum_{n=1}^{\infty} \frac{4}{\alpha_n^2} e^{-\frac{1}{\text{Pe}_m R_0^2 P} \alpha_n^2 t} \approx \frac{4}{\alpha_1^2} e^{-\frac{1}{\text{Pe}_m R_0^2 P} \alpha_1^2 t}, \quad (60)$$

where  $\alpha_n$  is the  $n$ -th zero of the zero-th order Bessel function of the first kind and  $\text{Pe}_m = L^2/(D_m P)$  is a Péclet number defined in terms of the forcing period  $P$  and dimension  $L$  of the aquifer. The molecular diffusivity of water  $D_m \sim 10^{-9} \text{ m}^2/\text{s}$  then yields an estimate of this Péclet number of order  $\text{Pe}_m \sim 10^{11}$  for a typical coastal aquifer of width  $L \sim 2000\text{m}$  subject to

a  $P = 12$ -hour tidal period. As per equation (60), for all but very short times, the total relative solute amount decays exponentially at a rate very close to  $-\alpha_1^2/(R_0^2 \text{Pe}_m)$  (with  $\alpha_1 = 2.40483$ ), thus 90% of solute has leached out of the trapped regions after time  $T_{90\%}$ , which is defined as

$$T_{90\%} \approx P \text{Pe}_m \frac{R_0^2}{\alpha_1^2} \ln(10). \quad (61)$$

Thus, the residence time of a solute within a given trapped region scales as  $R_0^2$ , which is proportional to the trapped region area ( $a$ ). Hence the histograms of the trapped area size ( $a$ ) shown in Figure 26b can be used to directly inform how solute transport varies with the aquifer parameters  $\mathcal{T}$ ,  $\mathcal{G}$ ,  $\mathcal{C}$ . In Chapter 5 (Section 5.4) we also show that the relative radius  $R_0$  of trapped regions scales linearly with the correlation length scale at a rate that varies with the Townley number  $\mathcal{T}$ , hence the duration of solute trapping scales quadratically with the correlation length scale. Figure 26b shows that a typical closed region has a relative area of  $a \sim 0.001$ , and so the corresponding disc has a relative radius  $R_0 \sim 0.0178$  and from (61) this takes around  $T_{90\%} \sim 16,000$  years to empty. Hence these trapped regions have a profound impact upon transport of diffusive solutes.

### ***Dispersive Transport***

We also quantify solute transport under hydrodynamic dispersion via the Scheidegger parameterization for the longitudinal  $D_L$  component of the hydrodynamic dispersivity tensor  $\mathbf{D}$  (under the assumption of relatively small transverse dispersion) which is related to the local velocity as

$$D_L = D_m + \alpha_L v, \quad (62)$$

where the longitudinal dispersivity for a coastal aquifer  $\alpha_L$  is estimated to be of order 10 m or larger. To provide an estimate of this residence time, we need to relate the mean regional

flow velocity to the tidally influenced velocity near the tidal boundary. The mean regional groundwater velocity is

$$\bar{v}_r = -J \frac{K_{\text{eff}}}{\varphi_{\text{eff}}}, \quad (63)$$

and the maximum tidal groundwater velocity  $\tilde{v}_{\text{max}}$  can be shown to be

$$\tilde{v}_{\text{max}} = \bar{v}_r \left( 1 + \frac{\mathcal{G}}{(1 - \mathcal{C})x_{\text{taz}}} \right). \quad (64)$$

We consider some field-scale parameters pertinent to a Safety Bay Sand/Tamala Limestone coastal aquifer near Fremantle (Smith et al., 2012). Representative parameter values are: aquifer width  $L \approx 2000$  m, dimensionless head gradient  $J \approx 0.005$ , hydraulic conductivity  $K_{\text{eff}} \approx 10$  m/d, dimensionless porosity  $\varphi_{\text{eff}} \approx 0.3$ , dimensionless tidal strength in Fremantle  $\mathcal{G} \approx 0.5 / (JL)$ , tidally affected zone (dimensionless fraction of  $L$ )  $x_{\text{taz}} \approx 0.2$ , dimensionless tidal compressibility  $\mathcal{C} \approx 0.03$ . Numerical evaluations show that the regional flow velocity  $\bar{v}_r$  is well within an order of magnitude estimator of the maximum tidally induced velocity  $\tilde{v}_{\text{max}}$  for practical purposes. But for extreme values of  $\mathcal{G}$  and  $\mathcal{C}$ , the tidally induced velocity becomes significantly greater than the regional velocity. Therefore, the regional flow  $v_r = J K_{\text{eff}} / \varphi_{\text{eff}}$  provides a reasonable estimate of the local velocity  $v$  in (62), and for typical values  $J \approx 0.005$ ,  $K_{\text{eff}} \approx 10$  m/d,  $\varphi_{\text{eff}} \approx 0.3$  yields  $v_r \sim 0.16667$  m/day, this gives an estimate of the longitudinal dispersivity of  $D_L \sim 2 \times 10^{-5}$  m<sup>2</sup>/s, and a corresponding Péclet number of  $\text{Pe} \sim 10^6$ . Equation (61) then predicts a solute emptying time of 304 days, suggesting trapped regions can still dominate solute transport in the presence of hydrodynamic dispersion.

#### 6.4. Tidal Transition Diagram

The parametric studies in the previous chapter clearly show how complex transport is a natural consequence of matrix heterogeneity and compressibility in formations subject to periodic forcing. Nevertheless, it may not yet be clear when and where to expect complex

transport in natural aquifers. Chapter 4 showed that physically plausible values for  $\mathcal{T}$  and  $\mathcal{G}$  yielded Poincaré sections exhibiting elliptic and hyperbolic points at high tidal compressibility  $\mathcal{C} = 0.5$ , and results from Chapter 5 have extended the Lagrangian complexity regime to much lower tidal compressibility values. In this section, we seek to (i) clarify how realistic coastal aquifer systems relate to the topological bifurcation phenomena, (ii) provide the reader with a simple rule of thumb for assessing the potential for Lagrangian complexity in any particular field setting. In this analysis, we maintain the single-mode spectral approximation for the tidal forcing, although it is recognized that tidal spectra commonly display multimodal forms, and the effects of multimodal forcing are the subject of future studies.

As discussed in Section 6.2, published coastal aquifer studies can be used to assess likely parameter ranges for common coastal aquifer types, including sediments, limestones, fractured basalts, etc. However, the Lagrangian flow complexity is also coupled with the effective coastal tidal amplitude which is a complicated function of position around the globe. We can decouple this complexity by plotting a small number of published field sites in  $\mathcal{T} \times \mathcal{G} \times \mathcal{C}$  parameter space, superimposing the results of the topological analysis, and seeking zones of overlap for increasing tidal amplitude. We term such a plot the *tidal transition diagram* as it maps how tidal flows in specific aquifer formations move toward Lagrangian complexity as the effective tidal amplitude increases. The tidal transition diagram in Figure 27 is constructed as follows:

- i. A rectangular prism is constructed in  $\mathcal{T} \times \sigma^2 \mathcal{G} \times \mathcal{C}$  in log-scale space.
- ii. Three-dimensional coloured ellipsoids, with ellipse axes approximating error bars on the parameter estimates, are plotted according to the parameters reported in the published field studies discussed in Section 6.2.

- iii. Shaded zones are superimposed to indicate the parametric extents of the elliptic bifurcation zone (pink) and the zone of chaotic flow (red) found in the present simulations.
- iv. Phase lines are plotted from the centroid of each ellipsoid to chart how its position would change for varying tidal amplitude  $g_p$  in the range  $[0.01, 8]$  where the upper bound is the maximum tidal amplitude observed on earth (Bay of Fundy, 8 metres).

The phase lines can be computed as exact linear functions of  $g_p$  from the definitions for  $\mathcal{G}$  and  $\mathcal{C}$ . Figure 27 shows that the tidal trajectories are increasing functions of  $g_p$  and display slightly curvilinear profiles since the  $\mathcal{C}$  axis is not drawn to be exactly logarithmic. Notably, all aquifer types impinge on the pink elliptic bifurcation zone as  $g_p$  increases, at amplitudes as low as 2m, see notation marks in Figure 27b. Chaotic phenomena (red zone) are rarer, at least for this small set of field sites. Observed tidal amplitudes are complicated functions of geographic location, however, Figure 28 shows significant stretches of coastline where either K1 (Lunisolar diurnal constituent, which has a period of 23.93 hours) or M2 (Principal lunar semidiurnal constituent, which has a period of 12.42 hours) modes dominate, and in other areas mixed tides (with both diurnal and semidiurnal modes) add richness to the tidal forcing signal. There are extensive zones around the world where tidal amplitudes are much larger than for the limited case studies used here. Thus, we may anticipate that the prerequisites for complex Lagrangian flows (compressible coastal aquifers and large tidal amplitudes) are not uncommon at a global scale.

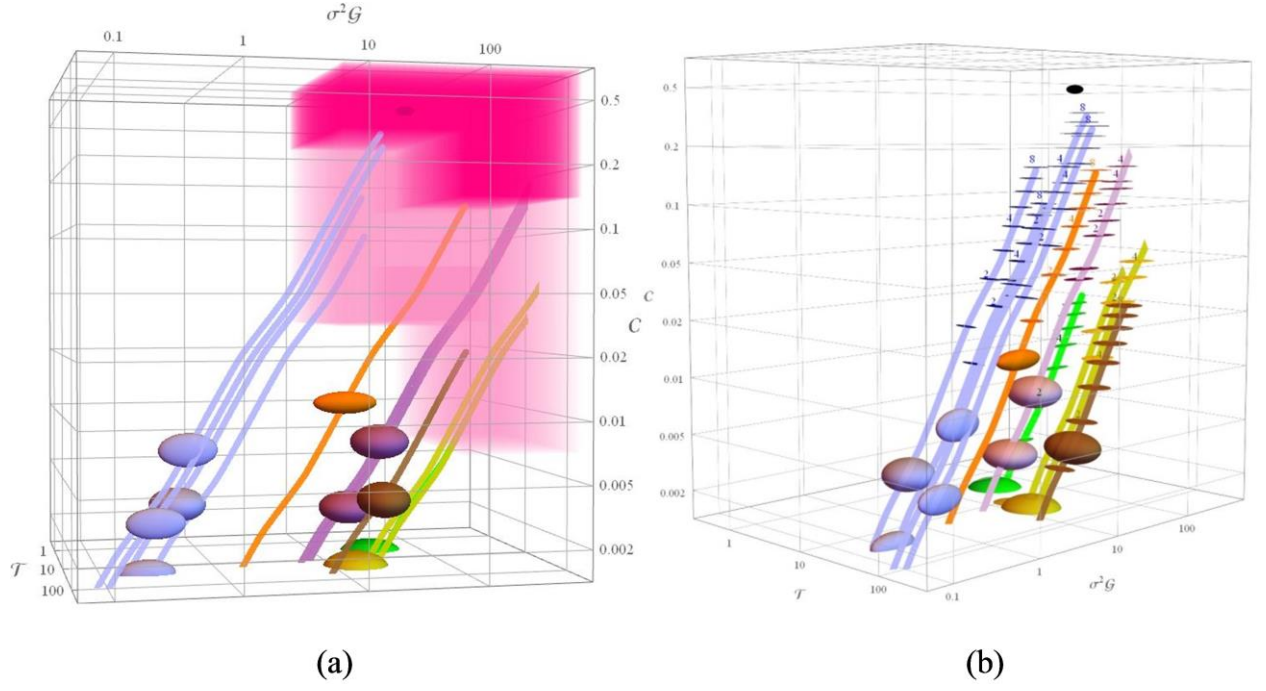


**Figure 27.** Tidal transition diagram showing (a) bifurcation and chaotic zones, and (b) tidal amplitude ( $g_p$ ) trajectories marked each metre up to a maximum of 8 m. Ellipsoids refer to the GI (blue, limestone and sand), LN (orange, sand and clay), J (purple, limestone and sand), D (brown, limestone and sand), SR (yellow, sand and clay) and P (green, basalts) case studies of Section 6.2 and the small black ellipse marks the example problem  $(\mathcal{T}, \sigma^2 \mathcal{G}, \mathcal{C}) = (10, 20, 0.5)$ . Trajectories reach the elliptic zone (pink) at values  $g_p = 3$  m (GI), 1.5 m (LN), 0.5 m (J), 3.5 m (D), 0.5 m (SR), 2 m (P).

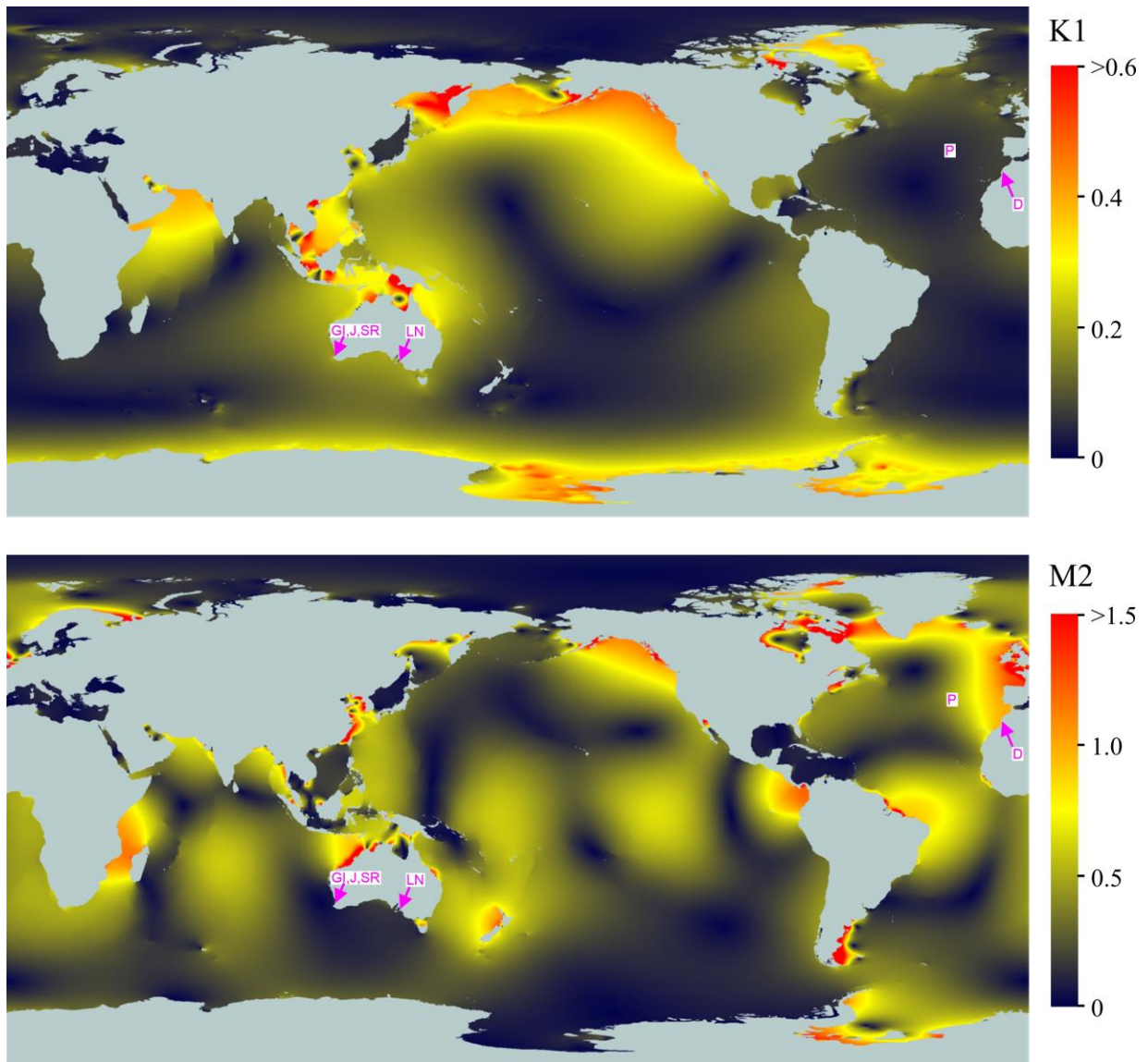


**Figure 28.** Global variation of the amplitudes (in metres) of the K1 (diurnal, top) and M2 (semi-diurnal, bottom) tidal modes (FES2004 data supplied by LEGOS, see Lyard et al. (2006)). Site locations used in Figure 27 are indicated by pink lettering. Zones of high amplitude indicate increased potential for Lagrangian complexity in coastal groundwater flows.

## 6.5. Chapter Summary

Groundwater discharge is a prime vector for contaminant migration and environmental impact. Results from the previous chapters have clearly established the presence of complex

transport phenomena and rich Lagrangian topology in tidally forced aquifers. The observations of Lagrangian phenomena in simulations influence on the utility of conventional groundwater quality characterization activities. This chapter considered the impacts of these transport dynamics on transport, mixing and reactions, and contextualize the example problem with a selection of relevant field studies. It was found that complex transport structures have profound impacts upon fluid mixing and transport, and leading to sequential effects, such as anomalous residence time distributions, flow segregation, accelerated mixing and augmented reaction kinetics. These phenomena fundamentally change the understanding of transport and mixing processes in transiently forced groundwater discharge systems.

This chapter also extends the Lagrangian analysis to dispersive/diffusive systems for translating these research findings into predictions of solute transport in realistic aquifer systems and estimates the propensity for complex transport to occur in natural coastal aquifers. The results in this chapter show that tidal forcing is sufficient to allow the formation of closed or chaotic transport regions, and such complex transport dynamics are prevalent in natural coastal aquifers around the world. It is also found that dispersing solutes can be trapped for many years when these complex transport structures arise in natural tidally forced aquifers.

## Chapter Seven

### 7. Conclusions

In this chapter, we provide a summary of the major research findings of this thesis, and we directly address the research questions identified in Chapter 1. From these answers, conclusions of the research are drawn and recommendations as to what further research directions could be pursued to gain further understanding of the transport dynamics in transiently forced aquifers and their implications for solute mixing and dispersion.

#### 7.1. Conclusions

Motivated by earlier studies in coastal groundwater hydraulics and biogeochemical transport, in this thesis, we have investigated the dynamics and kinematics of (dispersion-free) Darcy flow in transiently forced groundwater discharge system. To undertake this study, we have considered a simple 2D time-periodic model groundwater discharge system, which represents an idealisation of a broad class of natural (unpumped) hydrogeological environments. Whilst natural aquifers are more complex in that they are 3D, typically involve multi-modal forcing dynamics and density-driven flows at the saltwater-freshwater interface, this simplified 2D model provides insights into previously unrecognized complex transport phenomena that can arise in these systems, including controlling dynamics and governing mechanisms. Although a complete understanding of these transport dynamics involves extension of this model system to 3D, multi-modal forcing and coupling with density-driven flows, consideration of these dynamics in this simplified 2D model provides a critical starting point for a complete understanding of this complex transport behaviour and its implications for solute transport, chemical reactions and biological activity.

Using standard linear poroelastic theory, spectral solutions to the linear Darcy flow equations that govern this simplified 2D aquifer model were obtained using a finite-

difference scheme coupled with a self-consistent streamfunction method which resulted in a highly accurate, time-periodic velocity field. This model explicitly accounts for the spatial heterogeneity of aquifer conductivity, yielding complex and coupled Spatio-temporal variations in head, porosity, flux and velocity.

In this thesis, we have, for the first time, uncovered the underlying transport structure of tidally forced aquifers. Rather than study the advection-diffusion of a diffusive scalar which can mask the underlying transport structures in these flows, we advect diffusionless tracer particles to uncover this non-trivial transport structure. Resolution of the Poincaré section of the groundwater flow considered in Chapter 4 reveals a rich Lagrangian topology, with features that include:

1. *Elliptic islands* - isolated regions of the flow which trap fluid particles indefinitely
2. *Chaotic saddles* - isolated regions of the flow which involve rapid mixing and augmented reaction kinetics
3. *Flow segregation* - division of the flow domain into distinct subdomains
4. *Tidal inflow/outflow* - division of the tidal boundary into distinct inflow or outflow regions

This complex transport structure has profound ramifications for flow, transport and reaction in time-periodic groundwater discharge systems, and changes our understanding of transport and mixing processes (such as saltwater intrusion) in these systems at a fundamental level. Combining this diffusionless transport structure with dispersive processes represents a pressing direction for future research.

We show that the interplay of tidal forcing, aquifer heterogeneity and non-zero matrix compressibility (poroelasticity) is responsible for these complex Lagrangian kinematics. All three phenomena are required to produce the repeated stretching and folding of fluid elements that generate complex transport structures. Specifically, it is the presence of flow reversal

points in the aquifer that is directly responsible for the change in flow topology from everywhere parallel streamlines (associated with steady Darcy flow) to the presence of closed flow path lines, periodic points and separatrices. This change in flow topology fundamentally alters the transport characteristics of the aquifer, leading to indefinite trapping of fluid elements in circulation regions and segregation of the flow domain into distinct regions. As shown in Figure 16, these closed flow structures and their associated hyperbolic points (which sit at the separatrices of the closed regions) can undergo further bifurcation to form chaotic saddles, which are localised regions of chaotic advection that involve rapid mixing, arbitrarily long residence times and augmented reaction kinetics.

To answer the question of what extent these transport dynamics arise in natural groundwater systems and how these dynamics depend upon the aquifer properties and characteristics of the regional and tidal flows. We have undertaken a series of parametric studies of the governing parameters that characterize the aquifer and tidal properties. This study elucidates the mechanisms that govern complex transport dynamics, bifurcations between structures with changes in the governing parameters, and indicates the propensity of complex dynamics to occur in natural aquifer systems.

To achieve this, we defined two distinct parameter sets; the aquifer parameter set  $\mathcal{Q} = (\mathcal{T}, \mathcal{G}, \mathcal{C})$  which controls the dynamics of a periodically forced aquifer, and the hydraulic conductivity parameter set  $(\sigma_{\log K}^2, \lambda)$  which characterizes the log-Gaussian conductivity field. We used numerical simulation to consider the transport dynamics of a model tidally forced aquifer over these two parameter sets. We observed a change from open fluid particle orbits (similar to open streamlines characteristic of steady Darcy flow) to closed orbits that can trap fluid particles for indefinitely long periods. With further parametric variation, these closed orbits can then become chaotic, leading to accelerated mixing dynamics and slow “leaking” of particles into and out of these previously closed regions. We find that these three different

transport structure types (open, closed, chaotic) arise at particular combinations of the governing parameters, leading to a “phase portrait” of transport dynamics over the aquifer parameter space that we explain via the physical mechanisms that govern flow in periodically forced aquifers.

Stability and robustness of the Gaussian statistical model have also been tested via changing the correlation length ( $\lambda$ ), log-variance ( $\sigma_{\log K}^2$ ) and log-conductivity realization. We find that the size of closed regions increases linearly with the correlation length ( $\lambda$ ), and the propensity for complex transport increases with log-variance ( $\sigma_{\log K}^2$ ). Although we chose a simple log-conductivity field in this study, these results give confidence that the dynamical parameters  $Q$  will likely generate similar flow characteristics regardless of the details of the aquifer heterogeneity models employed, so long as sufficient heterogeneity (quantified as log-variance) exists and that multiple heterogeneities (quantified as correlation length) span the tidally active zone.

We have quantified the impact of closed and chaotic regions upon transport of diffusive and dispersive solutes and find that such trapping impacts solute transport over long timescales at a rate proportional to the size of the closed flow region. We also examine the parametric variation of the size distribution of trapped regions with the aquifer, allowing the impacts on solute transport to be directly estimated. Simple calculations show that common coastal aquifer types can display Lagrangian bifurcations to trapping flows for sufficiently high tidal amplitudes; such tidal amplitudes may be prevalent around the world, e.g. in northern Europe, east Africa and the Alaskan-Canadian Pacific coast. These phenomena may profoundly impact on biogeochemical processes in coastal aquifers.

The results presented in this thesis demonstrate that a Darcian groundwater flow system has the potential to admit complex and possibly chaotic flows as long as two preconditions are met: a sufficiently heterogeneous and compressible aquifer domain, and at least one

transient discharge boundary. When such dynamics do arise, it will lead to mixing and reactive transport patterns that are very different from those predicted by conventional Darcy flow models. The results also predict that complex transport structures and dynamics arise in natural tidally forced aquifers around the world.

## **7.2. Recommendations of Further Research**

This study was based on understanding specific transport structures and dynamics in a transiently forced aquifer model from a dynamical systems perspective. The interplay between periodic tidal forcing, aquifer compressibility and heterogeneity were found to be necessary conditions for complex transport and mixing behaviour to arise in coastal aquifer systems. By performing a relevant parametric study, it was found that complex transport dynamics can arise in natural aquifer systems; however there exist several opportunities to extend this research in terms of a deeper understanding of these transport dynamics and their implications and the application to natural systems.

This study uses a simple 2D time-periodic aquifer model to reduce complexity and facilitate a full understanding of the associated transport dynamics. As such, there is sufficient scope to extend this model and the analysis to more realistic scenarios. Clearly, the limitation to a 2D spatial domain constrains the allowable transport dynamics, and so the extension to a 3D model would facilitate the resolution of these dynamics. Studies of chaotic advection in transient fluid flows indicate that 3D flows admit a much richer set of dynamics than 2D systems and tend to more readily transition to chaotic dynamics due to the additional degrees of freedom in the system. As such, we expect a significant increase in the complexity of the transport structures and Lagrangian kinematics that arise in 3D aquifer systems. An extension to 3D transport also allows the consideration of coupling of these dynamics with density-driven flows at the saltwater-freshwater interface. The interaction of these transport mechanisms is expected to lead to novel mixing and transport behaviour that has not been

previously uncovered. It is also important to note that the saltwater/freshwater interface in coastal aquifers often only permeates a small fraction of the entire aquifer extent, which can span from hundreds of meters.

Furthermore, in this study we have only paid scant attention to the detailed transport dynamics in the tidal emptying zone; hence there is significant scope to consider these transport dynamics in more detail, with the possibility of coupling to an oceanic transport model. This study has also only considered a simplified periodic tidal forcing model that involves a single Fourier mode, whereas natural tidal signals are multimodal and possibly aperiodic. Consideration of the impact of such forcing dynamics upon transport is an important extension of this study that is necessary to fully understand transport in these systems, and again we expect such changes to increase the complexity of the observable transport dynamics.

This study has also ignored the impact of aquifer compressibility upon changes to the local conductivity structure, a coupling which is expected to be significant as conductivity is strongly correlated with permeability. Another area for further research is the consideration of different statistical conductivity models beyond the simple Gaussian autocorrelation models considered herein. Whilst this model forms a convenient basis for the preliminary investigations in this study; it does not necessarily conform to measurements of natural aquifer property distributions. Further studies using other statistical models, e.g. exponential, multi-gaussian, fractal, and kriging models, would provide sufficient evidence to understand how Lagrangian features arise for a representative range of different statistical models for the log-conductivity.

There is also significant scope to study the impacts of the complex transport dynamics considered in this thesis upon solute mixing and dispersion, chemical reactions and biological activity. Although we provided gross estimates of the residence times of diffusive and

dispersive solutes in closed flow regions in Chapter 6, there exists significant scope to undertake much more detailed investigations of the transport of dispersive solutes in these systems more broadly, including the complex transport behaviour in chaotic regions and the mixing dynamics in the tidal emptying region. Similar to studies of diffusive transport in chaotic advection, the interplay of chaotic mixing and solute diffusion is expected to lead to accelerated mixing and strongly anomalous transport. It is also expected that such studies could lead to the development of new stochastic transport theories regarding solute mixing and dispersion in such complex flow systems. In addition to the transport of dispersive solutes, there is also significant scope to consider the impacts of complex transport dynamics upon active processes such as chemical reactions, biological activity and geochemical processes. It is now well-established (Hernández-García & López, 2004; Károlyi et al., 2000; Tél et al., 2005) that chaotic advection can fundamentally alter both chemical reactions and biological activity hosted in such flows. Thus, the impact of the detailed coupling between these complex physical, chemical, and biological processes in natural aquifers systems represents a significant problem that is expected to involve a rich array of dynamical behaviours.

Finally, there is also ample scope to apply these findings to laboratory experiments, field studies, and highly resolved models of natural coastal aquifer systems. Simple laboratory-based experiments provide an ideal platform for the direct observation and investigation of these dynamics, via e.g. novel Hele-Shaw experiments involving deformable substrates. Field studies of, e.g. flow reversal would also provide direct evidence of the prevalence of complex transport phenomena in coastal aquifer systems. Whilst challenging, the identification of such transport dynamics in highly resolved models of natural aquifer systems would also provide further evidence of the ubiquity of this transport phenomena.

The present study represents a preliminary step in the complete understanding of a hitherto uncovered transport mechanism that has significant implications for solute transport in transiently forced aquifer systems. Whilst we have made significant inroads into understanding these dynamics in the context of the simplified 2D model used herein, we anticipate that a much richer set of dynamics shall arise when this model is extended to more realistic scenarios, including 3D transport, multi-modal forcing, density-driven flows, different conductivity models, and the consideration of solute dispersion, chemical reactions and biological activity. All of these factors have significant implications for a wide range of important transport, physical and biogeochemical processes in groundwater aquifers.

## References

- Adams, E. E., & Gelhar, L. W. (1992). Field study of dispersion in a heterogeneous aquifer: 2. Spatial moments analysis. *Water Resources Research*, 28(12), 3293-3307. doi:<https://doi.org/10.1029/92wr01757>
- Adrover, A., Cerbelli, S., & Giona, M. (2002). A spectral approach to reaction/diffusion kinetics in chaotic flows. *Computers & Chemical Engineering*, 26(1), 125-139. doi:[https://doi.org/10.1016/S0098-1354\(01\)00761-X](https://doi.org/10.1016/S0098-1354(01)00761-X)
- Allshouse, M. R., & Peacock, T. (2015). Refining finite-time Lyapunov exponent ridges and the challenges of classifying them. *Chaos*, 25(8), 087410. doi:<https://doi.org/10.1063/1.4928210>
- Anschutz, P., Smith, T., Mouret, A., Deborde, J., Bujan, S., Poirier, D., & Lecroart, P. (2009). Tidal sands as biogeochemical reactors. *Estuarine Coastal and Shelf Science*, 84(1), 84-90. doi:<https://doi.org/10.1016/j.ecss.2009.06.015>
- Anwar, N., Robinson, C., & Barry, D. A. (2014). Influence of tides and waves on the fate of nutrients in a nearshore aquifer: Numerical simulations. *Advances in water resources*, 73, 203-213. doi:<https://doi.org/10.1016/j.advwatres.2014.08.015>
- Aref, H. (1984). Stirring by chaotic advection. *Journal of Fluid Mechanics*, 143, 1-21. doi: <https://doi.org/10.1017/S0022112084001233>
- Aref, H., Blake, J. R., Budišić, M., Cardoso, S. S. S., Cartwright, J. H. E., Clercx, H. J. H., . . . Tuval, I. (2017). Frontiers of chaotic advection. *Reviews of Modern Physics*, 89(2), 025007. doi: <https://doi.org/10.1103/RevModPhys.89.025007>
- Arístegui, J., Tett, P., Hernández-Guerra, A., Basterretxea, G., Montero, M. F., Wild, K., . . . Barton, E. D. (1997). The influence of island-generated eddies on chlorophyll distribution: a study of mesoscale variation around Gran Canaria. *Deep Sea Research Part I: Oceanographic Research Papers*, 44(1), 71-96. doi: [https://doi.org/10.1016/s0967-0637\(96\)00093-3](https://doi.org/10.1016/s0967-0637(96)00093-3)
- Arnold, V. I. (1965). Sur la topologie des écoulements stationnaires des fluides parfaits. In *Vladimir I. Arnold-Collected Works* (pp. 15-18). Heidelberg, Berlin: Springer.
- Aronofsky, J. S., & Heller, J. P. (1957). A Diffusion Model to Explain Mixing of Flowing Miscible Fluids in Porous Media. *Transactions of the American Institute of Mining and Metallurgical Engineers*, 210(12), 345-349. Retrieved from <Go to ISI>://WOS:A1957WY72200004
- Ataie-Ashtiani, B., Volker, R. E., & Lockington, D. A. (1999). Tidal effects on sea water intrusion in unconfined aquifers. *Journal of Hydrology*, 216(1), 17-31. doi:[https://doi.org/10.1016/S0022-1694\(98\)00275-3](https://doi.org/10.1016/S0022-1694(98)00275-3)
- Badon-Ghyben, W. (1888). Notes on the probable results of well drilling near Amsterdam. *Tijdschrift van het Koninklijk Inst. van Ing. Den Haag*, 21.
- Bagtzoglou, A. C., & Oates, P. M. (2007). Chaotic advection and enhanced groundwater remediation. *Journal of materials in civil engineering*, 19(1), 75-83. doi:[https://doi.org/10.1061/\(ASCE\)0899-1561\(2007\)19:1\(75\)](https://doi.org/10.1061/(ASCE)0899-1561(2007)19:1(75))
- Bakker, M. (2014). Exact versus Dupuit interface flow in anisotropic coastal aquifers. *Water Resources Research*, 50(10), 7973-7983. doi:<https://doi.org/10.1002/2014wr016096>
- Bear, J. (1972). *Dynamics of Fluids In Porous Media*. New York: Dover: American Elsevier Publishing Company.
- Benson, D. A. (1998). *The fractional advection-dispersion equation: Development and application*. University of Nevada, Reno,

- Benson, D. A., Meerschaert, M. M., Baeumer, B., & Scheffler, H. P. (2006). Aquifer operator scaling and the effect on solute mixing and dispersion. *Water Resources Research*, 42(1). doi:<https://doi.org/10.1029/2004wr003755>
- Benson, D. A., Meerschaert, M. M., & Revielle, J. (2013). Fractional calculus in hydrologic modeling: A numerical perspective. *Advances in water resources*, 51, 479-497. doi:<https://doi.org/10.1016/j.advwatres.2012.04.005>
- Berkowitz, B., Cortis, A., Dentz, M., & Scher, H. (2006). Modeling non-Fickian transport in geological formations as a continuous time random walk. *Reviews of Geophysics*, 44(2). doi:<https://doi.org/10.1029/2005rg000178>
- Berkowitz, B., Emmanuel, S., & Scher, H. (2008). Non-Fickian transport and multiple-rate mass transfer in porous media. *Water Resources Research*, 44(3). doi:<https://doi.org/10.1029/2007wr005906>
- Berkowitz, B., & Scher, H. (2009). Exploring the nature of non-Fickian transport in laboratory experiments. *Advances in water resources*, 32(5), 750-755. doi:<https://doi.org/10.1016/j.advwatres.2008.05.004>
- Berkowitz, B., Scher, H., & Silliman, S. E. (2000). Anomalous transport in laboratory-scale, heterogeneous porous media. *Water Resources Research*, 36(1), 149-158. doi:<https://doi.org/10.1029/1999wr900295>
- Bianchi, M., & Zheng, C. (2016). A lithofacies approach for modeling non-Fickian solute transport in a heterogeneous alluvial aquifer. *Water Resources Research*, 52(1), 552-565. doi:<https://doi.org/10.1002/2015wr018186>
- Bijeljic, B., Mostaghimi, P., & Blunt, M. J. (2013). Insights into non-Fickian solute transport in carbonates. *Water Resources Research*, 49(5), 2714-2728. doi:<https://doi.org/10.1002/wrcr.20238>
- Bochner, S. (1949). Diffusion Equation and Stochastic Processes. *Proc Natl Acad Sci U S A*, 35(7), 368-370. doi:<https://doi.org/10.1073/pnas.35.7.368>
- Bone, S. E., Charette, M. A., Lamborg, C. H., & Gonner, M. E. (2007). Has submarine groundwater discharge been overlooked as a source of mercury to coastal waters? *Environ Sci Technol*, 41(9), 3090-3095. doi:<https://doi.org/10.1021/es0622453>
- Bromly, M., & Hinz, C. (2004). Non-Fickian transport in homogeneous unsaturated repacked sand. *Water Resources Research*, 40(7). doi:<https://doi.org/10.1029/2003wr002579>
- Burnett, W. C., Bokuniewicz, H., Huettel, M., Moore, W. S., & Taniguchi, M. (2003). Groundwater and pore water inputs to the coastal zone. *Biogeochemistry*, 66(1), 3-33. doi: <https://doi.org/10.1023/b:Biog.0000006066.21240.53>
- Cartwright, N., Nielsen, P., & Dunn, S. (2003). Water table waves in an unconfined aquifer: Experiments and modeling. *Water Resources Research*, 39(12). doi:<https://doi.org/10.1029/2003wr002185>
- Charette, M. A., & Sholkovitz, E. R. (2002). Oxidative precipitation of groundwater-derived ferrous iron in the subterranean estuary of a coastal bay. *Geophysical Research Letters*, 29(10), 85-81-85-84. doi:<https://doi.org/10.1029/2001gl014512>
- Chen, B.-F., & Hsu, S.-M. (2004). Numerical Study of Tidal Effects on Seawater Intrusion in Confined and Unconfined Aquifers by Time-Independent Finite-Difference Method. *Journal of Waterway, Port, Coastal, and Ocean Engineering*, 130(4), 191-206. doi:[https://doi.org/10.1061/\(ASCE\)0733-950X\(2004\)130:4\(191\)](https://doi.org/10.1061/(ASCE)0733-950X(2004)130:4(191))
- Cho, M. S., Solano, F., Thomson, N. R., Trefry, M. G., Lester, D. R., & Metcalfe, G. (2019). Field Trials of Chaotic Advection to Enhance Reagent Delivery. *Ground Water Monitoring and Remediation*, 39(3), 23-39. doi:<https://doi.org/10.1111/gwmmr.12339>
- Cirpka, O. A., & Attinger, S. (2003). Effective dispersion in heterogeneous media under random transient flow conditions. *Water Resources Research*, 39(9). doi:<https://doi.org/10.1029/2002wr001931>

- Coussy, O. (2004). *Poromechanics*: Wiley.
- Cruz, V. J., & Silva, O. M. (2001). Hydrogeologic framework of Pico Island, Azores, Portugal. *Hydrogeology Journal*, 9(2), 177-189. doi:<https://doi.org/10.1007/s100400000106>
- Cuthbert, M. O., Acworth, R. I., Andersen, M. S., Larsen, J. R., McCallum, A. M., Rau, G. C., & Tellam, J. H. (2016). Understanding and quantifying focused, indirect groundwater recharge from ephemeral streams using water table fluctuations. *Water Resources Research*, 52(2), 827-840. doi:<https://doi.org/10.1002/2015wr017503>
- Darcy, H. (1856). *Les fontaines publiques de la ville de Dijon. Exposition et application des principes à suivre et des formules à employer dans les questions de distribution d'eau: ouvrage terminé par un appendice relatif aux fournitures d'eau de plusieurs villes au filtrage des eaux et à la fabrication des tuyaux de fonte, de plomb, de tole et de bitume*: Dalmont.
- De Schepper, G., Therrien, R., Refsgaard, J. C., He, X., Kjaergaard, C., & Iversen, B. V. (2017). Simulating seasonal variations of tile drainage discharge in an agricultural catchment. *Water Resources Research*, 53(5), 3896-3920. doi:<https://doi.org/10.1002/2016wr020209>
- Delhomme, J. P. (1979). Spatial variability and uncertainty in groundwater flow parameters: A geostatistical approach. *Water Resources Research*, 15(2), 269-280. doi:<https://doi.org/10.1029/WR015i002p00269>
- Delleur, J. W. (2010). *The handbook of groundwater engineering*. Heidelberg, Berlin: CRC press.
- Dentz, M., & Carrera, J. (2003). Effective dispersion in temporally fluctuating flow through a heterogeneous medium. *Physical Review E*, 68(3), 036310. doi:<https://doi.org/10.1103/PhysRevE.68.036310>
- Dentz, M., & Carrera, J. (2005). Effective solute transport in temporally fluctuating flow through heterogeneous media. *Water Resources Research*, 41(8). doi:<https://doi.org/10.1029/2004wr003571>
- Dentz, M., Kang, P. K., & Le Borgne, T. (2015). Continuous time random walks for non-local radial solute transport. *Advances in water resources*, 82, 16-26. doi:<https://doi.org/10.1016/j.advwatres.2015.04.005>
- Dentz, M., Kinzelbach, H., Attinger, S., & Kinzelbach, W. (2003). Numerical studies of the transport behavior of a passive solute in a two-dimensional incompressible random flow field. *Phys Rev E Stat Nonlin Soft Matter Phys*, 67(4 Pt 2), 046306. doi:<https://doi.org/10.1103/PhysRevE.67.046306>
- Dentz, M., Lester, D. R., Le Borgne, T., & de Barros, F. P. J. (2016). Coupled continuous-time random walks for fluid stretching in two-dimensional heterogeneous media. *Physical Review E*, 94(6), 061102. doi: <https://doi.org/10.1103/PhysRevE.94.061102>
- Deutsch, C. V., & Journel, A. G. (1992). Geostatistical software library and user's guide. *New York*, 119, 147.
- Diersch, H.-J. G. (2013). *FEFLOW: finite element modeling of flow, mass and heat transport in porous and fractured media*: Springer Science & Business Media.
- Ding, D., Benson, D. A., Fernández-García, D., Henri, C. V., Hyndman, D. W., Phanikumar, M. S., & Bolster, D. (2017). Elimination of the Reaction Rate “Scale Effect”: Application of the Lagrangian Reactive Particle-Tracking Method to Simulate Mixing-Limited, Field-Scale Biodegradation at the Schoolcraft (MI, USA) Site. *Water Resources Research*, 53(12), 10411-10432. doi: <https://doi.org/10.1002/2017wr021103>

- Domenico, P. A., & Mifflin, M. D. (1965). Water from low-permeability sediments and land subsidence. *Water Resources Research*, 1(4), 563-576. doi:<https://doi.org/10.1029/WR001i004p00563>
- Eakins, B., & Sharman, G. (2010). Volumes of the World's Oceans from ETOPO1. NOAA National Geophysical Data Center, Boulder, CO, 7.
- Ezzedine, S., Rubin, Y., & Chen, J. (1999). Bayesian Method for hydrogeological site characterization using borehole and geophysical survey data: Theory and application to the Lawrence Livermore National Laboratory Superfund Site. *Water Resources Research*, 35(9), 2671-2683. doi:<https://doi.org/10.1029/1999wr900131>
- Fadili, A., Malaurent, P., Najib, S., Mehdi, K., Riss, J., & Makan, A. (2018). Groundwater hydrodynamics and salinity response to oceanic tide in coastal aquifers: case study of Sahel Doukkala, Morocco. *Hydrogeology Journal*, 26(7), 2459-2473. doi:<https://doi.org/10.1007/s10040-018-1812-4>
- Fakir, Y. (2003). Hydrodynamic characterization of a Sahelian coastal aquifer using the ocean tide effect (Dridrate Aquifer, Morocco). *Hydrological Sciences Journal-Journal Des Sciences Hydrologiques*, 48(3), 441-454. doi:<https://doi.org/10.1623/hysj.48.3.441.45281>
- Feller, W. (2008). *An introduction to probability theory and its applications* (Vol. 2): John Wiley & Sons.
- Ferguson, G., & Gleeson, T. (2012). Vulnerability of coastal aquifers to groundwater use and climate change. *Nature Climate Change*, 2(5), 342-345. doi:<https://doi.org/10.1038/Nclimate1413>
- Ferris, J. G. (1952). *Cyclic fluctuations of water level as a basis for determining aquifer transmissibility* (Note 1). Retrieved from Washington, D.C.: <http://pubs.er.usgs.gov/publication/70133368>
- Fienen, M., Hunt, R., Krabbenhoft, D., & Clemo, T. (2009). Obtaining parsimonious hydraulic conductivity fields using head and transport observations: A Bayesian geostatistical parameter estimation approach. *Water Resources Research*, 45(8). doi:<https://doi.org/10.1029/2008wr007431>
- Finn, M. D., & Thiffeault, J. L. (2011). Topological Optimization of Rod-Stirring Devices. *SIAM review*, 53(4), 723-743. doi:<https://doi.org/10.1137/100791828>
- Gelhar, L. W. (1993). *Stochastic Subsurface Hydrology*: Prentice-Hall.
- Gelhar, L. W., & Axness, C. L. (1983). Three-dimensional stochastic analysis of macrodispersion in aquifers. *Water Resources Research*, 19(1), 161-180. doi:<https://doi.org/10.1029/WR019i001p00161>
- Geng, X., & Boufadel, M. C. (2015). Impacts of evaporation on subsurface flow and salt accumulation in a tidally influenced beach. *Water Resources Research*, 51(7), 5547-5565. doi:<https://doi.org/10.1002/2015wr016886>
- Geng, X., Boufadel, M. C., & Cui, F. (2017). Numerical modeling of subsurface release and fate of benzene and toluene in coastal aquifers subjected to tides. *Journal of Hydrology*, 551, 793-803. doi:<https://doi.org/10.1016/j.jhydrol.2016.10.039>
- Glover, R. E. (1959). The Pattern of Fresh-Water Flow in a Coastal Aquifer. *Journal of Geophysical Research*, 64(4), 457-459. doi:<https://doi.org/10.1029/JZ064i004p00457>
- Goderniaux, P., Brouyère, S., Blenkinsop, S., Burton, A., Fowler, H. J., Orban, P., & Dassargues, A. (2011). Modeling climate change impacts on groundwater resources using transient stochastic climatic scenarios. *Water Resources Research*, 47(12). doi:<https://doi.org/10.1029/2010wr010082>
- Gonzalez, D. R., Speth, R. L., Gaitonde, D. V., & Lewis, M. J. (2016). Finite-time Lyapunov exponent-based analysis for compressible flows. *Chaos*, 26(8), 083112. doi:<https://doi.org/10.1063/1.4961066>

- Greenkorn, R. A. (1962). Experimental Study of Waterflood Tracers. *Journal of Petroleum Technology*, 14(01), 87-92. doi:<https://doi.org/10.2118/169-PA>
- Hallegatte, S., Ranger, N., Mestre, O., Dumas, P., Corfee-Morlot, J., Herweijer, C., & Wood, R. M. (2011). Assessing climate change impacts, sea level rise and storm surge risk in port cities: a case study on Copenhagen. *Climatic Change*, 104(1), 113-137. doi:<https://doi.org/10.1007/s10584-010-9978-3>
- Harrington, N., & Cook, P. G. (2014). *Groundwater in Australia*. Australia: National Centre for Groundwater Research and Training.
- Heiss, J. W., Post, V. E. A., Laattoe, T., Russoniello, C. J., & Michael, H. A. (2017). Physical Controls on Biogeochemical Processes in Intertidal Zones of Beach Aquifers. *Water Resources Research*, 53(11), 9225-9244. doi: <https://doi.org/10.1002/2017wr021110>
- Hernández-García, E., & López, C. (2004). Sustained plankton blooms under open chaotic flows. *Ecological Complexity*, 1(3), 253-259. doi:<https://doi.org/10.1016/j.ecocom.2004.05.002>
- Herzberg, A. (1901). Die wasserversorgung einiger Nordseebäder. *J. Gasbeleucht. Wasserversorg.*, 44, 842-844.
- Hosono, T., Ono, M., Burnett, W. C., Tokunaga, T., Taniguchi, M., & Akimichi, T. (2012). Spatial Distribution of Submarine Groundwater Discharge and Associated Nutrients within a Local Coastal Area. *Environmental Science & Technology*, 46(10), 5319-5326. doi:<https://doi.org/10.1021/es2043867>
- Huang, K., Liu, Y., Yang, C., Duan, Y., Yang, X., & Liu, C. (2018). Identification of Hydrobiogeochemical Processes Controlling Seasonal Variations in Arsenic Concentrations Within a Riverbank Aquifer at Jiangnan Plain, China. *Water Resources Research*, 54(7), 4294-4308. doi:<https://doi.org/10.1029/2017wr022170>
- Hughes, J. D., Langevin, C. D., & Banta, E. R. (2017). *Documentation for the MODFLOW 6 framework* (6-A57). Retrieved from Reston, VA: <http://pubs.er.usgs.gov/publication/tm6A57>
- Jacob, C. E. (1950). Flow of groundwater. *Engineering hydraulics*, 321-386.
- Jones, S. W., & Aref, H. (1988). Chaotic Advection in Pulsed-Source Sink Systems. *Physics of Fluids*, 31(3), 469-485. doi:<https://doi.org/10.1063/1.866828>
- Kacimov, A. R., Obnosov, Y. V., & Yakimov, N. D. (1999). Groundwater flow in a medium with a parquet-type conductivity distribution. *Journal of Hydrology*, 226(3), 242-249. doi:[https://doi.org/10.1016/S0022-1694\(99\)00151-1](https://doi.org/10.1016/S0022-1694(99)00151-1)
- Károlyi, G., Péntek, A., Scheuring, I., Tél, T., & Toroczkai, Z. (2000). Chaotic flow: the physics of species coexistence. *Proceedings of the National Academy of Sciences of the United States of America*, 97(25), 13661-13665. doi: <https://doi.org/10.1073/pnas.240242797>
- Károlyi, G., Scheuring, I., & Czaran, T. (2002). Metabolic network dynamics in open chaotic flow. *Chaos*, 12(2), 460-469. doi:<https://doi.org/10.1063/1.1457468>
- Kelvin, W. T. (1884). *Reprint of papers on electrostatics and magnetism*: Macmillan & Company.
- Kitanidis, P. K. (1994). The concept of the Dilution Index. *Water Resources Research*, 30(7), 2011-2026. doi:<https://doi.org/10.1029/94wr00762>
- Kobayashi, S., Sugimoto, R., Honda, H., Miyata, Y., Tahara, D., Tominaga, O., . . . Taniguchi, M. (2017). High-resolution mapping and time-series measurements of <sup>222</sup>Rn concentrations and biogeochemical properties related to submarine groundwater discharge along the coast of Obama Bay, a semi-enclosed sea in Japan. *Progress in Earth and Planetary Science*, 4(1), 6. doi: <https://doi.org/10.1186/s40645-017-0124-y>

- Kuan, W. K., Jin, G. Q., Xin, P., Robinson, C., Gibbes, B., & Li, L. (2012). Tidal influence on seawater intrusion in unconfined coastal aquifers. *Water Resources Research*, 48(2). doi:<https://doi.org/10.1029/2011wr010678>
- Lee, Y. W., Hwang, D. W., Kim, G., Lee, W. C., & Oh, H. T. (2009). Nutrient inputs from submarine groundwater discharge (SGD) in Masan Bay, an embayment surrounded by heavily industrialized cities, Korea. *Sci Total Environ*, 407(9), 3181-3188. doi:<https://doi.org/10.1016/j.scitotenv.2008.04.013>
- Lenda, A., & Zuber, A. (1970). Tracer dispersion in groundwater experiments. *Isotope Hydrology*, 1970, 619-641.
- Lester, D. R., Metcalfe, G., & Trefry, M. G. (2013). Is Chaotic Advection Inherent to Porous Media Flow? *Physical review letters*, 111(17), 174101. doi:<https://doi.org/10.1103/PhysRevLett.111.174101>
- Lester, D. R., Metcalfe, G., & Trefry, M. G. (2014). Anomalous transport and chaotic advection in homogeneous porous media. *Physical Review E*, 90(6), 063012. doi:<https://doi.org/10.1103/PhysRevE.90.063012>
- Lester, D. R., Metcalfe, G., Trefry, M. G., Ord, A., Hobbs, B., & Rudman, M. (2009). Lagrangian topology of a periodically reoriented potential flow: Symmetry, optimization, and mixing. *Physical Review E*, 80(3), 036208. doi:<https://doi.org/10.1103/PhysRevE.80.036208>
- Lester, D. R., Rudman, M., Metcalfe, G., & Blackburn, H. M. (2008). Global parametric solutions of scalar transport. *Journal of Computational Physics*, 227(6), 3032-3057. doi:<https://doi.org/10.1016/j.jcp.2007.10.015>
- Lester, D. R., Rudman, M., Metcalfe, G., Trefry, M. G., Ord, A., & Hobbs, B. (2010). Scalar dispersion in a periodically reoriented potential flow: Acceleration via Lagrangian chaos. *Physical Review E*, 81(4), 046319. doi:<https://doi.org/10.1103/PhysRevE.81.046319>
- Lester, D. R., Trefry, M. G., & Metcalfe, G. (2016). Chaotic advection at the pore scale: Mechanisms, upscaling and implications for macroscopic transport. *Advances in water resources*, 97, 175-192. doi: <https://doi.org/10.1016/j.advwatres.2016.09.007>
- Levy, M., & Berkowitz, B. (2003). Measurement and analysis of non-Fickian dispersion in heterogeneous porous media. *Journal of Contaminant Hydrology*, 64(3), 203-226. doi:[https://doi.org/10.1016/S0169-7722\(02\)00204-8](https://doi.org/10.1016/S0169-7722(02)00204-8)
- Li, H., & Jiao, J. (2002). Analytical solutions of tidal groundwater flow in coastal two-aquifer system. *Advances in water resources*, 25(4), 417-426. doi:[https://doi.org/10.1016/S0309-1708\(02\)00004-0](https://doi.org/10.1016/S0309-1708(02)00004-0)
- Li, L., Barry, D. A., Cunningham, C., Stagnitti, F., & Parlange, J. Y. (2000). A two-dimensional analytical solution of groundwater responses to tidal loading in an estuary and ocean. *Advances in water resources*, 23(8), 825-833. doi:[https://doi.org/10.1016/S0309-1708\(00\)00016-6](https://doi.org/10.1016/S0309-1708(00)00016-6)
- Li, L., Barry, D. A., Jeng, D.-S., & Prommer, H. (2004). Tidal dynamics of groundwater flow and contaminant transport in coastal aquifers. *Coastal aquifer management: Monitoring, modeling, and case studies*, 115-141.
- Li, L., Barry, D. A., & Jeng, D. S. (2001). Tidal fluctuations in a leaky confined aquifer: Dynamic effects of an overlying phreatic aquifer. *Water Resources Research*, 37(4), 1095-1098. doi:<https://doi.org/10.1029/2000wr900402>
- Li, L., Barry, D. A., & Pattiaratchi, C. B. (1997). Numerical modelling of tide-induced beach water table fluctuations. *Coastal Engineering*, 30(1), 105-123. doi:[https://doi.org/10.1016/S0378-3839\(96\)00038-5](https://doi.org/10.1016/S0378-3839(96)00038-5)
- Li, X. J., Li, Y. D., Chang, C. F., Benjamin, T., Chen, Z. Y., Jon, S., . . . Rubin, Y. (2018). Stochastic, goal-oriented rapid impact modeling of uncertainty and environmental

- impacts in poorly-sampled sites using ex-situ priors. *Advances in water resources*, 111, 174-191. doi:<https://doi.org/10.1016/j.advwatres.2017.11.008>
- Liu, Y., Jiao, J. J., & Liang, W. (2018). Tidal Fluctuation Influenced Physicochemical Parameter Dynamics in Coastal Groundwater Mixing Zone. *Estuaries and Coasts*, 41(4), 988-1001. doi: <https://doi.org/10.1007/s12237-017-0335-x>
- Llopis-Albert, C., & Pulido-Velazquez, D. (2014). Discussion about the validity of sharp-interface models to deal with seawater intrusion in coastal aquifers. *Hydrological Processes*, 28(10), 3642-3654. doi:<https://doi.org/10.1002/hyp.9908>
- Lu, W., Yang, Q. C., Martin, J. D., & Juncosa, R. (2013). Numerical modelling of seawater intrusion in Shenzhen (China) using a 3D density-dependent model including tidal effects. *Journal of Earth System Science*, 122(2), 451-465. doi:<https://doi.org/10.1007/s12040-013-0273-3>
- Luo, X., Jiao, J. J., Moore, W. S., & Lee, C. M. (2014). Submarine groundwater discharge estimation in an urbanized embayment in Hong Kong via short-lived radium isotopes and its implication of nutrient loadings and primary production. *Mar Pollut Bull*, 82(1-2), 144-154. doi:<https://doi.org/10.1016/j.marpolbul.2014.03.005>
- Lyard, F., Lefevre, F., Letellier, T., & Francis, O. (2006). Modelling the global ocean tides: modern insights from FES2004. *Ocean dynamics*, 56(5-6), 394-415. doi:<https://doi.org/10.1007/s10236-006-0086-x>
- Major, E., Benson, D. A., Revielle, J., Ibrahim, H., Dean, A., Maxwell, R. M., . . . Dogan, M. (2011). Comparison of Fickian and temporally nonlocal transport theories over many scales in an exhaustively sampled sandstone slab. *Water Resources Research*, 47(10). doi:<https://doi.org/10.1029/2011wr010857>
- Malott, S., O'Carroll, D. M., & Robinson, C. E. (2017). Influence of instantaneous and time-averaged groundwater flows induced by waves on the fate of contaminants in a beach aquifer. *Water Resources Research*, 53(9), 7987-8002. doi: <https://doi.org/10.1002/2017wr020948>
- Mays, D. C., & Neupauer, R. M. (2012). Plume spreading in groundwater by stretching and folding. *Water Resources Research*, 48(7). doi:<https://doi.org/10.1029/2011wr011567>
- McLaughlin, D., & Townley, L. R. (1996). A reassessment of the groundwater inverse problem. *Water Resources Research*, 32(5), 1131-1161. doi:<https://doi.org/10.1029/96wr00160>
- Metcalf, G., Bina, C. R., & Ottino, J. M. (1995). Kinematic Considerations for Mantle Mixing. *Geophysical Research Letters*, 22(7), 743-746. doi:<https://doi.org/10.1029/95gl00056>
- Metcalf, G., Lester, D., Ord, A., Kulkarni, P., Rudman, M., Trefry, M., . . . Morris, J. (2010a). An experimental and theoretical study of the mixing characteristics of a periodically reoriented irrotational flow. *Philosophical Transactions of the Royal Society A: Mathematical, Physical and Engineering Sciences*, 368(1918), 2147-2162. doi:<https://doi.org/10.1098/rsta.2010.0037>
- Metcalf, G., Lester, D., Ord, A., Kulkarni, P., Trefry, M., Hobbs, B. E., . . . Morris, J. (2010b). A partially open porous media flow with chaotic advection: towards a model of coupled fields. *Philosophical Transactions of the Royal Society A: Mathematical, Physical and Engineering Sciences*, 368(1910), 217-230. doi:<https://doi.org/10.1098/rsta.2009.0198>
- Mezic, I., Loire, S., Fonoberov, V. A., & Hogan, P. (2010). A new mixing diagnostic and Gulf oil spill movement. *Science*, 330(6003), 486-489. doi:<https://doi.org/10.1126/science.1194607>
- Moffatt, H. K. (1969). The degree of knottedness of tangled vortex lines. *Journal of Fluid Mechanics*, 35(1), 117-129.

- Montroll, E. W., & Weiss, G. H. (1965). Random walks on lattices. II. *Journal of Mathematical Physics*, 6(2), 167-181. doi:<https://doi.org/10.1063/1.1704269>
- Moore, W. S. (1999). The subterranean estuary: a reaction zone of ground water and sea water. *Marine Chemistry*, 65(1-2), 111-125. doi: [https://doi.org/10.1016/S0304-4203\(99\)00014-6](https://doi.org/10.1016/S0304-4203(99)00014-6)
- Moore, W. S. (2010). The effect of submarine groundwater discharge on the ocean. *Ann Rev Mar Sci*, 2(1), 59-88. doi:<https://doi.org/10.1146/annurev-marine-120308-081019>
- Morris, D. A., & Johnson, A. I. (1967). *Summary of hydrologic and physical properties of rock and soil materials, as analyzed by the hydrologic laboratory of the U.S. Geological Survey, 1948-60* (1839D). Retrieved from <http://pubs.er.usgs.gov/publication/wsp1839D>
- Neuman, S. P., & Tartakovsky, D. M. (2009). Perspective on theories of non-Fickian transport in heterogeneous media. *Advances in water resources*, 32(5), 670-680. doi:<https://doi.org/10.1016/j.advwatres.2008.08.005>
- Neumann, B., Vafeidis, A. T., Zimmermann, J., & Nicholls, R. J. (2015). Future coastal population growth and exposure to sea-level rise and coastal flooding--a global assessment. *PLoS One*, 10(3), e0118571. doi:<https://doi.org/10.1371/journal.pone.0118571>
- Nielsen, P. (1990). Tidal Dynamics of the Water-Table in Beaches. *Water Resources Research*, 26(9), 2127-2134. doi:<https://doi.org/10.1029/WR026i009p02127>
- Ottino, J. M. (1989). *The Kinematics of Mixing: Stretching, Chaos, and Transport*. Cambridge, UK: Cambridge University Press.
- Paytan, A., Shellenbarger, G. G., Street, J. H., Gonneea, M. E., Davis, K., Young, M. B., & Moore, W. S. (2006). Submarine groundwater discharge: An important source of new inorganic nitrogen to coral reef ecosystems. *Limnology and Oceanography*, 51(1), 343-348. doi:<https://doi.org/10.4319/lo.2006.51.1.0343>
- Pérez-Muñuzuri, V. (2014). Mixing and clustering in compressible chaotic stirred flows. *Physical Review E*, 89(2), 022917. doi:<https://doi.org/10.1103/PhysRevE.89.022917>
- Piscopo, A. N., Neupauer, R. M., & Mays, D. C. (2013). Engineered injection and extraction to enhance reaction for improved in situ remediation. *Water Resources Research*, 49(6), 3618-3625. doi:<https://doi.org/10.1002/wrcr.20209>
- Pool, M., Carrera, J., Dentz, M., Hidalgo, J. J., & Abarca, E. (2011). Vertical average for modeling seawater intrusion. *Water Resources Research*, 47(11). doi:<https://doi.org/10.1029/2011wr010447>
- Pool, M., Post, V. E. A., & Simmons, C. T. (2014). Effects of tidal fluctuations on mixing and spreading in coastal aquifers: Homogeneous case. *Water Resources Research*, 50(8), 6910-6926. doi:<https://doi.org/10.1002/2014wr015534>
- Pool, M., Post, V. E. A., & Simmons, C. T. (2015). Effects of tidal fluctuations and spatial heterogeneity on mixing and spreading in spatially heterogeneous coastal aquifers. *Water Resources Research*, 51(3), 1570-1585. doi:<https://doi.org/10.1002/2014wr016068>
- Ravu, B., Rudman, M., Metcalfe, G., Lester, D. R., & Khakhar, D. V. (2016). Creating analytically divergence-free velocity fields from grid-based data. *Journal of Computational Physics*, 323, 75-94. doi:<https://doi.org/10.1016/j.jcp.2016.07.018>
- Richey, A. S., Thomas, B. F., Lo, M.-H., Reager, J. T., Famiglietti, J. S., Voss, K., . . . Rodell, M. (2015). Quantifying renewable groundwater stress with GRACE. *Water Resources Research*, 51(7), 5217-5238. doi:<https://doi.org/10.1002/2015wr017349>
- Roberts, M. E., Trefry, M. G., Fowkes, N., Bassom, A. P., & Abbott, P. C. (2011). Water-table response to tidal forcing at sloping beaches. *Journal of Engineering Mathematics*, 69(4), 291-311. doi:<https://doi.org/10.1007/s10665-010-9407-7>

- Robinson, C., Brovelli, A., Barry, D. A., & Li, L. (2009). Tidal influence on BTEX biodegradation in sandy coastal aquifers. *Advances in water resources*, 32(1), 16-28. doi: <https://doi.org/10.1016/j.advwatres.2008.09.008>
- Robinson, C. E., Xin, P., Santos, I. R., Charette, M. A., Li, L., & Barry, D. A. (2018). Groundwater dynamics in subterranean estuaries of coastal unconfined aquifers: Controls on submarine groundwater discharge and chemical inputs to the ocean. *Advances in water resources*, 115, 315-331. doi: <https://doi.org/10.1016/j.advwatres.2017.10.041>
- Rodríguez-Escales, P., Fernández-García, D., Drechsel, J., Folch, A., & Sanchez-Vila, X. (2017). Improving degradation of emerging organic compounds by applying chaotic advection in Managed Aquifer Recharge in randomly heterogeneous porous media. *Water Resources Research*, 53(5), 4376-4392. doi: <https://doi.org/10.1002/2016wr020333>
- Ruan, F., & McLaughlin, D. (1998). An efficient multivariate random field generator using the fast Fourier transform. *Advances in water resources*, 21(5), 385-399. doi: [https://doi.org/10.1016/S0309-1708\(96\)00064-4](https://doi.org/10.1016/S0309-1708(96)00064-4)
- Santos, I. R., Burnett, W. C., Chanton, J., Dimova, N., & Peterson, R. N. (2009). Land or ocean?: Assessing the driving forces of submarine groundwater discharge at a coastal site in the Gulf of Mexico. *Journal of Geophysical Research: Oceans*, 114(C4). doi: <https://doi.org/10.1029/2008jc005038>
- Sbarbati, C., Colombani, N., Mastrocicco, M., Aravena, R., & Petitta, M. (2015). Performance of different assessment methods to evaluate contaminant sources and fate in a coastal aquifer. *Environ Sci Pollut Res Int*, 22(20), 15536-15548. doi: <https://doi.org/10.1007/s11356-015-4731-0>
- Scheidegger, A. (1961). General Theory of Dispersion in Porous Media. *Journal of Geophysical Research*, 66(10), 3273-3278. doi: <https://doi.org/10.1029/JZ066i010p03273>
- Smith, A., Massuel, S., Pollock, D., & Dillon, P. (2012). Geohydrology of the Tamala Limestone Formation in the Perth Region: Origin and role of secondary porosity. doi: <https://doi.org/10.4225/08/599dd0fd98a44>
- Smith, A. J. (1999). Application of a tidal method for estimating aquifer diffusivity: Swan River, Western Australia.
- Smith, A. J. (2004). Mixed convection and density-dependent seawater circulation in coastal aquifers. *Water Resources Research*, 40(8). doi: <https://doi.org/10.1029/2003wr002977>
- Smith, A. J., Herne, D. E., & Turner, J. V. (2009). Wave effects on submarine groundwater seepage measurement. *Advances in water resources*, 32(6), 820-833. doi: <https://doi.org/10.1016/j.advwatres.2009.02.003>
- Smith, A. J., & Hick, W. P. (2001). *Hydrogeology and aquifer tidal propagation in Cockburn Sound, Western Australia*: CSIRO Land and Water Australia.
- Smith, A. J., Townley, L. R., & Trefry, M. G. (2005). Visualization of aquifer response to periodic forcing. *Advances in water resources*, 28(8), 819-834. doi: <https://doi.org/10.1016/j.advwatres.2005.02.001>
- Smith, A. J., Turner, J. V., Herne, D. E., & Hick, W. P. (2003). Quantifying submarine groundwater discharge and nutrient discharge into Cockburn Sound Western Australia. In *Centre for Groundwater Studies Report No. 104*: Flinders University Adelaide.
- Strack, O. D. L. (1976). A single-potential solution for regional interface problems in coastal aquifers. *Water Resources Research*, 12(6), 1165-1174. doi: <https://doi.org/10.1029/WR012i006p01165>

- Sundaram, B., Feitz, A., de Caritat, P., Plazinska, A., Brodie, R., Coram, J., & Ransley, T. (2009). Groundwater sampling and analysis—a field guide. *Geoscience Australia Record*, 27(95), 104.
- Tang, X. Z., & Boozer, A. H. (1999). A Lagrangian analysis of advection-diffusion equation for a three dimensional chaotic flow. *Physics of Fluids*, 11(6), 1418-1434. doi:<https://doi.org/10.1063/1.870006>
- Tél, T., de Moura, A., Grebogi, C., & Károlyi, G. (2005). Chemical and biological activity in open flows: A dynamical system approach. *Physics Reports*, 413(2), 91-196. doi:<https://doi.org/10.1016/j.physrep.2005.01.005>
- Thiffeault, J. L. (2010a). Braids of entangled particle trajectories. *Chaos*, 20(1), 017516. doi:<https://doi.org/10.1063/1.3262494>
- Thiffeault, J. L. (2010b). Oceans. Chaos in the Gulf. *Science*, 330(6003), 458-459. doi:<https://doi.org/10.1126/science.1197554>
- Toroczka, Z., Károlyi, G., Péntek, Á., Tél, T., & Grebogi, C. (1998). Advection of Active Particles in Open Chaotic Flows. *Physical review letters*, 80(3), 500-503. doi:<https://doi.org/10.1103/PhysRevLett.80.500>
- Townley, L. R. (1995). The Response of Aquifers to Periodic Forcing. *Advances in water resources*, 18(3), 125-146. doi:[https://doi.org/10.1016/0309-1708\(95\)00008-7](https://doi.org/10.1016/0309-1708(95)00008-7)
- Trefry, M. G. (1999). Periodic forcing in composite aquifers. *Advances in water resources*, 22(6), 645-656. doi:[https://doi.org/10.1016/S0309-1708\(98\)00037-2](https://doi.org/10.1016/S0309-1708(98)00037-2)
- Trefry, M. G., & Bekele, E. (2004). Structural characterization of an island aquifer via tidal methods. *Water Resources Research*, 40(1). doi:<https://doi.org/10.1029/2003wr002003>
- Trefry, M. G., & Johnston, C. D. (1998). Pumping Test Analysis for a Tidally Forced Aquifer. *Groundwater*, 36(3), 427-433. doi:<https://doi.org/10.1111/j.1745-6584.1998.tb02813.x>
- Trefry, M. G., Lester, D. R., Metcalfe, G., Ord, A., & Regenauer-Lieb, K. (2012). Toward enhanced subsurface intervention methods using chaotic advection. *J Contam Hydrol*, 127(1-4), 15-29. doi: <https://doi.org/10.1016/j.jconhyd.2011.04.006>
- Trefry, M. G., McLaughlin, D., Lester, D. R., Metcalfe, G., Johnston, C. D., & Ord, A. (2011). Stochastic relationships for periodic responses in randomly heterogeneous aquifers. *Water Resources Research*, 47(8). doi:<https://doi.org/10.1029/2011wr010444>
- Trefry, M. G., McLaughlin, D., Metcalfe, G., Lester, D., Ord, A., Regenauer-Lieb, K., & Hobbs, B. E. (2010). On oscillating flows in randomly heterogeneous porous media. *Philosophical Transactions of the Royal Society A: Mathematical, Physical and Engineering Sciences*, 368(1910), 197-216. doi: <https://doi.org/10.1098/rsta.2009.0186>
- Trefry, M. G., Ruan, F. P., & McLaughlin, D. (2003). Numerical simulations of preasymptotic transport in heterogeneous porous media: Departures from the Gaussian limit. *Water Resources Research*, 39(3). doi:<https://doi.org/10.1029/2001wr001101>
- Trefry, M. G., Svensson, T. J. A., & Davis, G. B. (2007). Hypoalgic influences on groundwater flux to a seasonally saline river. *Journal of Hydrology*, 335(3-4), 330-353. doi: <https://doi.org/10.1016/j.jhydrol.2006.12.001>
- Trezzi, G., Garcia-Orellana, J., Rodellas, V., Santos-Echeandia, J., Tovar-Sanchez, A., Garcia-Solsona, E., & Masque, P. (2016). Submarine groundwater discharge: A significant source of dissolved trace metals to the North Western Mediterranean Sea. *Marine Chemistry*, 186, 90-100. doi:<https://doi.org/10.1016/j.marchem.2016.08.004>

- Turcotte, D. L. (1997). *Fractals and chaos in geology and geophysics*: Cambridge university press.
- Verruijt, A. (1968). A note on the Ghyben-Herzberg formula. *Hydrological Sciences Journal*, 13(4), 43-46.
- Volk, R., Mauger, C., Bourgoïn, M., Cottin-Bizonne, C., Ybert, C., & Raynal, F. (2014). Chaotic mixing in effective compressible flows. *Physical Review E*, 90(1), 013027. doi:<https://doi.org/10.1103/PhysRevE.90.013027>
- Wada, Y., van Beek, L. P. H., & Bierkens, M. F. P. (2012). Nonsustainable groundwater sustaining irrigation: A global assessment. *Water Resources Research*, 48(6). doi:<https://doi.org/10.1029/2011wr010562>
- Westbrook, S. J., Rayner, J. L., Davis, G. B., Clement, T. P., Bjerg, P. L., & Fisher, S. T. (2005). Interaction between shallow groundwater, saline surface water and contaminant discharge at a seasonally and tidally forced estuarine boundary. *Journal of Hydrology*, 302(1-4), 255-269. doi:<https://doi.org/10.1016/j.jhydrol.2004.07.007>
- Whitaker, S. (1986). Flow in porous media I: A theoretical derivation of Darcy's law. *Transport in Porous Media*, 1(1), 3-25. doi:<https://doi.org/10.1007/bf01036523>
- Wiggins, S., & Ottino, J. M. (2004). Foundations of chaotic mixing. *Philos Trans A Math Phys Eng Sci*, 362(1818), 937-970. doi:<https://doi.org/10.1098/rsta.2003.1356>
- Wilson, A. M., & Morris, J. T. (2012). The influence of tidal forcing on groundwater flow and nutrient exchange in a salt marsh-dominated estuary. *Biogeochemistry*, 108(1-3), 27-38. doi:<https://doi.org/10.1007/s10533-010-9570-y>
- Zhang, X., & Lv, M. (2007). Persistence of anomalous dispersion in uniform porous media demonstrated by pore-scale simulations. *Water Resources Research*, 43(7). doi:<https://doi.org/10.1029/2006wr005557>

## Appendices

### Appendix A: Relative penetration distance of saline wedges

In coastal aquifers, the presence of a saltwater/freshwater interface (which often manifests as a saline wedge) can generate significant density-driven flows that are not accounted for in our current model. However, these flows are often confined to a small zone close to the coastal boundary, whereas the coastal aquifer may extend much further inland. To estimate the magnitude of the impact of these density currents upon our model predictions, below we employ a steady sharp interface model (Strack, 1976) to calculate the penetration distance of the saline wedge toe ( $x_{wt}$ ) relative to that of the tidal signal ( $x_{taz}$ ) in coastal aquifers. Due to neglect of dispersion, the sharp interface model will overestimate wedge penetration and thus will provide a conservative measure of the spatial extent of density currents near the discharge boundary. A non-dimensional expression for  $x_{taz}$  can be found in subsection 3.2.5. For a homogeneous aquifer, the penetration distance of the saline wedge toe in the presence of a regional gradient is given in the Dupuit approximation by Bakker (Bakker, 2014)

$$x_{wt}^D = d \delta / 2 J , \quad (A1)$$

where  $J$  is the regional gradient,  $d$  the aquifer thickness and  $\delta \equiv (\rho_s - \rho_f)/\rho_f \approx 0.025$  is the salinity ratio (where  $\rho_s, \rho_f$  are the saline and freshwater densities, respectively). A less conservative estimate of wedge penetration is given by Glover (Glover, 1959)

$$x_{wt}^G = (d^2 - 4 x_F^2)(\delta/2dJ) , \quad (A2)$$

with  $x_F = dJ/2\delta$ . As the wedge toe is located where the saline wedge reaches zero thickness, we define the ratio of the half-wedge position  $x_{wt}/2$  to  $x_{taz}$  as the *wedge ratio*  $W$ . In this way  $W$  measures the position where the saline interval of the water column equals the freshwater interval. Figure A1 plots  $W$  as a function of regional gradient for a range of different values of aquifer thickness, storativity and conductivity that are representative of coastal aquifers.  $W$

decreases with aquifer conductivity  $K$  as the wedge toe position  $x_{wt}$  is constant while  $x_{taz}$  increases slowly. Similarly, an increase in the regional gradient  $J$  decreases  $W$  as the increasing flux deflects the saline wedge further than it reduces the tidally active zone (and hence  $x_{taz}$ ). As expected, increasing aquifer compressibility  $S$  acts to decrease penetration of tidal signals and thus increase  $W$ .

For common regional gradients ( $J < 0.01$ ), storativities ( $S < 0.01$ ) and conductivities ( $K < 50$  m/d),  $W$  is significantly smaller than unity, hence there exist significant non-saline intervals in the saturated thickness of the aquifer through which tidal signals can propagate according to standard freshwater Darcian dynamics. Reducing  $K$  and/or increasing  $g_p$  lead to further reductions in  $W$ . Thus, for a broad range of physical aquifer parameters there remains a significant portion of the coastal aquifer systems that is not impacted by density currents but is still subject to tidal forcing. Interestingly it has been demonstrated recently (Kuan et al., 2012) that tidal fluctuations tend to reduce the wedge penetration distance predicted by sharp interface models.

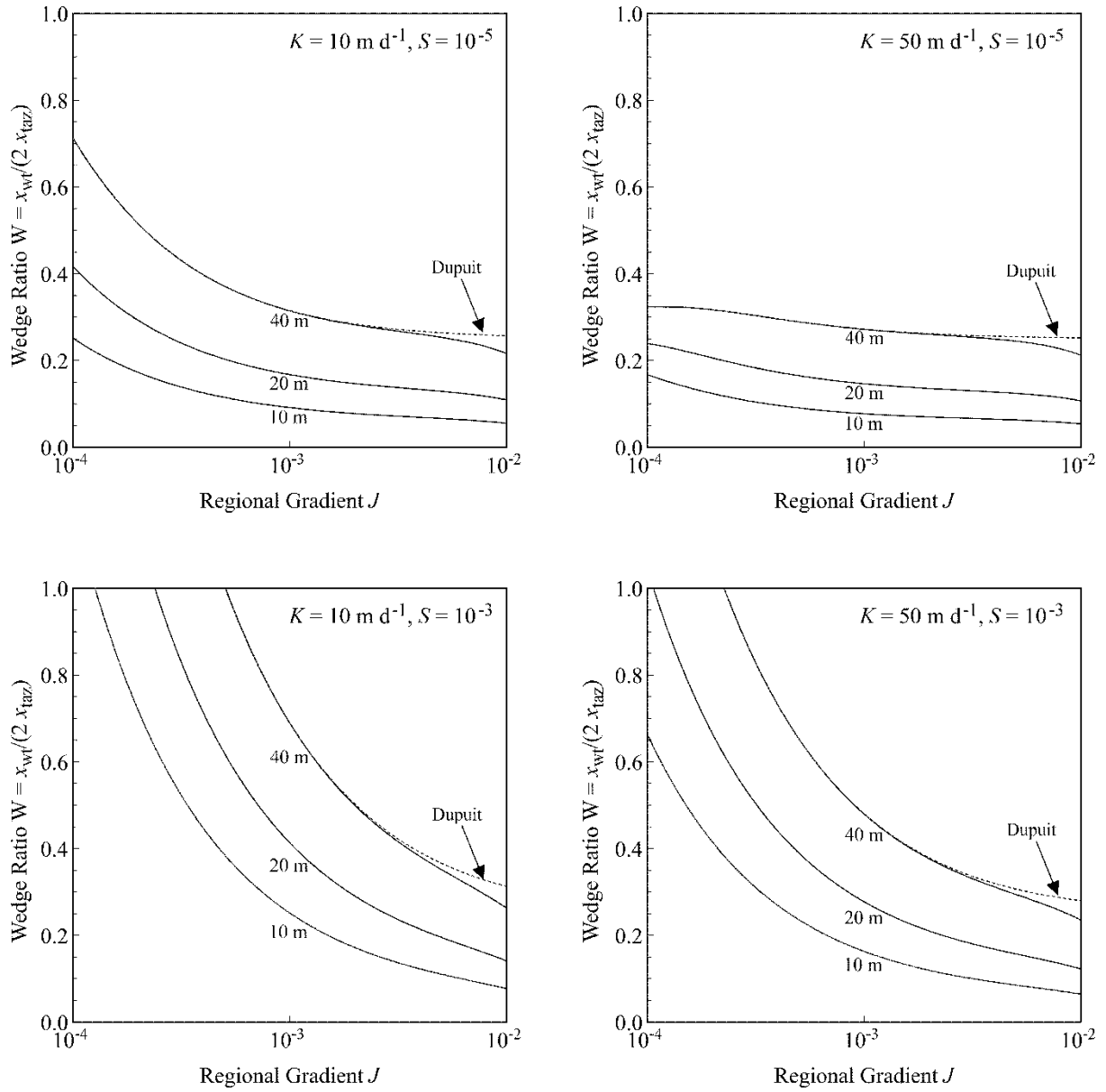


**Figure A1.** Estimates of the wedge ratio  $W$  as a function of regional gradient  $J$  in moderate conductivity ( $K = 10 \text{ m d}^{-1}$ , left column) and high conductivity ( $K = 50 \text{ m d}^{-1}$ , right column) coastal aquifers for various values of aquifer thickness  $d$  (numbers on curves) and storativity  $S$ . Solid curves incorporate the Glover result, while dotted curves show the Dupuit result for the 40 m thickness only. Tidal amplitude  $g_p$  is held fixed at 1 m.